The University of Osaka
Department of Physics - Institute for Scientific and Industrial Research

Doctor of Philosophy in Physics

Magnetotransport characteristics and surface effects on fabrication in strained Germanium two-dimensional hole gases

Doctoral Dissertation by:
Gabriel Gulak Maia

Advisor: Prof. Dr. Akira Oiwa

Supervisor of the Doctoral Program: Prof. Dr. Akira Oiwa

August 2025

This page was left blank intentionally

Preface

The present work is a small contribution to the vibrant and ever-expanding field of Solid State Physics. While it may arguably rest entirely within this field, it certainly does so while gazing at the field of Quantum Computation. The idea of quantum computers has been talked about since the second half of the last century and has become an independent and enthralling topic in itself in recent decades – fruitful both theoretically and experimentally. Nevertheless, as it is evident to anyone who dedicates their time to understanding Nature, no field stands alone. We categorise and simplify ideas, put them in different boxes for easier accessibility and smoother pedagogy, but such demarcations eventually become blurred and advancements towards a particular direction come to demand a variety of knowledge from multiple domains. This is, I believe, beautifully exemplified in the development of quantum computers and networks. Theoretical ideas in Quantum Mechanics were followed by suggestions on practical implementations which required knowledge on Chemistry, Thermodynamics, Electrical Engineering, and beyond. Some enterprises are simply too vast for a single field to tackle and the scientific effort must be distributed accordingly.

This thesis was born from such a realisation. From the difficulties that arose by approaching Ge/SiGe quantum devices fabrication in too broad a fashion. The similarities between Ge and Si have led, in the past, to attempts at transferring techniques employed in Si devices to their Ge counterparts. The idiosyncrasies of Ge, however, made this translation less feasible than one would have hoped. While Ge/SiGe devices have been experimentally achieved by a few research groups, many still struggle to master fabrication protocols, improve quality and yield. An obstacle to be overcome, particularly now, living as we are, in a period of revived interest in Ge. After all, although Ge inaugurated the field of semiconductor Physics, it was swiftly replaced in practical applications by Si and in go-to proof of concepts material by GaAs.

This challenge was certainly present in my own experience. I have initially, perhaps unwisely, tried to brute force my way through fabrication. Refining each new batch as a whole instead of understanding and optimising each fabrication step individually. In hindsight, this was an important aspect of the development of my mind as a researcher.

This thesis' focus is on Ge quantum wells. It investigates how the particularities of such heterostructures are affected by different chemical cleaning processes in order to produce clean and smooth interfaces. It also looks at how Ge quantum well structures, made into Hall bar devices, respond to interaction with light. This is a particularly important consideration as GaAs, for example, displays persistent photoconductivity phenomena, which makes it harder to operate in this context, while similar evaluations on Ge/SiGe heterostructures are not, to the best of our knowledge, yet discussed in the literature.

This thesis has a somewhat dense introduction, laying out the foundations and

the context for the interest in Ge devices. This is, of course, a deliberate choice as the thesis was written with accessibility and the struggles of young student-researchers in mind.

I would like to express my gratitude for the support of Dr Akira Oiwa during my time in his group, as well as for the support and helpful discussions with many students and researchers, from our group and others. These are, I'm afraid, too numerous to list and making any sort of selection would be committing an injustice to the rest. There are, however, people I would like to thank on a more personal basis. The friendship of Safnan Muhammad Mardhatillah, Alastair Grace Erfe and Nour Khalil was a safe haven during this challenging period. I am especially grateful to Dr Atika Nurani, for the stimulating intellectual exchanges and for the continuous and generous emotional support which proved to be an essential part of this journey. Just as no field stands alone, Science itself is not made in a vacuum, separated from other aspects of life. The foundation these individuals provided helped me push myself towards my scientific contribution. However small it may be, its shortcomings are mine alone. The support they gave me was immeasurable.

GABRIEL GULAK MAIA
Minoh
August 2025

I try all things, I achieve what I can
-Herman Melville, Moby Dick or, the Whale

(...) and I knew I could do it. It just took a few years
-Ramones, I wanna live

This page was left blank intentionally

Abstract

Since the theoretical proposals for quantum computers, and the development of quantum algorithms, which emphasised the superiority of such system over their classical counterparts, many candidates for *qubits* have been proposed, with no universally accepted platform being yet selected. A strong candidate are semiconductor spin qubits, in particular, Ge based quantum dots. Ge presents several advantages, such as strong spin-orbit coupling, fast hole mobility, the possibility for nuclear spin-free isotopic engineering of heterostructures (which improves decoherence times), and a bandgap which lies inside the bandwidth used in telecommunications. This makes Ge quantum well systems specially well-suited as a platform to bridge quantum processing (solid-state qubits) and quantum communication (photonic qubits). Efficient quantum networks, however, require also photo-spin platforms that are stable under light irradiation, free of phenomena such as persistent photoconductivity. Before the implementation of Ge devices as Poincaré interfaces, however, fabrication recipes must be optimised. While Ge devices have been successfully fabricated by a few groups, there is still a lack of detailed accounts of the physical and chemical processes taken during micro-fabrication and many groups struggle with low yield, gate leakages and similar issues.

The present work addresses both micro-fabrication challenges arising from Ge/SiGe heterostructures, and the characterisation of electronic transport with light irradiation. While Ge was at the inception of solid state electronics as we understand it today, with the first point-contact transistor being made out it, it was soon replaced in the industry by Si, due to the higher quality of its native oxide and its natural abundance. As a consequence, while fabrication techniques for Si became well-developed and optimised, such techniques are not all directly transferable to Ge. Ge native oxides are hygroscopic and thermally unstable, forming at normal laboratory conditions, which can compromise the quality of ohmic metal diffusion, and the overall quality of devices. With this concern, we have investigated different acid cleaning protocols and their effect on samples' surfaces. The recipes were based on different concentrations and dipping time on Hydrofluoric acid, with a 2 minutes dip in 10% aqueous solution, a standard recipe, being the most damaging to surface smoothness. While the cleaning power of all the recipes has been shown to be similar by surface composition analysis via XPS, more gentle approaches, with reduced concentrations (2%) and shorter dipping times proved to be a balanced choice between cleanliness and smoothness. This is an important step as native oxides and organic contaminants can prevent ohmic metals diffusion, compromising device quality. Smoothness, on the other hand, is an important aspect to consider for uniform metal diffusion, as well as for avoiding leakage pathways.

We have also investigated the effect of light irradiation on Hall bar transport measurements. While many devices performed poorly due to gate leakages and high resistance contacts, revealing a very low yield, a few devices were in good conditions enough to allow us to investigate the effect of light irradiation on Hall effect and

Shubnikov-de Haas oscillations. Overall, the light experiments show a possible photo-excitation of interfacial trap states, which saturate carrier concentration and mobility after initial irradiation, leading to seemingly stable transport characteristics Ge quantum wells themselves; an interesting result for irradiated quantum dot implementations, indicating a robustness of their characteristics under illumination.

Contents

List of Figures

Colophon

This document was typeset using the XeLaTeX typesetting system created by Jonathan Kew and distributed under the X11 free software license (MIT/X Consortium License) and the memoir class created by Peter R. Wilson. Drawings were typeset using the PSTricks package by Timothy Van Zandt. Editing and compiling were performed with the Texmaker freeware by Pascal Brachet.

1

Introduction

1.1 Classical computation

Machine assisted computation has a longer history than one may assume. The principle of rotation transfer between gears with different amounts of teeth was used over two millennia ago in devices such as the *Antikythera mechanism* [1, 2], an astronomical calculating machine, as well as in the famous *Pascaline* [3], the addition/subtraction machine devised by French philosopher Blaise Pascal, and in its improved version, which was also capable of multiplication and division, the *Stepped Reckoner*, created by German thinker Gottfried Leibniz [4]. Other methods have also been employed, such as a combination of Hydraulics and Mechanics in the *Castle Clock*, a time-keeping/automaton created by Mesopotamian polymath Ismail al-Jazari [5].

The early 19th century is, however, the beginning of the era most people would associate with the birth of computation in our modern understanding of the word, with designs such as the *Differential* and the *Analytical Engines*, both conceptualised by English polymath Charles Babbage, being the latter one a fully programmable machine [6]. By the late 19th and early 20th centuries, the history of computation becomes increasingly complex. Machines operating on different principles and different combinations of principles were being developed simultaneously, making it difficult to trace a clear line of technological development. In the first decades of the last century there were computers based on continuous variables such as shaft rotation angles (e.g. the *Differential Analyser* [7]) or currents and voltages (e.g. the *EAI 680* [8]), as well as early binary computing systems such as the *Atanasoff–Berry Computer* [9], which used vacuum tubes to implement binary logic via current/no-current states - a foundational principle to the logic gates used in modern computers. In the 1950s, even al-Jazari's seemingly exotic approach to computation, using Hydraulics, made a comeback in the form of the *Moniac*, a computer designed to simulate economic systems [10].

Both approaches had their merits and demerits. Analogue computation was made in real time and was particularly well suited for modelling differential equations, but was prone to noise and was much less flexible than their digital counterparts. The binary systems were, on the other hand, robust to noise (as one can make a 0-state as distant from a 1-state as needed to suppress error introduced by value fluctuations),

but required a discretisation of continuous problems, introducing a resolution issue in modelling the real world. While discretisation posed a non-trivial challenge, improvements in memory size and processing speed allowed digital computers to achieve resolutions sufficient for most practical applications. They were also more scalable and capable of running different programs, while analogue computers were hard-wired into solving specific problems. Even though analogue computation is still used in very niche fields today [11, 12], the last decades of the 20th century saw digital computation become the norm, in part aided by a technology developed over 30 years before: the transistor.

In 1947, U.S.-American physicists John Bardeen and Walter Brattain constructed at Bell Laboratories their first working *point-contact transistor* (PCT) [13]. Their device consisted of a slab of n-doped Germanium (Ge) mounted on top of a metallic base plate functioning as an electrical terminal. On top of the Ge slab, metal contacts placed on opposite sides of a plastic wedge were pressed against the semiconductor by a spring connected to the wedge, see Figure 1.1. These contacts were referred to as the **emitter** and the **collector** and were kept at fixed distances from one another. Their voltages were set relative to the base, closing the circuit. In an accompanying letter published on the same issue of *Physical Review* as their experimental report, Bardeen and Brattain theorised that a thin, localised, p-doped layer was formed on the surface of the Ge, creating a pn-junction, which was crucial for the working of the device [14]. A forward bias applied between the emitter and the base allowed current to flow across the pn-junction via hole injection. Meanwhile, a reverse bias was applied between the collector and the base, which should, ordinarily, block the passage of current. Due to the proximity of the contacts, however, holes injected by the emitter were captured by the collector, allowing signal to pass across the device. Furthermore, they observed that by suitably changing the bias of the emitter and the collector relative to the base, an amplification of the signal was possible: small variations of the emitter current generated larger variations of the collector current. At the opening of their original 1948 paper they already hint at the implications of their discovery for computation:

> *A Three-element electronic device which utilizes a newly discovered principle involving a semiconductor as the basic element is described. It may be employed as an amplifier, oscillator, and for other purposes for which vacuum tubes are ordinarily used.*

In the following year, the also U.S.-American physicist William Shockley, also at Bell Laboratories, built upon the achievement of his colleagues by developing a detailed theory of pn-junctions and conceptualising the first bipolar *pn-junction transistor* (BJT) [15]. His concept had an extremely thin n-doped Ge (nGe) layer at the centre, sandwiched between two p-doped regions connected to metallic contacts. The thinness of the central layer improved carrier transport by minimising recombinations along the way. The base (the third electrode) was placed in direct

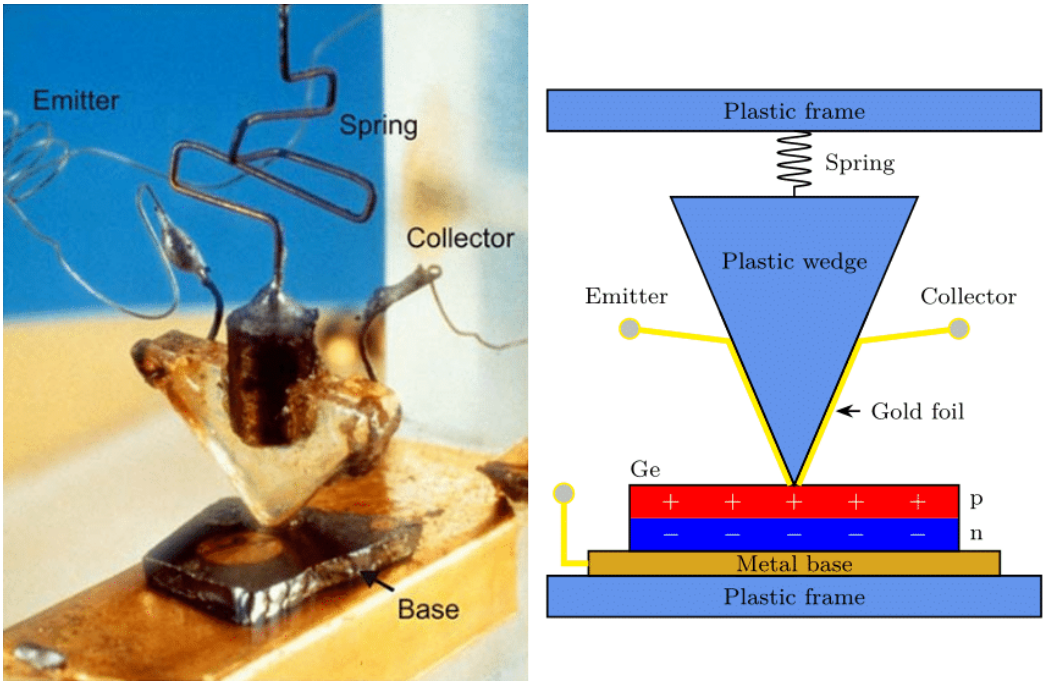

FIGURE 1.1: **The first Ge transistor:** The first Ge point-contact-transistor experimental apparatus (left) and its schematic representation (right).

contact with the nGe and transport was realised by minority carrier conduction across the junctions. In 1951 Shockley, together with U.S.-American physical chemists Morgan Sparks and Gordon Teal, constructed the first operating BJT device based on Shockley's idea [16].

In the late 1920s and early 1930s, however, an alternative theoretical approach to the development of current-control devices had been independently proposed by Austrian-Hungarian physicist Julius Edgar Lilienfeld [17] and German electrical engineer Oskar Heil [18]. Their idea, which came later to be known as *field-effect transistors* (FET), would, once experimentally realised for the first time in 1959 by Egyptian engineer Mohamed Atalla and Korean engineer Dawon Kahng [19], power the last major development in modern classical computing. Atalla and Kahng created the first MOSFET, which stands for *Metal-Oxide-Semiconductor Field Effect Transistor*, the technology still used in CPUs today.

A MOSFET consists of a lightly p(n)-doped semiconductor body with two heavily n(p)-doped regions. The two heavily doped regions are connected to metal electrodes and an oxide layer with a metal gate above it bridges both of these regions. They are known as the **source** and the **drain**, see Figure 1.2. The source is also connected to a body terminal which keeps them both at the same potential and prevents leakage currents from the source to the body. A depletion layer is formed at the borders between each doping type region which isolates source and drain. The gate terminal is used to create an electric field at the oxide-semiconductor interface,

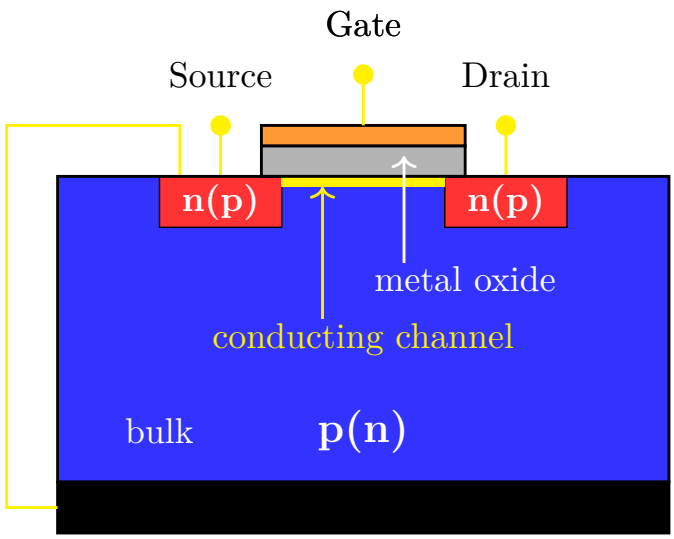

FIGURE 1.2: **MOSFET schematics:** Cross-sectional view of a Metal-Oxide-Semiconductor Field Effect Transistor.

in the same manner a capacitor would. This electric field can attract or repeal charges, modulating their density in the region (an electrically controlled doping) and effectively creating a charge pathway between source and drain. This allows the passage of an electric current which can be controlled by the voltage applied to the gate. This three-terminal architecture resembles that of vacuum tubes. The source and drain in a MOSFET are analogous to a vacuum tube's cathode and anode, respectively, while the gate functions similarly to the tube's control grid - regulating the flow of current. In both devices, current can be modulated purely through electric fields, enabling the construction of logic gates by interconnecting devices, where the output of one can serve as the input of another. MOSFETs, however, introduced significant advantages over vacuum tubes: they contain no moving parts, are highly scalable, and consume far less power. In contrast, vacuum tubes required heating the cathode to emit electrons via thermionic emission, which made them bulky and energy-intensive. These advantages have solidified the MOSFET's role as the foundational component of modern processors.

Figure 1.3 shows how MOSFETs work in real processors to built logic gates. These gates can be used to build a simple *Oracle* function. This function is designed to look for a particular entry in a data array in a way that, if the entry is, for example, a two-bit number $a = a_0 a_1 = 10$ and the data array is $x = \{00, 01, 10, 11\}$ we have

$$f(x) = f(x_0 x_1) = \begin{cases} f(00) = 0 \\ f(01) = 0 \\ f(10) = 1 \\ f(11) = 0 \end{cases} . \tag{1.1}$$

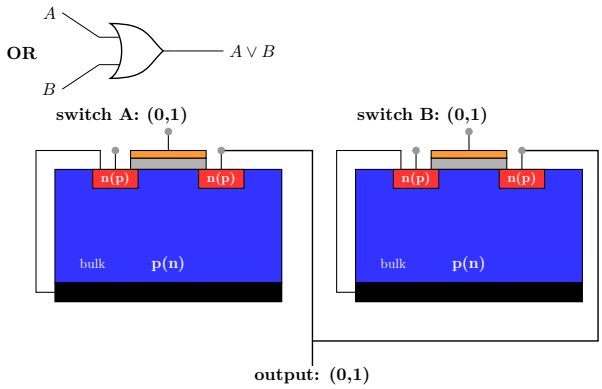

(a) **OR** gate: Either switch (gate) A or B has to be on so a signal is transmitted to the output.

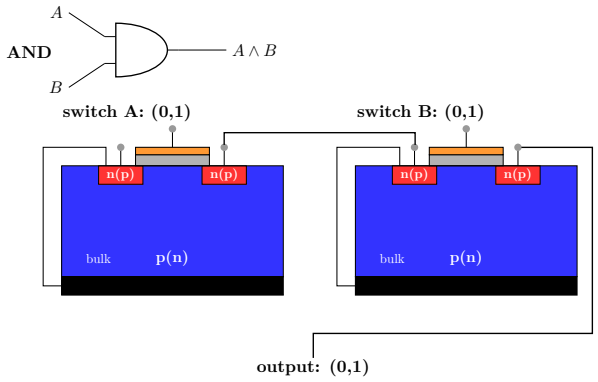

(b) **AND** gate: The drain of one MOSFET is connected directly to the source of another. The second MOSFET is the only one connected to the output, so both switches (gates) A and B must be on for an output to be present.

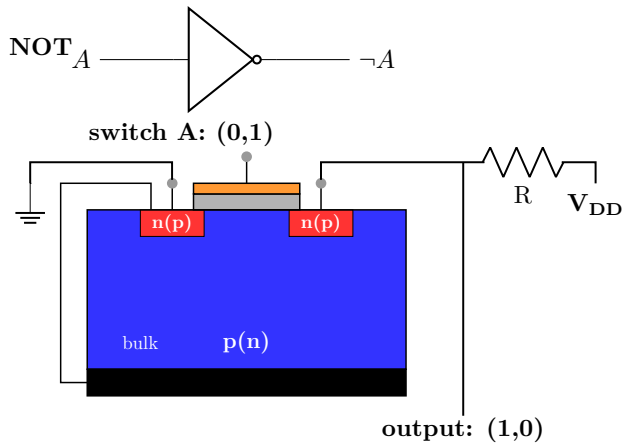

(c) **NOT** gate: If the switch (gate) is off, the voltage source $\mathbf{V_{DD}}$ is connected directly to the output. If the switch is on, the MOSFET short-circuits the path to the output.

FIGURE 1.3: **Logic gates from MOSFET:** Examples of logic gates built from MOSFETs.

In its logical form, $f(x)$ can be written as

$$f(x_0 x_1) = x_0 \wedge \neg x_1, \tag{1.2}$$

which makes clear the gates we need to build it: **NOT** and **AND** gates. The **NOT** gate flips x_1 so if the original entry was 0 it becomes 1, and if it was 1 it becomes 0. This result is then compared to x_0 via an **AND** gate which returns 0 if any of its entries is 0 and 1 if both are 1. This function can be generalised to an arbitrarily long target entry:

$$f(x) = \bigwedge_{i=0}^{n-1} \begin{cases} x_i & \text{if } a_i = 1 \\ \neg x_i & \text{if } a_i = 0 \end{cases}, \tag{1.3}$$

where n is the number of bits of the target entry a. An operation's complexity is calculated by taking into account how many times the Oracle function must be called in order for the problem to be solved. This is called *query complexity*. In our case, the Oracle does not know where the target entry is, so it must check every entry in the data array until it finds it. Since the target entry has n bits, there are 2^n possible entries to be checked, which is the maximum amount of times the function must be called. This makes the query complexity of the problem $\mathcal{O}(2^n)$.

This is, of course, a very simple example, but it shows how fast computational problems' complexity can scale up. The complexity issue can be addressed in many cases by parallel computation, that is, employing several different computers to process different parts of the problem simultaneously. Nonetheless, even parallel computation has its limits [20]. Data processing is not the only use of MOSFETs in computation. They are also used in RAM (Random Access Memory) data storage and retrieval. The two main types of RAM are DRAM (Dynamic RAM) and SRAM (Static RAM). DRAM cells are comprised of a MOS capacitor that holds each bit, accessed and refreshed via a MOSFET transistor (1T1C DRAM cell) [21], while SRAM typically employs a six-transistor (6T) MOSFET-based latch per bit, combining two cross-coupled inverters and access transistors to store information statically [22].

This brief introduction shows us how the positive features of MOSFETs listed earlier came through over the years, with every new generation of processors granting users higher computational power due to the miniaturisation of transistors. This scalability allowed for more transistors to be packed in the same space with every new generation. In fact, in 1965, in a paper titled *Cramming more components onto integrated circuits* [23], U.S.-American engineer Gordon Moore hypothesised that in 10 years a 1.6 cm^2 piece of semiconductor would be able to house 65.000 components. His prediction is often described as

> *The number of transistors in an Integrated Circuit (IC) board approximately doubles every two years*

and is known as Moore's law. In mathematical form it can be expressed as

$$n(t) = n_0 \exp\left(\frac{t}{T}\right). \tag{1.4}$$

where $n(t)$ is the number of transistors as a function of time, n_0 is the number of transistors at $t = 0$, t being the time and T the time between generations. This is a phenomenological observation rather than a law derived from physical principles, but it has been observed to be a reliable guide when compared to our technological improvements over the years, see Figure 1.4.

Moore's law cannot, however, hold forever. Everything discussed so far involves Classical Physics. The bits of information are classical binary states, charge transport is modelled with classical assumptions and so is the data processing step. As transistors become ever smaller, however, quantum effects become apparent. Miniaturisation involves thinning the gate oxide layer as well as the channel length between source and drain. In the first case, for a thin enough oxide layer charge tunnelling can happen between the channel and the gate, causing undesired electrical leakage. In the second case, when the channel length becomes comparable to the de Broglie wavelength of the charges being conducted between source and drain, the system becomes quantised and transport cannot be modelled with classical assumptions any longer.

1.2 Classical networks

Data transmission may not be intrinsically related to data processing in theory. In practice, however, both are strongly connected, as the contemporaneous prevalence of the Internet may attest. Data transmission, in ways that became foundationally relevant to its modern relation to data processing, had its origin in the 19th century with the electric telegraph. After early contributions by Samuel Thomas Soemmering (1809) and Francis Ronalds (1816), and a few early working devices by Paul Schilling von Canstatt (1832), Carl Friedrich Gauss and Wilhelm Eduard Weber (1833), and Karl August Steinheil (1835), U.S.-American inventor Samuel F. B. Morse, in the United States, and English physicist Charles Wheatstone and inventor William Fothergill Cooke, in Great Britain, presented, independently, in 1837, the two models of the technology that would become the standard [24].

Telegraphs worked by sending classically encoded binary information: electric signals (on/off current pulses) via a conductive wire. This idea was developed upon by Italian inventor Guglielmo Marconi, who in 1895 made the first public demonstration of his *wireless telegraph*, by sending binary encoded messages to a distance of approximately 2 Km [25]. His *radio*, as we refer to it today, used electromagnetic waves to encode data via their presence or absence; what is known as OOK (on-off keying). In 1899, Brazilian inventor Roberto Landell de Moura made the public demonstration of his device which delivered voice messages via radio across 4 to 8 Km distances [26]. His approach moved away from binary

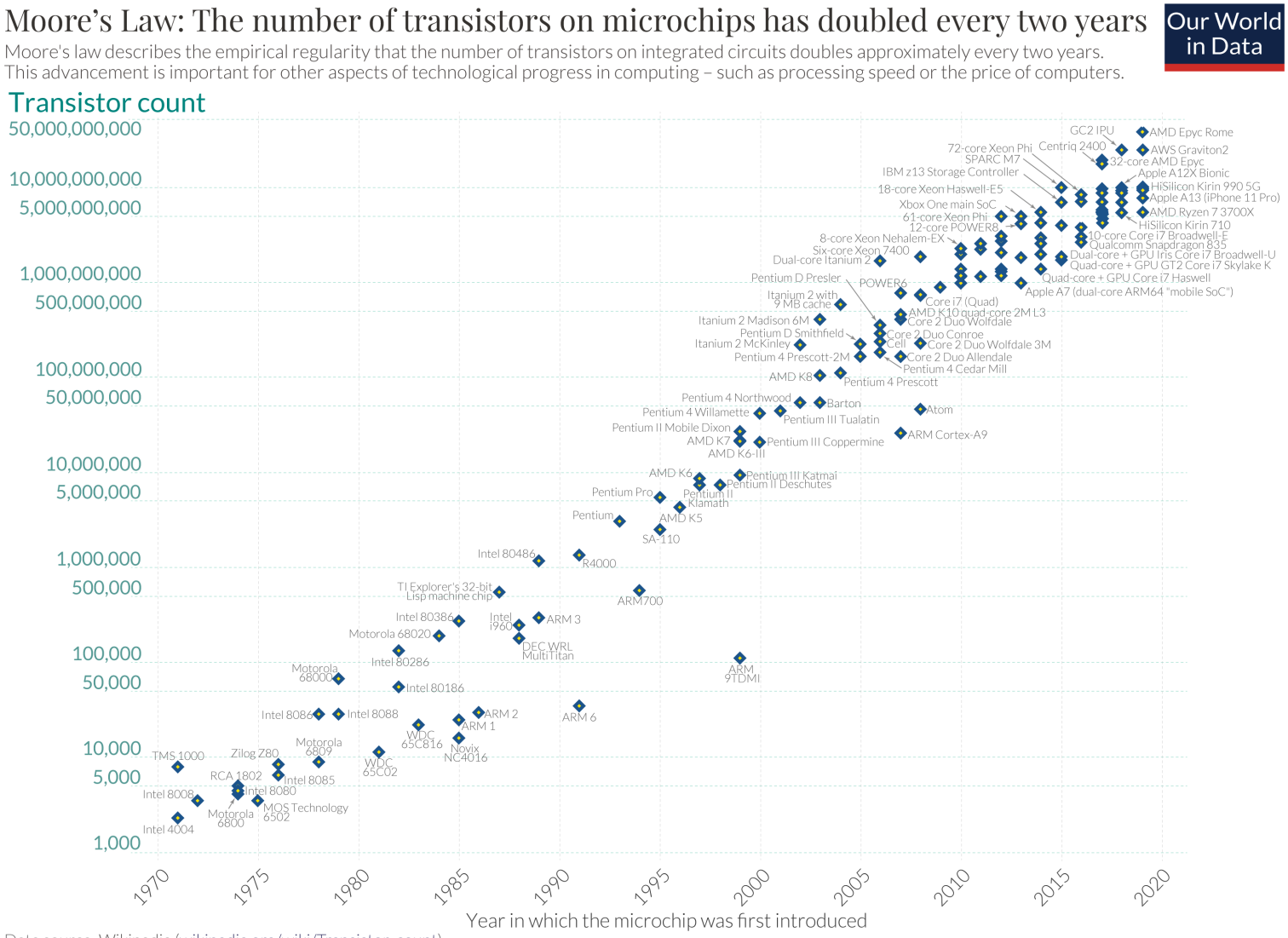

Data source: Wikipedia (wikipedia.org/wiki/Transistor_count)
OurWorldinData.org – Research and data to make progress against the world's largest problems.

FIGURE 1.4: **Moore's law:** Transistor count on Integrated Circuits over time.

encoding, introducing the first example of wireless analogue amplitude modulation: the changing air pressures on the microphone modulated the radio waves amplitudes as their were sent in a continuum, a similar technique as the one employed in telephone landlines since the 1870s.

As mentioned in the first section of this chapter, the early and mid 20th century have a convoluted history of technology, with different methods being employed concurrently. In the 1920s and 1930s, Teleprinters (teletypewriters, TTY) began using coded binary data, known as the Baudot code, which later developed into ASCII [27]. In 1937, Alec Reeves proposes pulse-code modulation (PCM) [28], which samples voice inputs, discretise them and encode them in binary form. In the 1960s his approach began being employed in telephony, with early modems being used to decode binary data back into analogue form [29, 30]. Since the 1970s data has also been transmitted via optical fibres, being encoded in light/no light states [31].

Nowadays data transmission in telecommunications involve different encoding techniques and different platforms depending on which level of the network we are looking at. Modern communication encodes data in binary or non-binary formats and modern channels can involve copper wires, optical fibres, and wireless transmission. Notwithstanding the channel, signals are always subject to attenuation and noise which degrades its fidelity as transmission distances increase. In general, guided signals lose power continuously with distance [32]. This is modelled by

$$\frac{dP(x)}{dx} = -\alpha P(x), \tag{1.5}$$

where α is the media-dependent attenuation constant. Solving this equation leaves us with an exponential power loss

$$P_{\text{out}}(L) = P_{\text{in}} e^{-\alpha L}, \tag{1.6}$$

which can be expressed in dB, as it is commonly done by engineers, via the dB-Loss definition

$$\text{Loss (dB)} = 10 \log_{10} \left(\frac{P}{P_{\text{ref}}} \right). \tag{1.7}$$

Applying it to our case, we have the power loss given by

$$\begin{aligned} P_{\text{out}}(\text{dB}) &= 10 \log_{10} \left(\frac{P_{\text{ref}}}{P_0} \right) + 10 \log_{10}(e^{-\alpha L}) \\ &= P_{\text{in}}(\text{dB}) - 10 \alpha L \log_{10}(e) \\ &= P_{\text{in}}(\text{dB}) - \alpha_{\text{dB}} L \end{aligned} \tag{1.8}$$

with the factor $\alpha_{\text{dB}} = (4.343)\alpha$. Even for optical fibre transmission, which have extremely low attenuation constants (0.2-0.4 dB/Km at telecommunications wavelengths), attenuation becomes significant over hundreds of kilometres (as in undersea cables).

In wireless communication, on the other hand, free-space path loss follows an inverse-square law. For a given wavelength λ and distance L we have that

$$P_{\text{FSL}} = \left(\frac{4\pi L}{\lambda}\right)^2, \tag{1.9}$$

(where FSL stands for Free Space Loss), due to the form of the power flux density of spherical waves:

$$S = \frac{P_t}{4\pi L^2}, \tag{1.10}$$

where P_t is the transmitted power. In both cases, the overall result is a significant power (or amplitude) decay with distance, a concern for particularly long transmission lines. Besides this expected decay, several other forms of environmental noise contamination must be taken into account, such as interference from external electromagnetic fields. To address this issue, repeater stations must be placed along communication lines. Such stations regenerate the original signal before it becomes unreadable and then resend it to the intended destination. A repeater can be a linear amplifier that boosts analogue waveforms, or it can be a digital repeater which reconstructs a clean copy of a digital bitstream.

1.3 Quantum computation

The introduction of quantum effects due to transistors' miniaturisation was not, as one might expect, the initial catalyst for the interest in the field of quantum computation, but rather a different issue: the scaling up of computational complexity. In 1980, Soviet mathematician Yuri Manin published a book whose title translates to *Computable and Non-computable* [33]. In it, Manin discussed how complex quantum systems become prohibitively computationally demanding for classical computers to simulate them. To address the issue, he then puts forward the idea of a *quantum automaton*. At the time, Manin was concerned about how Quantum Mechanics could be used to model such an automaton, without immediate concerns about physical implementations. In his words,

> Квантовый автомат должен быть абстрактным: его ма тематическая модель должна использовать лишь самые общие квант овые принципы, не предрешая физических реализаций. Тогда модель эволюции есть унитарное вращение в конечномерном гильбертовом пространстве, а модель виртуального разделения на подсистемы отве чает разложению пространства в тензорное произведение. Гдето в этой картине должно найти место взаимодействие, описываемое по тради ции эрмитовыми операторами и вероятностями[1].

[1] A quantum automaton must be abstract: its mathematical model should employ only the most general quantum principles, without presupposing any specific physical implementation. In this case,

Two years later, the seminal work by U.S.-American physicist Richard Feynman titled *Simulating Physics with Computers* [34], was published. In his paper he presented a case similar to Manin's: that quantum computers are necessary to accurately and efficiently simulate complex quantum systems. However, it soon became clear that the possibilities opened by quantum computation extended beyond the simulation of complex quantum systems: it could also be used to address a broad class of computational problems more efficiently than classical computers could, as was demonstrated in 1992 by British physicist David Deutsch and Australian mathematician Richard Jozsa [35]. In 1994 U.S.-American computer scientist Peter Shor presented his now-famous quantum algorithm for factoring large numbers, inaugurating the field he termed *quantum cryptanalysis* [36].

The ideas envisioned by Manin, Feynman, Deutsch, Jozsa, and Shor - among others - rested on a fundamentally different approach to understanding information itself. A classical bit is a one-dimensional binary entity: it exists in either one of two states, 0 or 1. This is, however, a deliberate choice. There is no fundamental physical constraint on information which requires it to be modelled by binary rather than ternary or higher-radix systems. Binary systems are, nonetheless, a robust and practical choice. Increasing the radix of a system raises the precision requirements for reliably distinguishing between multiple physical states. If different electric current values are used to denote different states, such states must be well isolated and precisely controlled, lest errors due to current fluctuations be introduced in the system. These stricter requirements make higher-radix systems more vulnerable to noise and energetically less efficient in most practical settings. Besides, Boolean algebra, the mathematical structure behind binary logic gates had already been a well-established idea since the 19th century [37, 38].

A similar argument applies to the quantum bit (qubit). Quantum systems are not inherently limited to binary states; in fact, many possess larger Hilbert spaces. Nevertheless, two-level quantum systems are the simplest non-trivial settings in which the defining features of Quantum Mechanics - superposition, interference, and entanglement - can be effectively harnessed for computation.

Let us consider a generic two-level quantum system. Analogously to the classical case, where the levels are labelled 0 and 1, the quantum levels are expressed as $|0\rangle$ and $|1\rangle$. Contrary to the classical case, however, Quantum Mechanics allows for the superposition of these levels, that is, $|0\rangle$ and $|1\rangle$ span a basis of possible states of the form[2]

$$|\psi\rangle = \alpha\,|0\rangle + \beta\,|1\rangle\,, \tag{1.11}$$

the model of its evolution is a unitary rotation in a finite-dimensional Hilbert space, and the model of its virtual division into subsystems corresponds to a decomposition of that space into a tensor product. Somewhere in this picture, there must also be room for interaction, traditionally described by Hermitian operators and probabilities. *Free translation.*

[2]This chapter's analysis of basic quantum phenomena is based on *Modern Quantum Mechanics* by Sakurai [39] and *Quantum Computation and Quantum Information* by Nielsen and Chuang [40], unless otherwise explicitly stated.

with $\alpha, \beta \in \mathbb{C}$, such that $|\alpha|^2 + |\beta|^2 = 1$. While there is still debate about how to interpret the philosophical depth of this simple mathematical expression, for practical purposes we can see it as the qubit occupying both $|0\rangle$ and $|1\rangle$ states simultaneously. This is an intrinsically quantum feature which is not directly accessible to us as classical observers. Once the state is observed, that is, measured, it collapses into one of the basis states, with probabilities $|\alpha|^2$ and $|\beta|^2$ of being in the states $|0\rangle$ and $|1\rangle$, respectively. This is not a statistical statement about our ignorance relative to an ensemble of states made up of fractions $|\alpha|^2$ and $|\beta|^2$ of two constituent states. Equation (1.11) does not describe mixtures inside an ensemble, but rather how the state $|\psi\rangle$ inhabits both basis states simultaneously. The evidence towards this interpretation comes from the fact that such systems present interference, which would not be the case in simple mixed classical ensembles. When this system is operated upon by a given unitary operator U, such that $U^\dagger U = 1$, we are left with a state $|\psi'\rangle$ given by $U|\psi\rangle$. If then, we want to find the probability of this state being measured to be in a given state $|\phi\rangle$, this probability is given by the amplitude of the projection of $|\psi'\rangle$ on $|\phi\rangle$, that is,

$$\begin{aligned} P_\phi &= |\langle\phi|\psi'\rangle|^2 \\ &= |\langle\phi|U|\psi\rangle|^2 \\ &= |\alpha|^2|\langle\phi|U|0\rangle|^2 + |\beta|^2|\langle\phi|U|1\rangle|^2 + (\alpha^*\beta + \beta^*\alpha)\langle\phi|U|0\rangle\langle\phi|U|1\rangle. \end{aligned} \tag{1.12}$$

The term depending on $\alpha^*\beta + \beta^*\alpha$ is the interference term, which is not a feature found in classical ensembles. Ensembles can, however, be treated quantum mechanically via the state densities formalism devised by Hungarian mathematician John von Neumann [41]. Using his formalism, information on ensembles is encoded on state density matrices. For an ensemble of particles in the state $|\psi\rangle$, the associated density matrix is

$$\rho = |\psi\rangle\langle\psi| = \begin{bmatrix} |\alpha|^2 & \alpha\beta^* \\ \alpha^*\beta & |\beta|^2 \end{bmatrix}, \tag{1.13}$$

where the off-diagonal elements are the coherence terms, which express the ability of the system to exhibit interference. When a system undergoes decoherence,

$$\rho \to \rho' = \begin{bmatrix} |\alpha|^2 & 0 \\ 0 & |\beta|^2 \end{bmatrix}, \tag{1.14}$$

and it behaves like a probabilistic classical bit. This happens, for example, when the system interacts with the environment in a way that conserves energy but introduces phase damping, that is

$$\rho(t) = \begin{bmatrix} |\alpha|^2 & \alpha\beta^* e^{-\gamma t} \\ \alpha^*\beta e^{-\gamma t} & |\beta|^2 \end{bmatrix}, \tag{1.15}$$

such that

$$\lim_{t\to\infty} \rho(t) = \begin{bmatrix} |\alpha|^2 & 0 \\ 0 & |\beta|^2 \end{bmatrix}. \tag{1.16}$$

This matrix representation of quantum states is particularly useful for computation, as operations (quantum gates) can be easily written as matrices. A few important quantum gates are

$$\text{Pauli} - X, Y, Z = \begin{bmatrix} 0 & 1 \\ 1 & 0 \end{bmatrix}, \quad \begin{bmatrix} 0 & -i \\ i & 0 \end{bmatrix}, \quad \begin{bmatrix} 1 & 0 \\ 0 & -1 \end{bmatrix}. \tag{1.17a}$$

$$\text{Hadamard} = \frac{1}{\sqrt{2}} \begin{bmatrix} 1 & 1 \\ 1 & -1 \end{bmatrix}. \tag{1.17b}$$

Using the Hadamard gate, in particular, we can build a *quantum Oracle* function to find a specific entry from a data set, as we did with classical logic gates. The protocol used in its quantum counterpart is known as Grover's algorithm [42]: a single qubit is spanned in a Hilbert quantum space $\mathcal{H}$. The total space for two qubits is then

$$\mathcal{H} = \mathcal{H}_1 \otimes \mathcal{H}_2. \tag{1.18}$$

The basis states of this system are denoted as $\{|00\rangle, |01\rangle, |10\rangle, |11\rangle\}$, being

$$\begin{aligned}
|00\rangle = |0\rangle \otimes |0\rangle &= \begin{bmatrix} 1 \\ 0 \end{bmatrix} \otimes \begin{bmatrix} 1 \\ 0 \end{bmatrix} = \begin{bmatrix} 1 \\ 0 \\ 0 \\ 0 \end{bmatrix}, \\
|01\rangle = |0\rangle \otimes |1\rangle &= \begin{bmatrix} 1 \\ 0 \end{bmatrix} \otimes \begin{bmatrix} 0 \\ 1 \end{bmatrix} = \begin{bmatrix} 0 \\ 1 \\ 0 \\ 0 \end{bmatrix}, \\
|10\rangle = |1\rangle \otimes |0\rangle &= \begin{bmatrix} 0 \\ 1 \end{bmatrix} \otimes \begin{bmatrix} 1 \\ 0 \end{bmatrix} = \begin{bmatrix} 0 \\ 0 \\ 1 \\ 0 \end{bmatrix}, \\
|11\rangle = |1\rangle \otimes |1\rangle &= \begin{bmatrix} 0 \\ 1 \end{bmatrix} \otimes \begin{bmatrix} 0 \\ 1 \end{bmatrix} = \begin{bmatrix} 0 \\ 0 \\ 0 \\ 1 \end{bmatrix},
\end{aligned} \tag{1.19}$$

where $|00\rangle$ describes the qubits at positions 0 and 1 of the array being in the same state $|0\rangle$, $|01\rangle$ describes the qubit at position 0 being in state $|0\rangle$ and the qubit at position 1 being in state $|1\rangle$, and so on. The 2-qubit Hadamard gate is given by

$$\mathrm{H}^{\otimes 2} = \mathrm{H} \otimes \mathrm{H} = \frac{1}{2} \begin{bmatrix} 1 & 1 \\ 1 & -1 \end{bmatrix} \otimes \begin{bmatrix} 1 & 1 \\ 1 & -1 \end{bmatrix} = \frac{1}{2} \begin{bmatrix} 1 & 1 & 1 & 1 \\ 1 & -1 & 1 & -1 \\ 1 & 1 & -1 & -1 \\ 1 & -1 & -1 & 1 \end{bmatrix}. \tag{1.20}$$

The initial state is prepared to be $|00\rangle$. The Hadamard gate is then applied on it in order to produce an equal amplitude superposition of all possible states,

$$\mathrm{H}^{\otimes 2}|00\rangle = \frac{1}{2}\begin{bmatrix}1 & 1 & 1 & 1\\ 1 & -1 & 1 & -1\\ 1 & 1 & -1 & -1\\ 1 & -1 & -1 & 1\end{bmatrix}\begin{bmatrix}1\\0\\0\\0\end{bmatrix} = \frac{1}{2}\begin{bmatrix}1\\1\\1\\1\end{bmatrix}. \tag{1.21}$$

The target entry is hard-wired into the system via the Oracle function:

$$O_f|x\rangle = (-1)^{f(x)}|x\rangle. \tag{1.22}$$

In the computational basis $\{|00\rangle, |01\rangle, |10\rangle, |11\rangle\}$, the oracle matrix is diagonal:

$$O_f = \begin{bmatrix}(-1)^{f(0)} & 0 & 0 & 0\\ 0 & (-1)^{f(1)} & 0 & 0\\ 0 & 0 & (-1)^{f(2)} & 0\\ 0 & 0 & 0 & (-1)^{f(3)}\end{bmatrix}, \tag{1.23}$$

where

$$f(x) = \begin{cases}1 & \text{if } x = x_0,\\ 0 & \text{if } x \neq x_0.\end{cases} \tag{1.24}$$

If, for example, we select the target as $x_0 = |10\rangle$, O_f becomes

$$O_f = \begin{bmatrix}1 & 0 & 0 & 0\\ 0 & 1 & 0 & 0\\ 0 & 0 & -1 & 0\\ 0 & 0 & 0 & 1\end{bmatrix}. \tag{1.25}$$

Finally, the Diffusion gate is defined as

$$\mathrm{D} = 2|\psi\rangle\langle\psi| - I, \tag{1.26}$$

where the projector $|\psi\rangle\langle\psi|$ is built from the post-Hadamard gate quantum state:

$$|\psi\rangle\langle\psi| = \frac{1}{4}\begin{bmatrix}1 & 1 & 1 & 1\\ 1 & 1 & 1 & 1\\ 1 & 1 & 1 & 1\\ 1 & 1 & 1 & 1\end{bmatrix}. \tag{1.27}$$

We have then that

$$\mathrm{D} = \begin{bmatrix}-0.5 & 0.5 & 0.5 & 0.5\\ 0.5 & -0.5 & 0.5 & 0.5\\ 0.5 & 0.5 & -0.5 & 0.5\\ 0.5 & 0.5 & 0.5 & -0.5\end{bmatrix}. \tag{1.28}$$

The Diffusion gate is then applied to the post-Oracle vector, yielding

$$\mathrm{D} \cdot \frac{1}{2} \begin{bmatrix} 1 \\ 1 \\ -1 \\ 1 \end{bmatrix} = \begin{bmatrix} 0.5 \\ 0.5 \\ 1.5 \\ 0.5 \end{bmatrix} \Big/ \sqrt{3}. \tag{1.29}$$

We can see the outputted quantum state has a higher probability of collapsing to the state $|10\rangle$ when measured, correctly identifying the target entry. This algorithm can be easily generalised to the n-qubit case:

Step 1 - Initialisation:

$$|\psi\rangle = |0\rangle^{\otimes n}. \tag{1.30}$$

$$|\psi_0\rangle = \mathrm{H}^{\otimes n} |\psi\rangle = \frac{1}{\sqrt{n}} \sum_{x=0}^{n-1} |x\rangle. \tag{1.31}$$

Step 2 - Oracle application:

$$O_f |\psi_0\rangle = (-1)^{f(x)} |\psi_0\rangle. \tag{1.32}$$

where $f(x)$ flips the phase of the target x_0. Finally, the diffusion operator D, given in this case by

$$\mathrm{D} = 2 |\psi_0\rangle \langle\psi_0| - I. \tag{1.33}$$

can be more easily implemented by noticing that

$$\mathrm{D} = \mathrm{H}^{\otimes n}(2 |0\rangle \langle 0| - I)\mathrm{H}^{\otimes n}. \tag{1.34}$$

This gate is applied on the post-oracle vector to give us the output

$$|\psi_1\rangle = \mathrm{D}(O_f |\psi_0\rangle). \tag{1.35}$$

In practice, we want to maximise the probability of wave-function collapse into the target state. This requires an iterative process where the outputted vector state is fed back into the circuit, that is,

$$|\psi_2\rangle = \mathrm{D}(O_f |\psi_1\rangle). \tag{1.36}$$

and so on, until we reach sufficiently high probabilities of measuring the target state. That is because the initial probability of measuring the correct state is $1/n$, but every iteration rotates the state vector in a two-dimensional subspace spanned by $|x_0\rangle$ (target state) and $|x_i\rangle$ (superposition of unmarked states). Defining this rotation angle via

$$\sin \frac{\theta}{2} = \frac{1}{\sqrt{n}}, \tag{1.37}$$

after k iterations the rotation angle becomes $(2k+1)\theta/2$. If we want the state vector to be approximately aligned with $|x_0\rangle$ this will require that

$$(2k+1)\frac{\theta}{2} \approx \frac{\pi}{2}. \tag{1.38}$$

Solving for k we have

$$k \approx \frac{\pi}{4\theta} - \frac{1}{2}. \tag{1.39}$$

For large enough n,

$$\sin\frac{\theta}{2} \approx \frac{1}{\sqrt{n}} \quad \Longrightarrow \quad \theta \approx \frac{2}{\sqrt{n}}. \tag{1.40}$$

giving us $k \approx \frac{\pi}{4}\sqrt{n}$. This means a computational complexity of order $\mathcal{O}(\sqrt{n})$. A superior result to the classical complexity of $\mathcal{O}(2^n)$.

The discussion up to this point has been, following Manin's advice, based on abstract quantum mechanical principles, without concern for their physical implementation. Such implementation, has several challenges on its path, many of which are unique to the quantum approach to information. **Noise and decoherence**, for example, are particularly important given the fragility of quantum states, which are susceptible to environmental noise such as stray electromagnetic fields, vibrations, and thermal fluctuations. All of which can introduce decoherence and, as we have seen, compromise the ability of the system to be in superposed states. As a practical consequence, computations have short coherence windows on which they can happen before energy relaxation and dephasing become issues [43–46]. **Gate fidelity**, is another important feature. It concerns how close to the gate's theoretical description the way they are implemented behave [47]. Small errors can accumulate rapidly in several iterations, eventually degrading algorithmic precision. Single qubit gate fidelities today can exceed 99.9% [48], but this success rate can drastically decrease as the number of qubits increases. This issue is addressed with error correction techniques, which suppress logical error rates to satisfactory levels. The challenge, however, posed by their implementation, is the fact that many physical qubits are required per logical qubit, limiting the quantum circuit's architecture design. This issue is referred to as the **scalability** problem [49, 50]. Increasing the system's qubit count increases the components density in the device, which creates other issues such as crosstalk between qubits and increased wiring complexity.

All these challenges have different weights based on which platform is employed for qubits implementation. While electric currents became the physical embodiment of the classical bit, many viable candidates have been proposed for their quantum counterparts. In 1995, for example, Spanish physicist Juan Ignacio Cirac and Austrian theoretician Peter Zoller presented the concept of using **cold trapped-ions** for computational purposes [51]. According to their idea, qubits are formed by individual ions in electromagnetic traps. The qubit states are modelled as hyperfine levels of the ion, and lasers can be used to cool them down or drive coherent

transitions. Trapped-ions have long coherence times and provide high fidelity, but have lower gate speeds and are difficult to scale up, requiring complex laser optics hardware as well.

In 1997, U.S.-American physicist Neil A. Gershenfeld and U.S.-American electrical engineer Isaac L. Chuang proposed using **bulk spin resonance** for quantum computation [52]. This method uses molecules' nuclei spins as quantum states, but instead of addressing them individually, several molecules (in a solid or liquid, for example) are prepared in a pseudo-pure ensemble. In an external magnetic field of amplitude B_0 , the nuclei precess with Larmor frequency $\omega_L = \gamma B_0$, where γ is the gyromagnetic ratio of the nuclei. This is set perpendicular to the bulk plane and fixes the quantisation direction. A small oscillating magnetic field is then set in-plane, controlled by radio-frequency pulses. When the frequency of the pulses matches the system's Larmor frequency, resonant absorption can be used to make the qubit transition between states. In 1998, Chuang, Gershenfeld and U.S.-American computer scientist Mark Kubinec implemented Grover's algorithm on a four-state Nuclear magnetic resonance (NMR) quantum computer [53]. NMR quantum computers have long coherence times, which are improved by lower temperatures due to the suppression of phonon interactions, and rely on well-established NMR technology. Accurate spin control, however, requires sophisticated techniques. Besides, while NMR qubits can be densely packed, scaling up qubit count while maintaining control and coherence are challenging tasks. Finally, the system is sensitive to external magnetic fields and other decoherence inducing environmental contaminations.

Alternatively, **semiconductor spin qubits** have been proposed in two fashions: quantum dots and donor atom bonding. In the first case, the spin of single electrons (or holes) is confined in gate-defined, tunable quantum dots. The idea was first proposed in 1998, by Swiss physicist Daniel Loss and U.S.-American physicist David P. DiVincenzo [54]. In the same year U.S.-American physicist Bruce E. Kane proposed encoding the qubit information in the nuclear spin of p-donors in Si substrates [55]. Single spin control and two-qubit gates have been achieved using semiconductor spin qubits as a platform. This implementation has the advantages of particularly long coherence times (specially in the case of nuclear spin) and its compatibility with well-established, industrial grade semiconductor fabrication techniques. Quantum dots, in particular, also have the advantage of direct electrical control. This implementation is, however, limited by the short-range coupling of qubits (requiring them to be a few nm apart for exchange coupling), and by strict material purity requirements. For quantum dots, for example, fabricated on quantum well heterostructures, nuclear spin can act as a source of decoherence [56]. This makes the growth of isotopically purified heterostructures a necessity, adding extra complexity to the fabrication process [57, 58]. Microfabrication also presents its challenges, with recipe optimisation being a point of current interest for materials such as Ge/SiGe [59, 60].

In 1999, Japanese physicist Yasunobu Nakamura and colleagues developed for the first time **superconducting qubits** [61]. These are Josephson junctions-based electrical circuits which display quantised energy levels at cryogenic temperatures.

Their architecture involves charge qubits, formed by a Cooper pair box, where states 0 and 1 are defined by the different occupancy of Cooper pairs in the box, and flux qubits, where states 0 and 1 are defined by the super-currents' direction in the circuit. Superconducting qubits have fast gate speeds and on chip scalability (with the ever-present price of increased wiring complexity to pay), but require sub-Kelvin cryogenic freezers and careful noise shielding.

In the following year, Austrian physicist Dieter Jaksch and his team (notoriously including Cirac and Zoller) presented the idea of **neutral-atom qubits** [62]. These are single atoms (e.g. Rubidium or Cesium) confined in optical traps or tweezer arrays, with qubit states being typically defined by the hyperfine levels of the atom. This approach uses a powerful interaction mechanism, the Rydberg blockade, in its operation: when atoms are excited to high-lying Rydberg states, the strong dipole-dipole interaction can be used to implement two-qubit gates. Such qubits can be scaled up by employing multiple tweezers arrays and can be accessed by laser control. Rydberg states are, however, short-lived, requiring fast gates for proper employment. Besides, system cooling and managing atoms loss are also challenging tasks.

In 2001, U.S.-American physicist/mathematician Emmanuel Knill, with Canadian physicist Raymond J. Laflamme, and Australian physicist Gerard J. Milburn showed how quantum computation could be achieved via linear optics and projective measurements [63]. Such **photonic qubits** can encode quantum information in properties of single photons, such as polarisation, path (dual-rail encoding), time-bin, or orbital angular momentum. Photons have the advantage of light speed travel and weak environmental coupling, making them particularly useful for communication. Photonic qubits can be operated at room temperature with inherently low decoherence and are easily integrated with fibre-optics networks. Photons do not, however, naturally interact with each other, leading to probabilistic gates. They also face the common scalability issues besides problems arising from photonic loss, photo-detectors precision, and from the difficulties in generating single photons.

In 2001, German physicist Jörg Wrachtrup and colleagues proposed the possibility of using **single electron spin in Nitrogen-vacancy centers in diamonds** for computational purposes [64]. In 2004, German physicist Fedor Jelezko's team observed coherent oscillations in this system, supporting Wrachtrup's original claim [65]. This method consists of using a substitutional Nitrogen atom adjacent to a vacancy in the Carbon lattice as a qubit. This system has spin-1 ground state, but qubits can be built by using only two spin sublevels (0 and 1). One of the main advantages of this implementation is that there is no requirement for cryogenic operation, which had been already demonstrated by German physicist A. Gruber and his team in 1997 by manipulating single NV spins at room temperature [66]. Even at such temperatures, NV centers have long coherence times and are a natural spin-photon interface. Technical limitations come, however, from creating and positioning the NV centers with precision. Besides, the system may present inhomogeneities, as the environment of each center may be slightly different. For these reasons, scaling is also an issue for NV centers.

These are important candidates, but no single platform has emerged as a uni-

versal solution. Each of them have their own strengths and challenges, both on the fabrication and operational ends. The ongoing exploration of different physical systems reflects both the richness of quantum physics and the practical realities of engineering scalable, fault-tolerant quantum computers. In parallel to the development of platforms for processing quantum information, however, a correlated question has been raised: how to transmit quantum information?

1.4 Quantum networks

When Peter Shor presented an efficient quantum algorithm for factorising integral numbers into prime factors [36], he simultaneously created the need for quantum networks. This is because classical encryption and key distribution protocols, whose breaking into is a nearly intractable problem for classical computers, is much more approachable with quantum computers. The solution is then bringing communication to the same quantum sphere we hope to bring data processing. The idea of quantum effects on communication, however, pre-dates Shor's algorithm. It was first put forward by U.S.-American physicist Stephen Wiesner. In a 1983 paper titled *Conjugate Coding* he explained how the uncertainty principle could introduce limitations on quantum communication in certain channels, while simultaneously allowing new forms of coding inaccessible to classical physics [67]. Building upon this foundational work in quantum communication protocols, U.S.-American physicist Charles Bennett and Canadian computer scientist Gilles Brassard presented in 1984 the BB84, the first quantum key distribution protocol [68, 69], a way of using Quantum Mechanics to securely transmit encryption keys.

If a sender (commonly referred to as *Alice*) sends a sequence of polarised photons through a communication channel to a receiver (*Bob*), and Bob measures the sequence in the same basis as Alice prepared them[3], by the end of the transmission they would both have the same sequence. Contrary to classical communication, quantum communication naturally imposes a barrier for eavesdroppers (usually referred to as *Eve* in this context): if the channel is tapped, Eve must make the measurements on the same basis as Alice generated them so when the information is retransmitted to Bob, they will have the expected sequence of photons. If Eve uses a different basis, Alice's sequence will not match Bob's and they will know the data has been spied upon. This still leaves, however, a window for eavesdropping, as Eve could accurately guess the basis the data is being generated on. The BB84 improves on this by employing random basis data generation and measurements: in the first step, Alice generates a sequence of photons with a randomised basis for each photon and Bob makes each measurement with a randomised photo-detector direction. In the second step they share both their bases publicly. Statistically, their sequences should match approximately 50% of the time. Eve will know which bases

[3] Alice's photon emitter could be vertically aligned, for example, and so could be Bob's photo-detector, or both of their apparatuses could be inclined with a 45° in relation to each other and so on.

were used, but not how each photon that was produced and measured on the same basis was polarised. If Eve intercepted the channel during the first step, at some point the eavesdropping basis would not coincide with Alice's and Bob's bases that should be the same, corrupting the key and making sender and receiver aware of the eavesdropper presence. Mathematically, the information produced by Alice can be encoded in $|\psi_{a_i b_j}\rangle$ states:

$$|\psi_{00}\rangle = |0\rangle, \tag{1.41a}$$

$$|\psi_{10}\rangle = |1\rangle, \tag{1.41b}$$

$$|\psi_{01}\rangle = |+\rangle = \frac{1}{\sqrt{2}}|0\rangle + \frac{1}{\sqrt{2}}|1\rangle, \tag{1.41c}$$

$$|\psi_{11}\rangle = |-\rangle = \frac{1}{\sqrt{2}}|0\rangle - \frac{1}{\sqrt{2}}|1\rangle, \tag{1.41d}$$

such that b_j encodes the basis information. A way for Eve to go around BB84 would be to copy every qubit sent by Alice, send one copy to Bob and keep another copy for herself, to be measured after the basis information was publicly shared so that eavesdropping measurements could be done later in the correct bases. This, however, is forbidden by the *No-cloning theorem*, a fundamental result in quantum information stating the impossibility of copying an unknown quantum state [70, 71]. In other words, there is no physical operation that takes an arbitrary pure state $|\psi\rangle$ and a fixed "blank" state $|e\rangle$ and produces two copies $|\psi\rangle\,|\psi\rangle$.

Theorem 1.4.1 (No-cloning theorem) *No quantum operation can perform* $|\psi\rangle_A \otimes |e\rangle_B \mapsto |\psi\rangle_A \otimes |\psi\rangle_B$ *for every input* $|\psi\rangle$.

Proof 1.4.1 *Suppose an unitary operation* U *acting on* $\mathcal{H}_A \otimes \mathcal{H}_B$ *such that, for any state* $|\psi\rangle_A$*, we have*

$$U(|\psi\rangle_A \otimes |e\rangle_B) = \exp^{i\alpha(\psi,e)} |\psi\rangle_A \otimes |\psi\rangle_B\,, \tag{1.42}$$

exists. For two distinct pure states $|\psi\rangle$ *and* $|\phi\rangle$*, since* U *is unitary, that is,* $U^\dagger U = 1$*, this would imply that*

$$\begin{aligned} \langle\phi|_A \langle e|_B \, |\psi\rangle_A |e\rangle_B &= \langle\phi|_A \langle e|_B U^\dagger U |\psi\rangle_A |e\rangle_B \\ &= \langle\phi|\psi\rangle^2\,, \end{aligned} \tag{1.43}$$

where $|e\rangle$ *is assumed normalised. This means that*

$$|\,\langle\phi|\psi\rangle\,| = |\,\langle\phi|\psi\rangle\,|^2, \tag{1.44}$$

which is only the case if $\langle\phi|\psi\rangle = 1$ *or* $\langle\phi|\psi\rangle = 0$*. The cloning is, therefore, not valid for arbitrary states, as originally assumed.*

A more sophisticated quantum key distribution protocol was proposed by British/Polish physicist Artur Ekert in 1991, being known as E91 [72]. To understand it, however, we need to be introduced to a new aspect of quantum systems. In the previous section we stated that three features of quantum physics - superposition, coherence, and entanglement - made quantum computation fundamentally different from its classical counterpart. Nevertheless, we have yet to introduce the concept of entanglement. While there are quantum gates and algorithms that make use of this feature, its discussion has been halted so far as it is particularly important for quantum communication.

In 1935 German physicist Albert Einstein, Russian-U.S.-American physicist Boris Podolsky and U.S-American physicist Nathan Rosen (commonly referred to, in conjunct, as *EPR*) brought up questions about the physical interpretation of quantum physics based on its mathematical structure [73]. The particular phenomenon they addressed was termed *entanglement* by Austrian-Irish physicist Erwin Schrödinger that same year [74]. The concept of entanglement is based on the idea that the wave function of a composite-system is not necessarily factorisable, that is, the system's state cannot be expressed as the multiplication of the states of each constituent [75, 76].

Consider a composite-system of two particles described by the Hilbert space $\mathcal{H} = \mathcal{H}_A \otimes \mathcal{H}_B$. The most general form a state in this system can take is

$$|\psi\rangle_{AB} = \sum_{i,j} c_{i,j} |i\rangle_A \otimes |j\rangle_B . \tag{1.45}$$

If $c_{i,j}$ can be written as $c_{i,j} = c_i^A c_j^B$, the pure state $|\psi\rangle_{AB} \in \mathcal{H}$ is called *separable*, that is, it assumes the form

$$|\psi\rangle_{AB} = |\psi\rangle_A \otimes |\psi\rangle_B , \tag{1.46}$$

such that $|\psi\rangle_A = \sum_i c_i |i\rangle$ and $|\psi\rangle_B = \sum_j c_j |j\rangle$. Otherwise, the system is said to be *entangled*. Mixed states are called *entangled* if their density matrix ρ is such that

$$\rho \neq \sum_i p_i \, \rho_A^i \otimes \rho_B^i, \tag{1.47}$$

with p_i being a probability distribution and ρ_A^i and ρ_B^i states of the sub-systems. Entanglement is then defined as the negation of a property: separability. An alternative definition of entanglement defines entangled states as those that cannot be simulated by classical correlations [77].

The four maximally entangled states that span the Hilbert space $\mathcal{H} = \mathcal{H}_1 \otimes \mathcal{H}_2$ of a bipartite system are known as Bell-states and are given by

$$|\psi^{\pm}\rangle = \frac{1}{\sqrt{2}}(|0\rangle |1\rangle \pm |1\rangle |0\rangle) \ , \ |\phi^{\pm}\rangle = \frac{1}{\sqrt{2}}(|0\rangle |0\rangle \pm |1\rangle |1\rangle). \tag{1.48}$$

These states illustrate the key feature of entanglement: a measurement on one particle instantaneously determines the state of the other, regardless of their spatial separation.

This feature was so striking, even within the quantum mechanical framework, that Einstein, Podolsky, and Rosen concluded that quantum physics must be incomplete. Since, in their view, physical reality was ensured by the ability to predict measurement outcomes with certainty, they argued that the only way to preserve locality[4] was to assume the existence of *hidden variables*: pre-existing properties within the entangled pair that determined their states prior to spatial separation, but which were not accounted for by standard quantum theory.

In 1964, Irish physicist John Bell performed a more rigorous analysis of EPR's idea [78]. Suppose an entangled pair of photons is produced and one of them is sent to Alice and one to Bob. Alice's measurement (A) will depend on the setting of her photo-detector (a) and on some hidden variable λ,

$$A(a, \lambda) = \pm 1. \tag{1.49}$$

Similarly for Bob's measurement (B),

$$B(b, \lambda) = \pm 1. \tag{1.50}$$

The locality assumption assumes A is independent of b and B is independent of a. Bell then analysed the expectation value of measurements products,

$$P(a, b) = \int d\lambda \, \rho(\lambda) \, A(a, \lambda) B(b, \lambda), \tag{1.51}$$

for Alice's and Bob's measurements for chosen settings a and b, mediated by a statistical distribution on hidden variables λ. λ is not accessible to the experimentalist, so its contribution must be included via a probability distribution $\rho(\lambda)$. $\rho(\lambda)$ is such that

$$\int d\lambda \rho(\lambda) = 1. \tag{1.52}$$

Consider now the cases where Alice has a fixed setting for her photo-detector, a, but Bob employs two settings, b and b'. In deterministic local hidden variable models, each party's outcome is a deterministic function of the local setting and the shared hidden variable. When Bob changes his setting, the change in the expectation value P is given by

$$|P(a, b) - P(a, b')| = \left| \int d\lambda \, \rho(\lambda) \, A(a, \lambda) \big[B(b, \lambda) - B(b', \lambda) \big] \right|. \tag{1.53}$$

Now, $B(b, \lambda) = \pm 1$, which bounds $|B(b, \lambda) - B(b', \lambda)|$ to

$$|B(b, \lambda) - B(b', \lambda)| = \begin{cases} 0 & \text{if } B(b, \lambda) = B(b', \lambda), \\ 2 & \text{if } B(b, \lambda) \neq B(b', \lambda). \end{cases} \tag{1.54}$$

[4]The idea that no influence or signal can propagate faster than the speed of light.

We have then that

$$1 - B(b,\lambda)B(b',\lambda) = |B(b,\lambda) - B(b',\lambda)|, \tag{1.55}$$

and, multiplying it by $\rho(\lambda)$ and integrating over λ, we have

$$\begin{aligned} |P(a,b) - P(a,b')| &\leq \int d\lambda\, \rho(\lambda)\, |B(b,\lambda) - B(b',\lambda)| \\ &= \int d\lambda\, \rho(\lambda)\, [1 - B(b,\lambda)B(b',\lambda)] \\ &= 1 - P(b,b'). \end{aligned} \tag{1.56}$$

Thus,

$$|P(a,b) - P(a,b')| \leq 1 - P(b,b'), \tag{1.57}$$

or, equivalently,

$$1 + P(b,b') \geq |P(a,b) - P(a,b')|. \tag{1.58}$$

The difference between $P(a,b)$ and $P(a,b')$ measures how much the correlations change when Bob switches settings, while Alice stays fixed. The correlation $P(b,b')$ tells us how similar Bob's outcomes are between b and b'. If Bob's outcomes at b and b' are very similar (i.e., $P(b,b')$ close to 1), then changing from b to b' shouldn't affect Alice's correlation very much and $|P(a,b) - P(a,b')|$ must be small. If, on the other hand, Bob's outcomes are maximally different (i.e., $P(b,b') = -1$), then the difference can be as large as possible. This inequality imposes a constraint on local realism: it says you cannot have both strong correlations with two Bob settings and a large difference in Alice's correlations without violating locality. Experimentally, if the inequality is held, this means hidden variables are still a possible element at play. It's violation, however, rules out their presence.

In 1969, U.S.-American physicist John Clauser and colleagues refined Bell's theory in a framework more suitable for actual experiments in what is known as the *CHSH inequality* [79]. In their work they propose the parameter

$$S = P(a,b) - P(a,b') + P(a',b) + P(a',b'), \tag{1.59}$$

and show that the inequality

$$|S| \leq 2 \tag{1.60}$$

is violated in the absence of hidden variables. A year later, Soviet physicist Boris Tsirelson calculated the upper bound on S to be $2\sqrt{2}$ in the case of maximally entangled pairs of particles, as described by equation (1.48), [80].

Experiments in 1972 by U.S.-American physicist Stuart Freedman and Clauser [81], and by French physicists Alain Aspect, Philippe Grangier, and Gérard Roger in 1981 [82], and again by Aspect and Roger now with French physicist Jean Dalibard in 1982 [83], have shown clear violations of Bell's and CHSH inequalities, ruling out the possibility of hidden variables in entangled systems and establishing entanglement as a genuine, albeit counter-intuitive, feature of quantum particles.

We may now return to Ekert's quantum key distribution protocol, E91. In this protocol, Alice can choose between three possible measurement bases (a_1, a_2, a_3) and Bob between two possible bases (b_1, b_2), giving a total of six possible combinations. After the transmission they both share their measurement bases publicly and, when their bases coincide, they obtain perfectly anti-correlated outcomes. By agreeing on one of them to flip their measurement values they can establish the key. Of the remaining measurements, the expectation values $P(a_2, b_1)$, $P(a_2, b_2)$, $P(a_3, b_1)$, and $P(a_3, b_2)$ are used to calculate the correlation parameter S from the CHSH inequality and determine if the qubits used in the key distribution were maximally entangled or not. This allows them to estimate how much information an eavesdropper (Eve) might have gained, as any intervention would degrade the maximal entanglement expected by Alice and Bob.

With an understanding of how quantum information operates in the context of quantum communication, we can now revisit a familiar challenge from classical communication networks: information degradation during transmission. The same vulnerabilities that afflict classical bits transmitted through long channels exist for qubits; that is, environmental noise contamination and data loss due to signal attenuation. For qubits, however, the situation becomes more intricate, as classical repeaters cannot be used to restore quantum information. Using a classical repeater requires measuring the qubit state, collapsing its wave function and destroying the quantum properties - such as superposition and entanglement - that are essential for quantum communication. For this reason, *quantum repeaters* are necessary for the implementation of quantum networks [84–87]. As we saw, the no-cloning theorem prevents the copying of an arbitrary quantum state into a blank state. A quantum repeater must then perform local entanglement generation and entanglement swapping[5] to effectively extend the range of entangled pairs. In the case of a single repeater, two pairs of entangled qubits are generated at the repeater station:

$$|\Psi^+\rangle_{AB} = \frac{1}{\sqrt{2}}(|00\rangle_{AB} + |11\rangle_{AB}). \tag{1.61a}$$

$$|\Psi^+\rangle_{CD} = \frac{1}{\sqrt{2}}(|00\rangle_{CD} + |11\rangle_{CD}). \tag{1.61b}$$

The total state is given by

$$\begin{aligned} |\Psi^+\rangle_{AB} \otimes |\Psi^+\rangle_{CD} = \frac{1}{2}\Big(& |00\rangle_{AB}|00\rangle_{CD} + |00\rangle_{AB}|11\rangle_{CD} \\ & + |11\rangle_{AB}|00\rangle_{CD} + |11\rangle_{AB}|11\rangle_{CD}\Big). \end{aligned} \tag{1.62}$$

State A is meant to be sent to Alice and state D to Bob. These are not, however, entangled yet and must become so without direct interaction. Expressing qubits B

[5] Entanglement purification is also needed from a pragmatic point of view, but its technical complexity lies outside of the scope of this discussion.

and C and A and D in the above expression as Bell states (see equation (1.48)), we have

$$|0\rangle_B |0\rangle_C = \frac{1}{\sqrt{2}}(|\phi^+\rangle_{BC} + |\phi^-\rangle_{BC}), \tag{1.63a}$$

$$|0\rangle_B |1\rangle_C = \frac{1}{\sqrt{2}}(|\psi^+\rangle_{BC} + |\psi^-\rangle_{BC}), \tag{1.63b}$$

$$|1\rangle_B |0\rangle_C = \frac{1}{\sqrt{2}}(|\psi^+\rangle_{BC} - |\psi^-\rangle_{BC}), \tag{1.63c}$$

$$|1\rangle_B |1\rangle_C = \frac{1}{\sqrt{2}}(|\phi^+\rangle_{BC} - |\phi^-\rangle_{BC}). \tag{1.63d}$$

and

$$|0\rangle_A |0\rangle_D = \frac{1}{\sqrt{2}}(|\phi^+\rangle_{AD} + |\phi^-\rangle_{AD}), \tag{1.64a}$$

$$|0\rangle_A |1\rangle_D = \frac{1}{\sqrt{2}}(|\psi^+\rangle_{AD} + |\psi^-\rangle_{AD}), \tag{1.64b}$$

$$|1\rangle_A |0\rangle_D = \frac{1}{\sqrt{2}}(|\psi^+\rangle_{AD} - |\psi^-\rangle_{AD}), \tag{1.64c}$$

$$|1\rangle_A |1\rangle_D = \frac{1}{\sqrt{2}}(|\phi^+\rangle_{AD} - |\phi^-\rangle_{AD}). \tag{1.64d}$$

The total state is then, in the Bell basis,

$$\begin{aligned} |\Psi^+\rangle_{ABCD} = \frac{1}{2}\Big[&|\phi^+\rangle_{BC} |\phi^+\rangle_{AD} + |\phi^-\rangle_{BC} |\phi^-\rangle_{AD} \\ &+ |\psi^+\rangle_{BC} |\psi^+\rangle_{AD} + |\psi^-\rangle_{BC} |\psi^-\rangle_{AD}\Big]. \end{aligned} \tag{1.65}$$

At the repeater, a Bell measurement[6] is then performed on qubits B and C, collapsing them and generating an entangled state between A and D, which is then sent to Alice and Bob.

This process can be extended when additional repeater stations are needed. In the case of two repeaters, R_1 and R_2, for example, R_1 first generates an entangled pair between Alice and itself: particle A is sent to Alice, while particle C_1 is retained by R_1,

$$|\Phi^+\rangle_{AC_1} = \frac{1}{\sqrt{2}}(|0\rangle_A |0\rangle_{C_1} + |1\rangle_A |1\rangle_{C_1}). \tag{1.66}$$

Meanwhile, R_2 generates another entangled pair, consisting of C_2, which is sent to R_1, and D_1, which is kept by R_2:

$$|\Phi^+\rangle_{C_2D_1} = \frac{1}{\sqrt{2}}(|0\rangle_{C_2} |0\rangle_{D_1} + |1\rangle_{C_2} |1\rangle_{D_1}). \tag{1.67}$$

[6]That is, a joint quantum measurement on two qubits in the basis of maximally entangled states, see equation (1.48).

R_2 also creates a second entangled pair, keeping D_2 and sending B to Bob,

$$|\Phi^+\rangle_{D_2B} = \frac{1}{\sqrt{2}}(|0\rangle_{D_2}|0\rangle_B + |1\rangle_{D_2}|1\rangle_B). \tag{1.68}$$

R_1 then performs a Bell-state measurement on C_1 and C_2, which entangles A and D_1. Subsequently, R_2 performs a Bell-state measurement on D_1 and D_2, thereby finally entangling A and B:

$$\underbrace{|\Phi^+\rangle_{AC_1} \otimes |\Phi^+\rangle_{C_2D_1} \otimes |\Phi^+\rangle_{D_2B}}_{\text{Initial}} \overset{\text{Bell}(C_1,C_2)}{\longrightarrow} \underbrace{|\Phi^+\rangle_{AD_1} \otimes |\Phi^+\rangle_{D_2B}}_{\text{After } R_1} \overset{\text{Bell}(D_1,D_2)}{\longrightarrow} |\Phi^+\rangle_{AB}. \tag{1.69}$$

After these successive entanglement swapping steps, Alice and Bob share an entangled pair over a distance for which direct transmission of entangled particles would be otherwise impractical.

Different approaches have been proposed for implementing quantum repeaters. One promising route involves fully optical networks [88]. Unlike matter-based quantum memories (such as spins in quantum dots, trapped ions, or NV centers), purely optical networks do not require long-lived stationary qubits, which are often challenging to realise and suffer from decoherence. Optical networks are also potentially simpler to build, relying primarily on light sources, beam splitters, and detectors, while avoiding the need for cryogenic equipment and magnetic control systems necessary for operating solid-state spins. Furthermore, these networks are naturally compatible with existing optical fibre infrastructure, enabling, in principle, higher speeds since they do not require stationary memories to wait for feedback. Photon loss can also be addressed probabilistically through loss-tolerant coding strategies, providing robustness without the need for memory purification [89].

On the other hand, fully optical networks face significant challenges. They require large photonic cluster states to achieve tolerance to loss and errors, which can be experimentally demanding to generate and control [90, 91]. These networks also rely heavily on multi-photon interference, making photon indistinguishability and precise synchronisation technically challenging. Additionally, deterministic entanglement generation remains difficult: the current method, parametric down-conversion [92, 93], is inherently probabilistic [94, 95], although recent advances in source engineering have shown improvements [96, 97]. They also require high-purity single-photon sources and efficient, low-noise detectors, which are still areas of active development [98].

In contrast, light–matter interaction–based repeaters rely on converting photonic qubits into matter qubits, enabling the quantum state to be effectively ”paused” in a quantum memory. This is crucial for synchronising probabilistic events across long distances [86]. Once stored as matter qubits, local gate operations can be performed with high fidelity, which is essential for entanglement swapping and purification [84, 99]. Many purification protocols require ensembles of locally controlled qubits,

which is straightforward to achieve in matter-based systems. As proposed by Rutger Vrijen and Eli Yablonovitch, photons are ideal carriers for transmitting quantum information, while solid-state systems are optimal for processing it; thus, light–matter interfaces act as a crucial bridge between communication and computation [100].

Despite these advantages, light–matter interaction approaches also present challenges. Memory decoherence remains a fundamental limitation, as matter qubits have finite coherence times, restricting their effective storage time [101]. These systems generally require higher technical complexity, including operation at cryogenic temperatures, high-fidelity gates, and precise coherent optical interfaces. Efficient photon–matter coupling is also challenging to achieve [102]. Finally, heralded entanglement generation and local gate operations are typically slower compared to purely optical systems, potentially limiting overall communication rates.

Of particular interest for the present work is the implementation of quantum dots for repeater technologies. In 2012 Belgian electrical engineer Kristiaan De Greve and his team proposed the use of quantum dot spin-photon entanglement as a quantum communication platform [103]. In the same year W. B. Gao's team achieved entanglement between a quantum dot and a single photon [104]. In 2016 and 2017, Aymeric Delteil's team [105] and R. Stockill's team [106], respectively, achieved the photo-generated entanglement of two spatially-separated quantum dots, with Delteil's team using quantum dot-confined electron holes.

The implementation of quantum dots as a platform for photon-spin conversion rests on the aforementioned seminal work by Vrijen and Yablonovitch [100]. Their idea was to design a photo-detector that could coherently transfer the photon polarisation state to an electron spin state in a semiconductor. In this scenario, the photon excites an electron from the valence band to the conduction band in a quantum dot, creating an *exciton* - an electron-hole pair. The conservation of angular momentum creates selection rules correlating the photon's polarisation to the electron's (hole's) spin, which can be used as a qubit.

In their work, they consider electronic states in Gallium Arsenide (GaAs). In GaAs, the valence band states are described by p-orbitals with orbital angular momentum $l = 1$, giving electrons a total angular momentum of

$$J = L + S = \frac{3}{2}. \tag{1.70}$$

The $j = 3/2$ quadruplet splits into:

- Heavy-holes (HH): $m_j = \pm\frac{3}{2}$
- Light-holes (LH): $m_j = \pm\frac{1}{2}$,

while $j = 1/2$ corresponds to the split-off (SO) band. As for the conduction band, electrons arise from s-like orbitals with $l = 0$, being described solely by their spin $m_s = \pm 1/2$. A right-handed circularly polarised photon σ^+ has an angular momentum $m_j = 1$. We have, therefore, that right-handed photons couple $m_j = -3/2$ valence states to $m_j = -1/2$ conduction band states. Left-handed

photons σ^-, on their turn, have angular momentum $m_j = -1$ and couple $m_j = 3/2$ valence states to $m_j = 1/2$ conduction band states:

$$\sigma^+(m_j = +1) \;\rightarrow\; \left|m_j = -\frac{3}{2}\right\rangle_v \longrightarrow \left|m_j = -\frac{1}{2}\right\rangle_{cb}. \tag{1.71a}$$

$$\sigma^-(m_j = -1) \;\rightarrow\; \left|m_j = +\frac{3}{2}\right\rangle_v \longrightarrow \left|m_j = +\frac{1}{2}\right\rangle_{cb}. \tag{1.71b}$$

For a superposed photon state

$$|\phi\rangle_{ph} = \alpha\,|\sigma^+\rangle + \beta\,|\sigma^-\rangle\,, \tag{1.72}$$

each polarisation state couples to a different valence band state, entangling the photo-generated electrons to their holes, that is,

$$\begin{aligned} |\psi\rangle_{eh} = \alpha \left|m_j = -\frac{3}{2}\right\rangle_h \left|m_j = -\frac{1}{2}\right\rangle_e \\ + \beta \left|m_j = +\frac{3}{2}\right\rangle_h \left|m_j = +\frac{1}{2}\right\rangle_e. \end{aligned} \tag{1.73}$$

This is not, however, an appropriate qubit as it requires the coherence of both the electron and the hole to be kept, lest the interaction of one of them with the rest of the system collapses the whole state. To avoid this issue, both conduction states must be excited from a single valence state. In bulk materials there is a degeneracy between the heavy-holes ($m_j = \pm 3/2$) and the light-holes ($m_j = \pm 1/2$) valence bands at Γ point. This degeneracy can, however, be lifted by straining quantum wells. Tensile-strained quantum wells lift the light-holes band, while compressive-strained quantum wells lift the heavy-holes band. As for the remaining spin degeneracy, it can be removed by the application of a magnetic field.

By applying a magnetic field perpendicularly to the crystal's growth direction, that is, an in-plane magnetic field, the quantisation axis is changed. In the new basis defined by m_j, J_z is no longer diagonal, and the Hamiltonian of the system must be diagonalised in accordance with the new magnetic field orientation (e. g. x). The system's Hamiltonian becomes

$$H_z \propto J_x. \tag{1.74}$$

$|m_j\rangle$ are, however, eigenstates of J_z, not of J_x. By defining the *ladder operators*

$$J_+ |m_j\rangle = \sqrt{(J - m_j)(J + m_j + 1)}\,|m_j + 1\rangle\,, \tag{1.75a}$$

$$J_- |m_j\rangle = \sqrt{(J + m_j)(J - m_j + 1)}\,|m_j - 1\rangle\,, \tag{1.75b}$$

we can write J_x as

$$J_x = \frac{1}{2}(J_+ + J_-). \tag{1.76}$$

Ignoring the heavy holes contribution, for $m_j = \pm\frac{1}{2}$, J_x can be written in this two-dimensional subspace as

$$J_x = \begin{pmatrix} \langle +\frac{1}{2} \left| J_x \right| +\frac{1}{2} \rangle & \langle +\frac{1}{2} \left| J_x \right| -\frac{1}{2} \rangle \\ \langle -\frac{1}{2} \left| J_x \right| +\frac{1}{2} \rangle & \langle -\frac{1}{2} \left| J_x \right| -\frac{1}{2} \rangle \end{pmatrix} \sim \frac{1}{2} \begin{pmatrix} 0 & 1 \\ 1 & 0 \end{pmatrix}. \tag{1.77}$$

Diagonalising this matrix gives us the eigenstates

$$|\psi^+\rangle = \frac{1}{\sqrt{2}} \{ \left| m_j = -\frac{1}{2} \right\rangle + \left| m_j = +\frac{1}{2} \right\rangle \}, \tag{1.78a}$$

$$|\psi^-\rangle = \frac{1}{\sqrt{2}} \{ \left| m_j = -\frac{1}{2} \right\rangle - \left| m_j = +\frac{1}{2} \right\rangle \}, \tag{1.78b}$$

to which photons can couple to with the same amplitude in each case. Considering $|\psi^+\rangle$ as the initial state we have that

$$\sigma^+(m_j = +1) \ \rightarrow \ \left| m_j = -\frac{1}{2} \right\rangle_v \longrightarrow \left| m_s = +\frac{1}{2} \right\rangle_{cb}. \tag{1.79a}$$

$$\sigma^-(m_j = -1) \ \rightarrow \ \left| m_j = +\frac{1}{2} \right\rangle_v \longrightarrow \left| m_s = -\frac{1}{2} \right\rangle_{cb}. \tag{1.79b}$$

Conduction band states can be written (in the logical qubit notation) as

$$|0\rangle = \sqrt{\frac{1}{2}} \{ \left| m_s = -\frac{1}{2} \right\rangle - \left| m_s = \frac{1}{2} \right\rangle \}. \tag{1.80a}$$

$$|1\rangle = \sqrt{\frac{1}{2}} \{ \left| m_s = -\frac{1}{2} \right\rangle + \left| m_s = \frac{1}{2} \right\rangle \}. \tag{1.80b}$$

A photonic state like (1.72) produces then qubits given by

$$|\psi\rangle_{eh} = |\psi^+\rangle_h \left\{ \frac{\alpha}{\sqrt{2}} (|0\rangle + |1\rangle) + \frac{\beta}{\sqrt{2}} (|0\rangle - |1\rangle) \right\}_e. \tag{1.81}$$

We can see their protocol successfully excites a superposition of qubits in the conduction band, while simultaneously factoring out a hole state, which is free to recombine without compromising the coherence of the qubit.

2

Germanium systems

2.1 Material choices

Gate-defined semiconductor quantum dots have been implemented in many different material systems, notably GaAs/AlGaAs (groups III-V) and Si/SiGe and Ge/SiGe (group-IV) heterostructures. Each of these platforms offers distinct physical characteristics which affect quantum dot operation and qubit performance. Below, we compare these systems in terms of their band gaps, and their relation to the telecommunication waveband, their charge carrier mobility, effective masses, spin coherence times, and nuclear spin environments.

Telecommunication waveband compatibility is an important aspect from a practical point of view: the wide implementation of quantum networks is more easily achieved if we can keep the light signal transmission infrastructure we already have in place. GaAs is a direct-bandgap semiconductor, and a $\sim$870 nm wavelength photon is needed to bridge its gap. This value is, however, outside the desired window, which ranges from 1260 nm to 1565 nm. Si has an indirect bandgap requiring $\sim$1100 nm wavelength photons, which also falls short of the *telecomm.* waveband requirements. Its direct gap is even higher in energy, corresponding to a $\sim$360–380 nm wavelength. Ge is also an indirect bandgap semiconductor, bridged by $\sim$1870 nm photons, but its direct bandgap corresponds to a $\sim$1550 nm wavelength, which lies inside the *telecomm.* waveband.

Regarding transport characteristics, high carrier mobility in a 2D quantum well is indicative of low disorder and high-quality quantum dots with well-controlled tunnel couplings and charge stability. It also affects the ease of forming large arrays of dots. Below we compare typical low-temperature mobilities of electrons and holes in these heterostructures.

GaAs/AlGaAs quantum wells display extremely high electron mobilities. In modulation-doped GaAs/AlGaAs heterostructures, electron mobilities can exceed 10^7 cm$^2/V{\cdot}$s at low temperatures. This also reflects its low effective mass ($m_e^* \approx 0.067\ m_e$) and the maturity of GaAs growth techniques. Hole mobilities in GaAs, however, are lower, due to holes' higher effective mass ($m_h^* \approx 0.35 \sim 0.40\ m_e$) and stronger scattering. It can achieve orders of magnitude of $10^4 \sim 10^5$ cm$^2/V{\cdot}$s.

Si/SiGe devices have achieved high mobilities as well, albeit not to the same extent as GaAs/AlGaAs systems. Electrons in clean Si/SiGe 2DEGs can typically

achieve mobilities of $10^5 \sim 10^6$ cm$^2/V$·s at low temperatures. It's worth noticing that Si 2DEG mobility is often limited by interface roughness and residual impurities, not necessarily by phonons, at cryogenic temperatures. Hole mobilities in Si, on the other hand, are much lower, having typical values of 10^4 cm$^2/V$·s. The electronic effective mass in such systems is $\sim$0.19 m_e while holes have an effective mass of $0.25 \sim 0.30\ m_e$.

Contrary to both GaAs/AlGaAs and Si/SiGe heterostructures, Ge/SiGe quantum wells have shown exceptionally high hole mobilities. Holes in Ge have light effective mass ($0.05 \sim 0.10\ m_e$), which, despite the still improvable chemical purity of the crystal, has allowed mobilities of $10^5 \sim 10^6$ cm$^2/V$·s. This is the highest hole mobility in any semiconductor system, rivalling that of electron mobility in Si and GaAs. In contrast, electrons in Ge quantum wells have very low mobilities: 10^4 cm$^2/Vcdot$s with an effective mass of $\sim 0.12\ m_e$.

Finally, let us discuss what is perhaps the most critical characteristic for devices concerned with spin qubits: the spin lifetime. The spin lifetime depends on the materials hyperfine environment, which is governed by nuclei spins, as well as on spin-orbit coupling, which can couple spin to charge noise and phonons, and on valley degeneracies.

Relatively long lifetimes, between 1 and 100 ns, have been achieved for GaAs electrons, despite the presence of nuclear spin: both Ga and As isotopes have nuclear spin $3/2$. For holes in GaAs, the spin lifetime is even shorter. Despite not suffering from hyperfine interactions due to the p-like nature of their wave functions, they have a strong spin-orbit coupling and spin lifetimes peaking at 100 ps.

Si/SiGe quantum wells have exceptionally long coherence times when enriched with spin-zero isotopes. ^{28}Si and ^{30}Si have 0 nuclear spin, and even ^{28}Si, which has nuclear spin 1/2, provides a better landscape than GaAs. For electrons the spin lifetime has been measured to range between 1 and 10 μs, while for holes it peaks at 10 ns, due to strong spin-orbit interaction.

Ge/SiGe quantum wells have emerged as a promising host option for hole spin qubits, precisely because it offers strong spin-orbit coupling and a quiet nuclear environment. Of all the five naturally occurring isotopes of Ge, only ^{73}Ge has a nuclear spin of 9/2, while ^{70}Ge, ^{72}Ge, ^{74}Ge, and ^{76}Ge have zero nuclear spin. This makes the hyperfine noise in the environment weak. Additionally, heavy holes in Ge have a predominantly p-orbital character at atomic sites, further suppressing Fermi-contact hyperfine interactions. The spin coherence is then limited, primarily by charge noise and device imperfections. The spin lifetimes for Ge holes can range from 100 to 500 ns.

In summary, while GaAs/AlGaAs served as a crucial "learning ground" for spin qubits, its intrinsic limitations (omnipresent nuclear spins, not *telecomm.*-friendly) make it less suitable for large-scale quantum computers and networks. Si/SiGe has become a front-runner for spin qubits that prioritise long coherence and integration with classical electronics, which is ideal for dense quantum processors with error correction. On the other hand, Ge/SiGe is emerging as a compelling alternative with potentially faster qubit gates and native photonic interfacing while still retaining

long coherence through nuclear-spin-free isotopes. These results are summarised in Table 2.1.

Properties	**GaAs/AlGaAs**	**Si/SiGe**	**Ge/SiGe**
Bandgap	∼870 nm	1100 nm (indirect) 365 nm (direct)	1875 nm (indirect) 1550 nm (direct)
Mobility ($cm^2/V{\cdot}s$)	10^7 (e^-) $10^4 \sim 10^5$ (h^+)	$10^5 \sim 10^6$ (e^-) 10^4 (h^+)	10^4 (e^-) $10^5 \sim 10^6$ (h^+)
Effective mass (m_e)	$m_e^* \approx 0.067$ $m_h^* \approx 0.35 \sim 0.40$	$m_e^* \approx 0.19$ $m_h^* \approx 0.25 \sim 0.30$	$m_e^* \approx 0.12$ $m_h^* \approx 0.05 \sim 0.10$
Spin lifetime	$1 \sim 100$ ns (e^-) $0 \sim 100$ ps (h^+)	$1 \sim 10$ μs (e^-) $0 \sim 10$ ns (h^+)	$1 \sim 10$ ns (e^-) $100 \sim 500$ ns (h^+)
Nuclear spin	Every stable isotope has nuclear spin	0 for ^{28,30}Si 1/2 for ^{29}Si	0 for ^{70,72,74,76}Ge 9/2 for ^{73}Ge

Table 2.1: Comparison between material properties for different quantum well systems.

2.1.1 Persistent photo-conductivity

From the previous section we can draw the conclusion that Ge is the best suited material candidate for photon-spin interface technologies. There is, however, one more important characteristic involving light-matter interactions which must be checked: **Persistent photo-conductivity** (PPC). This phenomenon, observed primarily in GaAs/AlGaAs, refers to a long-lived photo-induced increase in charge carriers, which persists long after the illumination source has been turned off. In GaAs quantum wells, PPC comes from photo-induced carrier de-trapping at certain defect states. The two main contributors are DX centres in the AlGaAs barrier (associated with donor impurities like Si), and deep-level traps in the GaAs (such as Arsenic-antisite defects). These defects can trap charge carriers and have metastable configurations that lead to PPC.

DX centres are deep donor states in AlGaAs that form when a donor atom undergoes lattice relaxation. It acquires, in the process, a negative charge by capturing an electron. At low temperatures, many donors become neutral or negatively charged,

reducing the free electron density. Illumination can excite these trapped electrons into the conduction band, suddenly increasing the free carrier density. Crucially, once emptied by light, a DX centre has a large capture barrier and cannot easily recapture an electron at low temperature. In essence, the donor remains ionized and the liberated electron stays in the 2DEG, so the photo-conductivity persists until thermal energy is supplied. This behavior – carrier freeze-out in the dark and persistent ionisation under illumination – is the hallmark of DX centres. Deep-level traps, on their turn, have been experimentally detected in the GaAs layer itself (as well as at the interface with AlGaAs) and cause similar metastable states which are shielded against charge recombination. This is contrastive with ordinary photo-conductivity where the exciton pair quickly recombine once illumination ceases. Quantitatively, studies have shown that short light irradiation times can nearly double the carrier density in modulation-doped GaAs quantum wells. This order of magnitude remains typical – the sheet density is boosted by a factor of $\sim$2–3 in many cases. The effect tends to saturate after ionising the available traps: once most DX centres or deep traps have been emptied by light, further illumination yields diminishing increments in carrier density. Notably, the persistent fraction of photo-generated carriers can depend on specifics like dopant concentration and illumination history.

The consequences of this phenomenon, in particular for device operation are of great importance. Particularly for quantum dots, the increase in the background carrier concentration raises the Fermi level of the 2DEG, shifting threshold values of the gates. In relation to dot occupancy, after illumination, a given quantum dot will hold more electrons at the same gate voltages, requiring frequent adjustments. In essence, the device's whole band structure is affected and thermal cycling is required to *reset* it. Typically, quantum dot qubits or Coulomb blockade measurements are performed in the dark (after an initial illumination) to avoid photon-induced noise. Continuous above-band gap illumination would generate non-equilibrium electrons and holes that could tunnel into the dot or screen the gates unpredictably.

While photo-spin conversion has been successfully performed in GaAs/AlGaAs quantum dots, PPC is another reason for looking for a different material for scalable quantum photo-spin conversion interfaces. As Ge checks many of the other boxes for efficient implementation of such interfaces, it is important to look for this phenomenon in Ge as well.

2.2 Material properties of Germanium

Germanium is a period 4 semiconductor of the Carbon group (group 14), with atomic number $Z = 32$. It has five stable isotopes: ^{70}Ge, ^{72}Ge, ^{73}Ge, ^{74}Ge, and ^{76}Ge. It crystallises in the diamond-cubic structure, identical to that of Silicon and diamonds, see Figure 2.1. This structure can also be described as two inter-penetrating face-centred cubic (FCC) sublattices, displaced by one quarter of the body diagonal vector. At room temperature, Ge has a lattice constant a of approximately 5.658 Å, which is about 4.2% larger than that of Si. The FCC lattice primitive vectors can be expressed

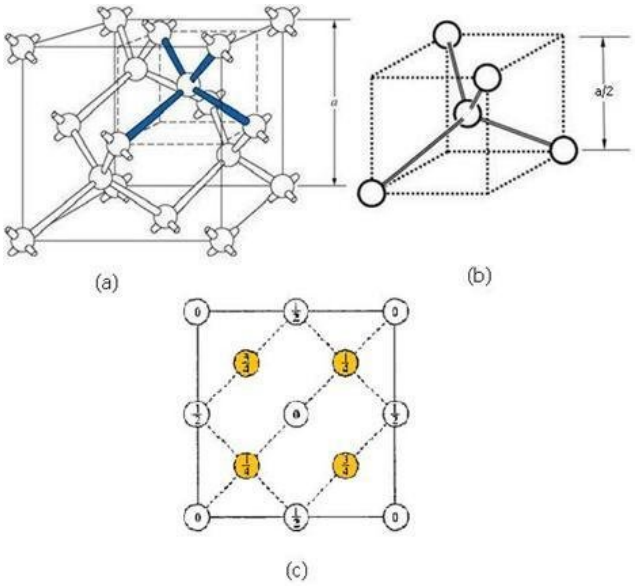

FIGURE 2.1: **Ge crystal lattice:** (a) Diamond-cubic crystal structure. (b) Closest neighbours tetrahedron structure. (c) Bird-eye view of the structure. *Source:* [107]

as

$$\mathbf{a}_1 = \frac{a}{2}(0,1,1), \quad \mathbf{a}_2 = \frac{a}{2}(1,0,1), \quad \mathbf{a}_3 = \frac{a}{2}(1,1,0). \tag{2.1}$$

Each lattice point has a two-atom basis, with basis vectors given by

$$\mathbf{0} = (0,0,0), \qquad \mathbf{d} = \left(\frac{1}{4}, \frac{1}{4}, \frac{1}{4}\right) a. \tag{2.2}$$

The atomic positions in the crystal are given by

$$\mathbf{R} = n_1\mathbf{a}_1 + n_2\mathbf{a}_2 + n_3\mathbf{a}_3 + \mathbf{d}, \tag{2.3}$$

where n_i are integers running over all lattice points, and $\mathbf{d}$ takes the values $\mathbf{0}$ and $\left(\frac{1}{4}, \frac{1}{4}, \frac{1}{4}\right) a$. Each atom in the lattice is tetrahedrally coordinated, meaning they have four nearest neighbours at a distance

$$d = \frac{\sqrt{3}}{4} a. \tag{2.4}$$

For Ge, $d \approx 2.45$ Å. These neighbours' bonds are formed via an sp^3-hybridised tetrahedral network, resulting in strong covalent bonding throughout the crystal, see Figure 2.2. The lattice exhibits a highly symmetrical crystal structure, belonging to space group $Fd\bar{3}m$ (No. 227) and to point group O_h[1]. It presents, amongst its symmetries, inversion, mirror planes, and roto-inversion. Its centre-symmetry, in particular, prohibits certain optical and electrical effects in the bulk, such as piezoelectricity and second-order nonlinear optical phenomena. Its reciprocal lattice

[1] Octahedral symmetry

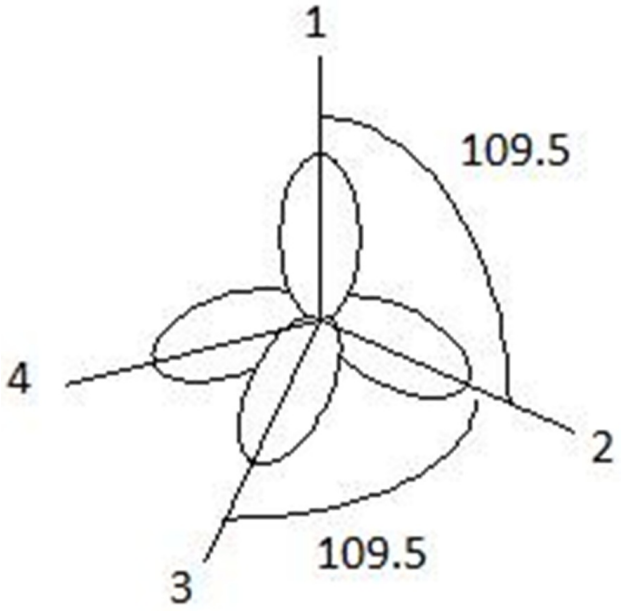

FIGURE 2.2: sp^3 **hybridisation in Ge:** Tetrahedral bonding network characteristic of the diamond-cubic structure.

is body-centred cubic (BCC), with primitive reciprocal lattice vectors given by

$$\mathbf{b}_1 = \frac{2\pi}{a}(-1,1,1), \qquad \mathbf{b}_2 = \frac{2\pi}{a}(1,-1,1), \qquad \mathbf{b}_3 = \frac{2\pi}{a}(1,1,-1). \tag{2.5}$$

Figure 2.3 shows Ge's band-structure. We can see the valence maximum is located at Γ point, while the conduction minimum is located at L point, making Ge an indirect band-gap semiconductor. At L point, the band-gap is approximately 0.66 eV, while the direct gap at Γ point is approximately 0.80 eV. At Γ point, degenerate valence Heavy-hole (HH) and Light-hole (LH) subbands can be found, as well as the Split-off (SO) subband, which is separated from the others by a spin-orbit splitting energy of approximately 0.29 eV. The strong spin-orbit coupling in the valence band plays an important role in defining spin dynamics and optical selection rules.

Ge has a Debye temperature of approximately 374K. This temperature indicates the capping at which all vibrational modes are excited. Its thermal conductivity is relatively low compared to Si, due to its heavier atomic mass and lower phonon group velocities. Due to having two atoms per primitive cell, Ge exhibits three acoustic and three optical phonon branches. The optical phonon frequency at the Γ point is approximately 300 cm^{-1} (around 37 meV). Due to its cubic symmetry, longitudinal optical (LO) and transverse optical (TO) phonons are degenerate at Γ.

From an optical perspective, the absorption edge corresponds to the indirect band gap. Ge possesses a high refractive index, approximately 4.0 around 1.5 μm. It absorbs much of the visible spectrum but remains transparent in the mid-infrared, making it attractive for infrared optics.

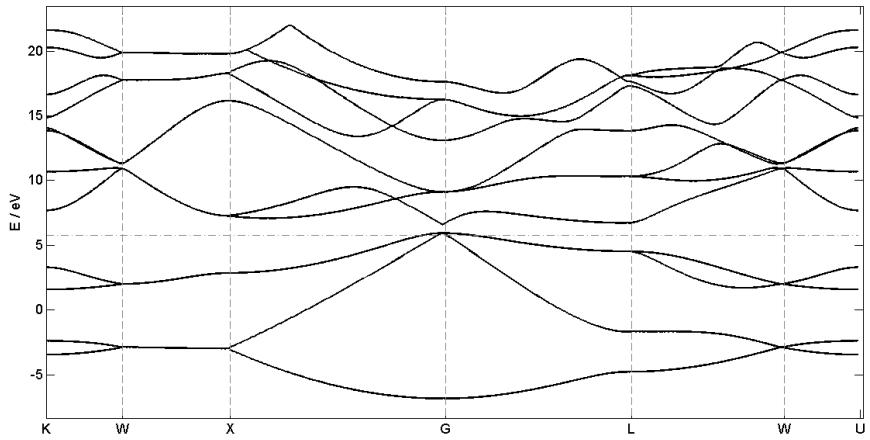

FIGURE 2.3: **Ge bandstructure**. Bandstructure of bulk Ge.

Mechanically, Ge is more brittle than Si and tends to form point defects such as vacancies, interstitials, and antisites. Self-interstitials and vacancies in Ge can readily migrate at elevated temperatures, impacting diffusion processes. It can be n-type doped by Sb or P, and p-type doped by B or Ga. Due to its small band gap, it exhibits a high intrinsic carrier concentration.

Finally, Ge's electronic band-structure is highly sensitive to strain. Tensile strain reduces the Γ-L conduction band energy separation, enhancing direct-gap transitions. Conversely, compressive strain can elevate the heavy-hole band above the light-hole band, thus modifying optical transition probabilities.

2.3 Spin-orbit coupling and g-factor tunability

Spin-orbit coupling (SOC) arises from the relativistic interaction between an electron's spin and its orbital motion. In the electron's rest frame, electric fields $\mathbf{E}$ transform into an effective magnetic field $\mathbf{B}'$ given by

$$\mathbf{B}' = -\frac{\mathbf{v} \times \mathbf{E}}{c^2}, \tag{2.6}$$

where $\mathbf{v}$ is the velocity of the lab frame in relation to the electron's rest frame, and c is the speed of light. The electron's magnetic moment μ_s couples to this field via the spin-orbit (SO) Hamitonian

$$H_{\mathrm{SO}} = -\mu_s \cdot \mathbf{B}'. \tag{2.7}$$

For an electron in a single atom, the electric field is given by the central Coulomb potential $V(\mathbf{r})$ through

$$\mathbf{E} = -\nabla V(\mathbf{r}). \tag{2.8}$$

Writing then $\mathbf{v}$ in terms of the momentum $\mathbf{p}$, $\mathbf{v} = \frac{\mathbf{p}}{m_0}$, where m_0 is the electron's mass, we have the effective magnetic field as

$$\mathbf{B}' = -\frac{\mathbf{v} \times \mathbf{E}}{c^2} = -\frac{1}{m_0 c^2}\,\mathbf{p} \times (-\nabla V) = \frac{1}{m_0 c^2}\,(\nabla V \times \mathbf{p}). \tag{2.9}$$

The magnetic moment operator is given by

$$\mu_{_s} = -\frac{g_s \mu_B}{\hbar}\mathbf{S} = -\frac{e\hbar}{2m_0 c}\sigma, \tag{2.10}$$

where μ_B is Bohr's magneton, e is the electronic charge and σ are the Pauli matrices. Since the orbital angular momentum operator is defined as $\mathbf{L} = \mathbf{r} \times \mathbf{p}$, we can write, for a central potential,

$$\nabla V \times \mathbf{p} = \frac{1}{r}\frac{dV}{dr}\mathbf{L}. \tag{2.11}$$

Finally, replacing equations (2.9) through (2.11) in equation (2.7), the atomic SO Hamiltonian can be written as

$$H_{\text{SO}} = \frac{\hbar}{4m_0^2 c^2}\,\frac{1}{r}\frac{dV}{dr}\,\mathbf{L} \cdot \sigma. \tag{2.12}$$

As the name suggests, this phenomenon couples the spin angular momentum $\mathbf{S}$ with the orbital angular momentum $\mathbf{L}$, resulting in the total angular momentum $\mathbf{J}$,

$$\mathbf{J} = \mathbf{L} + \mathbf{S}, \tag{2.13}$$

which becomes the relevant quantum number, with allowed eigenstates labelled by $j = l \pm \frac{1}{2}$.

Using first-order perturbation theory, the energy correction due to SOC is,

$$\Delta E_{\text{SO}} = \frac{\hbar^2}{2m_0^2 c^2}\left\langle \frac{1}{r}\frac{dV}{dr} \right\rangle \langle \mathbf{L} \cdot \mathbf{S} \rangle, \tag{2.14}$$

where

$$\langle \mathbf{L} \cdot \mathbf{S} \rangle = \frac{\hbar^2}{2}\big[j(j+1) - l(l+1) - s(s+1)\big]. \tag{2.15}$$

The same formalism can be used for crystals, with the difference that now the effective magnetic field $\mathbf{B}'$ is created by periodic potentials $V(\mathbf{r}) = V(\mathbf{r} + \mathbf{R})$. Such potentials are not central, and, rigorously, the crystal SOC Hamiltonian is given by

$$H_{\text{SO}} = \frac{\hbar}{4m_0^2 c^2}(\nabla V(\mathbf{r}) \times \mathbf{p}) \cdot \sigma. \tag{2.16}$$

Near atomic sites, however, and at Γ point, the potential can be approximated to a nearly central one, and H_{SO} can be written as

$$H_{\text{SO}} \approx \lambda \mathbf{L} \cdot \mathbf{S}, \tag{2.17}$$

where

$$\lambda = \frac{\hbar}{4m_0^2c^2}\left\langle \frac{1}{r}\frac{dV}{dr}\right\rangle . \tag{2.18}$$

This makes clear how this Hamiltonian acts on angular momentum states. It also explains how the HH-LH degeneracy is lifted at Γ point. For $\mathbf{k} = 0$, the periodic potential Hamiltonian (excluding SOC) H_0 yields p-like orbitals with $l = 1$. Accounting for spin, this results in six degenerate states. By incorporating SOC, l and s must be combined via

$$j = l \pm s \rightarrow j = \frac{3}{2} \quad \text{and} \quad j = \frac{1}{2}, \tag{2.19}$$

yielding

$$m_j = \pm\frac{3}{2},\ \pm\frac{1}{2}. \tag{2.20}$$

For $j = \frac{3}{2}$, four states are possible, $|m_j = \pm 3/2\rangle$ (HH) and $|m_j = \pm 1/2\rangle$ (LH). For $j = \frac{1}{2}$, two states are possible, $|m_j = \pm 1/2\rangle$ (SO). The energies associated with these states are given by

$$E_{3/2} = \frac{\lambda}{2}\hbar^2, \quad E_{1/2} = -\lambda\hbar^2, \tag{2.21}$$

with the spin-orbit splitting energy given then by

$$\Delta_{\text{SO}} = E_{(1/2)} - E_{(3/2)}. \tag{2.22}$$

The strength of the SOC scales strongly with the atomic number Z as $\lambda \propto Z^4$. For Ge ($Z = 32$), this results in a spin-orbit splitting energy of ~ 0.29 eV[2].

By using $\mathbf{k} \cdot \mathbf{p}$ perturbation theory, the full Hamiltonian (taking into account SOC and $\mathbf{k} \neq \mathbf{0}$ effects), can be written as an effective, semi-empiric Luttinger-Kohl Hamiltonian:

$$H_v = -\frac{\hbar^2}{2m_0}\Big[\left(\gamma_1 + \frac{5}{2}\gamma_2\right)k^2 - 2\gamma_2\sum_i k_i^2 J_i^2 - 4\gamma_3\sum_{i\neq j} k_i k_j \{J_i, J_j\}\Big], \tag{2.23}$$

where γ_1, γ_2, and γ_3 are Luttinger parameters, which represent second-order perturbative corrections in $\mathbf{k} \cdot \mathbf{p}$ theory involving virtual coupling to remote bands. These parameters are usually determined experimentally.

SOC can also play a part in spin relaxation. In crystals, it causes Bloch states to no longer be pure spin eigenstates. Instead, each eigenstate becomes a mixture of spin up and down,

$$|\psi_n(\mathbf{k})\rangle = a_n(\mathbf{k})|\uparrow\rangle + b_n(\mathbf{k})|\downarrow\rangle, \tag{2.24}$$

[2]Strong SOC is also responsible for phenomena like topological insulators, where spin-momentum locking occurs at surfaces.

with coefficients $a_n(\mathbf{k})$ and $b_n(\mathbf{k})$ depending on the crystal momentum **k** and on the strength of the coupling. In the presence of SOC, even if the scattering potential is spin-independent, the Bloch eigenstates have a mixed spin character. When an electron scatters (off phonons or impurities, for example), its total wave-function changes, and because of the mixed spin content, spin flips can occur indirectly.

The so-called *Yafet correction* accounts for explicit spin-flip terms in the scattering matrix elements, such as contributions from the spin-dependent part of the potential or additional SOC effects during scattering. This correction is particularly important at lower temperatures or in materials with strong SOC. Furthermore, at higher temperatures, the increased number of phonons enhances scattering events and reduces the momentum relaxation time, thereby accelerating spin relaxation.

So far, the g-factor has been introduced in a subtle manner, but it is of crucial importance for the discussion. The g-factor quantifies the coupling between a charge carrier's angular momentum and external magnetic fields **B**. A free electron, for example, has no orbital angular momentum contribution to its magnetic moment, so it couples to **B** via its spin. In a crystal, however, this coupling involves the total angular momentum, which depends on the crystalline structure itself. For this reason, since crystals are not necessarily isotropic, the coupling can change depending on the direction of **B** in relation to the lattice. This leads to anisotropic g-tensors, as we can see from the Zeeman Hamiltonian

$$\mathcal{H}_Z = \mu_B \mathbf{B} \cdot \mathbf{g} \cdot \mathbf{S} = \mu_B \begin{bmatrix} B_x & B_y & B_z \end{bmatrix} \begin{bmatrix} g_{xx} & g_{xy} & g_{xz} \\ g_{yx} & g_{yy} & g_{yz} \\ g_{zx} & g_{zy} & g_{zz} \end{bmatrix} \begin{bmatrix} S_x \\ S_y \\ S_z \end{bmatrix}. \tag{2.25}$$

In Ge, the conduction band has s-like orbitals with $l = 0$, and so, their effective g-factor is nearly isotropic. Holes in the valence band, however, have strongly anisotropic g-tensors, since they have significant angular momenta with different projections along different directions.

This dependency of the g-factor (tensor) on the structure of its environment is what allows for its tuning. Low-dimensional systems, such as quantum wells (2D), quantum wires (1D), and quantum dots (0D), break the bulk symmetries and modify the energy bands, directly influencing how charge carriers couple to magnetic fields. Anisotropic strain (either tensile or compressive) on the crystal also influences the g-tensor for the same reason: it modifies the environment, breaking symmetries and altering the energy band.

This effect can also be controllably achieved via the application of an electric field along the growth direction of the crystal. This is known as the Rashba effect. For an electric field given by

$$\nabla V \approx eE_z\hat{z}, \tag{2.26}$$

and by noticing that, for a 2D system, $\mathbf{p} = \hbar\mathbf{k}$, we have, from equation (2.16), the Rashba Hamiltonian as

$$H_R = \alpha_R(\mathbf{k} \times \mathbf{E}) \cdot \mathbf{J}, \tag{2.27}$$

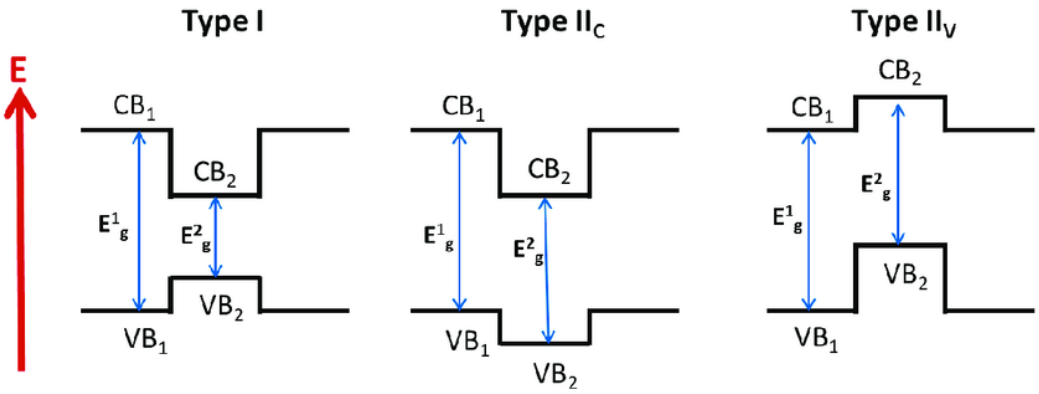

FIGURE 2.4: **Quantum well types:** *Type I*: Both electrons and holes are confined in the same material. The conduction band minimum (CBM) and valence band maximum (VBM) of the well material lie within those of the barrier material. *Type II_c*:Electrons are confined in the well, while holes are in the barrier. *Type II_v*: Holes are confined in the well, while electrons are in the barrier. *Source:* [108]

where

$$\alpha_R = \frac{e\hbar^2\langle E_z\rangle}{4m_0^2c^2}, \tag{2.28}$$

is the Rashba coefficient. As we can see, this Hamiltonian depends on the total angular momentum, as l and s have already been coupled by the intrinsic spin-orbit Hamiltonian. The Rashba Hamiltonian modifies these states, however, changing the expectation value of **J** and, consequently, changing the g-tensor as well.

2.4 Fundamentals of quantum wells

Quantum wells (QW) are perhaps one of simplest non-trivial quantum systems Quantum Mechanics' students are introduced to. While introductory textbooks usually treat them as an almost abstract system, without mention of real world implementations, in practice, quantum wells are built from thin layers of semiconductor materials with a lower band gap, sandwiched between two layers of materials with higher band gaps. This band off-set confines charge carriers, serving as barriers. Ge quantum wells are, for example, usually placed in between SiGe barriers.

When two semiconductors are joined, their conduction and valence band edges form discontinuities known as band offsets. In type-I wells, both electrons and holes are confined in the well. In type-II, electrons and holes are confined in different layers, see Figure 2.4. In a thin well (usually of a few nm), charge carriers are confined along the growth direction, but remain free to move in-plane. This confinement leads to quantised energy levels, similar to the familiar particle-in-a-box problems. In a simple one-dimensional infinite barrier approximation,

$$E_n = \frac{\hbar^2 \pi^2 n^2}{2m^* \mathrm{L}_z^2}, \tag{2.29}$$

where n is the quantised energy level, m^* is the effective mass in the confinement direction and L_z is the width of the well. In the two-dimensional case,

$$E_n(k_x, k_y) = E_n + \frac{\hbar^2 (k_x^2 + k_y^2)}{2m^*}. \tag{2.30}$$

In bulk semiconductors, the conduction band edge E_c defines the minimum energy for free electrons. In a quantum well,

$$E_{c,n} = E_c^{\text{bulk}} + E_n, \tag{2.31}$$

where E_n is the quantised confinement energy. Similarly, for holes in the valence band,

$$E_{v,n} = E_v^{\text{bulk}} - E_n', \tag{2.32}$$

where E_v^{bulk} is the valence band edge and E_n' is the confinement energy for holes, which depends on the hole effective mass m_h^*. Assuming the confinement happens along the z-axis, carriers are still free to move in the x, y directions. Their total energy is then

$$E(\mathbf{k}_\parallel) = E_n + \frac{\hbar^2 \mathbf{k}_\parallel^2}{2m^*}, \tag{2.33}$$

where $\mathbf{k}_\parallel$ is the in-plane wave vector. We see then that each discrete n-level forms a two-dimensional subband dispersion. Because of the confinement energies E_n and E_n', the effective band-gap of the well increases:

$$E_g^{\text{QW}} = E_c^{\text{bulk}} - E_v^{\text{bulk}} + E_n + E_n'. \tag{2.34}$$

This is the reason why quantum wells often exhibit blue-shifted photo-luminescence when compared to the bulk material.

2.5 Photo-spin conversion mechanisms

We have already seen in the ***Introduction*** a little about how photo-spin conversions work based on Vrijen's and Yablonovitch's work [100]. Nevertheless, let us now, for the sake of completeness, discuss photo-spin conversion mechanism in more detail. In particular in relation to Ge quantum wells.

Photons can be polarised linearly or elliptically. From a classical perspective, this corresponds to the oscillation direction of the electric field. If it oscillates along the $\hat{\boldsymbol{\epsilon}}$ direction, light is said to be $\hat{\boldsymbol{\epsilon}}$-polarised. If the oscillation direction changes, however, such that the oscillation maxima trace an ellipse on the plane perpendicular to the propagation direction, light is said to be elliptically-polarised. In the special case where the ellipse has its semi-major axis in equal length to its semi-minor axis, light

is said to be circularly-polarised. A circularly polarised photon carries an angular momentum of $\pm\hbar$, where $\sigma^+ = +\hbar$ is called a right-hand circular polarisation and $\sigma^- = -\hbar$ a left-hand circular polarisation.

The interaction of electromagnetic radiation with charge carriers is described by the coupling Hamiltonian

$$H = \frac{1}{2m}\big(\mathbf{p} + e\mathbf{A}(\mathbf{r},t)\big)^2 + V(\mathbf{r}), \tag{2.35}$$

where $\mathbf{A}(\mathbf{r},t)$ is the vector potential, which is connected to the electromagnetic fields via

$$\mathbf{E} = -\nabla\phi - \frac{\partial \mathbf{A}}{\partial t}, \qquad \mathbf{B} = \nabla \times \mathbf{A}, \tag{2.36}$$

being ϕ the scalar potential. These potentials are not uniquely defined and can be transformed via gauge transformations,

$$\mathbf{A}' = \mathbf{A} + \nabla\Lambda, \quad \phi' = \phi - \frac{\partial \Lambda}{\partial t}, \tag{2.37}$$

without affecting the physical fields **E** and **B**. Expanding the interaction term in the Hamiltonian we obtain

$$\frac{1}{2m}\big(\mathbf{p} + e\mathbf{A}\big)^2 = \frac{\mathbf{p}^2}{2m} + \frac{e}{2m}(\mathbf{p}\cdot\mathbf{A} + \mathbf{A}\cdot\mathbf{p}) + \frac{e^2\mathbf{A}^2}{2m}. \tag{2.38}$$

By considering weak electromagnetic fields, $\mathbf{A}^2$ can be ignored. If the wavelength of the incident light is much larger than the relevant atomic scale (e.g. the lattice constant a), the spatial part of its plane-wave description can be approximated to

$$e^{i\mathbf{k}\cdot\mathbf{r}} \approx 1 + i\mathbf{k}\cdot\mathbf{r} + \dots . \tag{2.39}$$

This means the spatial variation of the field over the electronic wave-functions is negligible and we can approximate the field as being spatially uniform (over the unit cell):

$$\mathbf{A}(\mathbf{r},t) \approx \mathbf{A}(t). \tag{2.40}$$

In the Coulomb gauge ($\nabla \cdot \mathrm{A}$, $\phi = 0$), we have then that

$$\mathbf{E}(t) = -\frac{\partial \mathbf{A}(t)}{\partial t}, \tag{2.41}$$

which is independent of **r**, making **p** and **A** commutable. The interaction Hamiltonian is then:

$$H' = \frac{e}{m}\mathbf{p}\cdot\mathbf{A}. \tag{2.42}$$

Now, this is not the total Hamiltonian, which is given by

$$H = H_0 + H' \quad , \quad H_0 = \frac{1}{2m}\mathbf{p}^2 + V(\mathbf{r}). \tag{2.43}$$

The light interaction is, however, being treated perturbatively, meaning the actual eigenstates are small deviations of the eigenstates of H_0. For H_0, the following relation is valid:

$$\mathbf{p} = \frac{im}{\hbar}[H_0, \mathbf{r}]. \tag{2.44}$$

Assuming then its approximate validity, and assuming an harmonic field of angular frequency ω, $A(t) = A_0 e^{-i\omega t}$, such that

$$\mathbf{A}(t) = \frac{-i}{\omega}\mathbf{E}(t), \tag{2.45}$$

where equation (2.41) was used, we have

$$H' = \frac{e}{\hbar\omega}[H_0, \mathbf{r}] \cdot \mathbf{E}. \tag{2.46}$$

Using this Hamiltonian to connect a valence eigenstate $|v\rangle$ to a conduction eigenstate $|c\rangle$ of H_0 we have

$$\langle c| \left[H_0, \mathbf{r}\right] \cdot \mathbf{E} \, |v\rangle = \left(E_c - E_v\right) \langle c| \, \mathbf{r} \cdot \mathbf{E} \, |v\rangle \, . \tag{2.47}$$

Now, energy conservation demands the photon's energy is equal to the gap the charge must bridge to go from $|v\rangle$ to $|c\rangle$, that is,

$$\hbar\omega = E_c - E_v. \tag{2.48}$$

The interaction Hamiltonian in the electric dipole approximation is then

$$H' = \mathbf{d} \cdot \mathbf{E}, \tag{2.49}$$

where

$$\mathbf{d} = e\mathbf{r}. \tag{2.50}$$

This first order coupling of **d** and **E** is what gives this perturbative approach the ***electric dipole approximation*** name. For Ge, the band-gap lies in the telecommunication waveband - 1.3μm $\sim$ 1.6μm - which is from over 2000 to nearly 3000 times longer than the lattice constant. The electric dipole approximation is then valid on this case.

Transition probability amplitudes are given by the transition matrix elements

$$M_{cv} = \langle c|H'|v\rangle = e\langle c|\mathbf{E} \cdot \mathbf{r}|v\rangle. \tag{2.51}$$

The photon polarisation is usually incorporated via the polarisation vector **e**, giving us

$$M_{cv} \propto \langle c|\mathbf{e} \cdot \mathbf{r}|v\rangle. \tag{2.52}$$

For circularly polarised light propagating along the z-direction, polarisation vectors are defined as

$$\sigma^+ = \frac{1}{\sqrt{2}}\left(\mathbf{e}_x + i\mathbf{e}_y\right) \quad \text{(right-handed)}, \tag{2.53a}$$

$$\sigma^- = \frac{1}{\sqrt{2}}\left(\mathbf{e}_x - i\mathbf{e}_y\right) \quad \text{(left-handed)}. \tag{2.53b}$$

By adding $\sigma^0 = \mathbf{e}_z$ to these equations, we have a complete spherical basis for describing photonic polarisation: $\sigma^{\pm,0} = \{\sigma^+, \sigma^0, \sigma^-\}$. In this spherical basis $\sigma^{\pm,0}$ forms a rank-1 spherical tensor, with the right-handed polarisation being simply $\sigma^+ = (1,0,0)$, and the left-handed polarisation $\sigma^- = (0,0,1)$. The spatial operator $\mathbf{r}$ can be rewritten in a similar fashion,

$$r_+ = \frac{1}{\sqrt{2}}(x+iy), \quad r_- = \frac{1}{\sqrt{2}}(x-iy), \quad r_0 = z. \tag{2.54}$$

forming another rank-1 spherical tensor $\mathbf{r}_{\pm,0} = r_q$. This allows us to use the *Wigner-Eckart theorem* to calculate the optical transition selection rules.

Theorem 2.5.1 (Wigner-Eckart theorem) *The matrix elements of a spherical tensor operator $T_q^{(k)}$ between angular momentum eigenstates can be factorized as*

$$\langle j', m'|T_q^{(k)}|j, m\rangle = \langle j, m; k, q|j', m'\rangle \langle j'||\mathbf{T}^{(k)}||j\rangle, \tag{2.55}$$

where $\langle j, m; k, q|j', m'\rangle$ is a Clebsch–Gordan coefficient and $\langle j'||T^{(k)}||j\rangle$ is the reduced matrix element, which is independent of m and q.

The Clebsch-Gordan coefficients are given by

$$\begin{aligned}\langle j, m; k, q|j', m'\rangle = \delta_{m',m+q}&\sqrt{\frac{(2j'+1)(j'+j-k)!(j'-j+k)!(j-j'+k)!}{(j+k+j'+1)!}} \\ &\times \sqrt{(j'+m')!(j'-m')!(j-m)!(j+m)!(k-q)!(k+q)!} \\ &\times \sum_t \frac{(-1)^t}{t!(j+k-j'-t)!(j-m-t)!(k+q-t)!} \\ &\times \frac{1}{(j'-k+m+t)!(j'-j-q+t)!}.\end{aligned} \tag{2.56}$$

The Wigner-Eckart theorem addresses the components of a spherical tensor operator. In our case this is $\mathbf{r}_{\pm,0}$, as $^{\pm,0}$ is not an operator, but a rank-1 spherical tensor characterising the photon's circular polarisation. Considering that, for two tensors $\mathbf{T}^{(k)}$ and $\mathbf{U}^{(k)}$,

$$\mathbf{T}^{(k)} \cdot \mathbf{U}^{(k)} = \sum_q (-1)^q T_{-q}^{(k)} U_q^{(k)}, \quad \text{with } q = 0, \pm 1, \tag{2.57}$$

we have that

$$\begin{aligned}\langle j_2, m_2|\sigma^{\pm,0} \cdot \mathbf{r}_{\pm,0}|j_1, m_1\rangle &= \sum_q (-1)^q \sigma^{-q} \langle j_2, m_2|r_q|j_1, m_1\rangle \\ &= \sum_q (-1)^q \sigma^{-q} \langle j_1, m_1; 1, q|j_2, m_2\rangle \langle j_2||\mathbf{r}_{\pm,0}||j_1\rangle\end{aligned} \tag{2.58}$$

From equation (2.56) we can readily observe the **first optical transition selection rule**:

$$\boxed{m_2 = m_1 + q} \tag{2.59}$$

From the numerator of the first square-rooted term in equation (2.56) we have the term

$$(j_2 + j_1 - 1)!\,(j_2 - j_1 + 1)!\,(j_1 - j_2 + 1)!.$$

Since *factorials* are not defined for negative integers, only transitions respecting

$$j_2 + j_1 - 1 \geq 0 \;\rightarrow\; j_2 \geq 1 - j_1, \tag{2.60a}$$
$$j_2 - j_1 + 1 \geq 0 \;\rightarrow\; j_2 \geq j_1 - 1, \tag{2.60b}$$
$$j_1 - j_2 + 1 \geq 0 \;\rightarrow\; j_2 \leq 1 + j_1 \tag{2.60c}$$

can occur. This can be summarised in the **second optical transition selection rule**:

$$\boxed{|j_1 - 1| \leq j_2 \leq j_1 + 1.} \tag{2.61}$$

The **final optical transition selection rule** is not derived from equation (2.56), but rather from parity considerations about the spatial operator **r**. Since **r** is odd under parity transformations π, it cannot connect orbitals of the same parity. We have then that

$$\boxed{\pi_f = -\pi_i.} \tag{2.62}$$

This condition is connected to the wave-functions of charges in the valence and conduction band, and so, is material dependent. Let us now analyse how different valence bands can be connected to the conduction band. In Ge, at Γ point, the valence bands can be approximate to p-orbitals and the conduction band to s-orbitals. At conduction L point the orbitals are a mixture of p- and d-orbitals, but with a predominant odd parity profile. This does not mean, however, transitions from valence Γ to conduction L do not happen. Ge is, after all, an indirect band-gap semiconductor. Such transitions are, however, phonon assisted, in order for momentum and symmetry to be conserved. Nevertheless, in either case, the conduction band angular momentum is dictated by electronic spin. Let us consider direct transitions using the first selection rule:

Heavy-holes: $|j_1, m_1\rangle = \left|\frac{3}{2}, \pm\frac{3}{2}\right\rangle$, $m_2 = \pm\frac{1}{2}$

$$q = m_2 \mp \frac{3}{2} = \{\pm 1, \pm 2\}. \tag{2.63}$$

Notice the selection rule does not impose restrictions on q itself, but it is limited by the rank of the spherical tensor operator; in this case $k = 1 \rightarrow q = \{+1, 0, -1\}$. The physical transitions are then:

$$\left|m_1 = -\frac{3}{2}\right\rangle \rightarrow \sigma^+ \rightarrow \left|m_2 = -\frac{1}{2}\right\rangle \tag{2.64a}$$

$$\left|m_1 = +\frac{3}{2}\right\rangle \rightarrow \sigma^- \rightarrow \left|m_2 = +\frac{1}{2}\right\rangle \tag{2.64b}$$

Light-holes: $|j_1, m_1\rangle = \left|\frac{3}{2}, \pm\frac{1}{2}\right\rangle$, $m_2 = \pm\frac{1}{2}$

$$q = m_2 - \mp\frac{1}{2} = \{0, \pm 1\}. \tag{2.65}$$

We can see that transitions that preserve the sign of m are only possible for $q = 0$:

$$\left|m_1 = \pm\frac{1}{2}\right\rangle \rightarrow \sigma^0 \rightarrow \left|m_2 = \pm\frac{1}{2}\right\rangle . \tag{2.66}$$

On the other hand, circularly polarised light *flips* m:

$$\left|m_1 = -\frac{1}{2}\right\rangle \rightarrow \sigma^+ \rightarrow \left|m_2 = +\frac{1}{2}\right\rangle \tag{2.67a}$$

$$\left|m_1 = +\frac{1}{2}\right\rangle \rightarrow \sigma^- \rightarrow \left|m_2 = -\frac{1}{2}\right\rangle \tag{2.67b}$$

Split-orbit: $|j_1, m_1\rangle = \left|\frac{1}{2}, \pm\frac{1}{2}\right\rangle$, $m_2 = \pm\frac{1}{2}$

$$q = \pm\frac{1}{2} - m_2 = \{0, \pm 1\}. \tag{2.68}$$

Similarly as for the light-holes case we have that

$$\left|m_1 = \pm\frac{1}{2}\right\rangle \rightarrow \sigma^0 \rightarrow \left|m_2 = \pm\frac{1}{2}\right\rangle \tag{2.69a}$$

$$\left|m_1 = +\frac{1}{2}\right\rangle \rightarrow \sigma^+ \rightarrow \left|m_2 = -\frac{1}{2}\right\rangle \tag{2.69b}$$

$$\left|m_1 = -\frac{1}{2}\right\rangle \rightarrow \sigma^- \rightarrow \left|m_2 = +\frac{1}{2}\right\rangle \tag{2.69c}$$

It is important to notice that all of these transitions are allowed by the selection rule on j. The bounds of the second selection rule also allow transitions to states with, for example, $j = 5/2$ in some cases, but such states are not present in the conduction band at Γ point.

2.6 Ge quantum dots

Quantum dots are nanoscale quantum devices that confine charge carriers within small, well-defined regions of a semiconductor quantum well. This strong confinement discretizes the energy levels, giving rise to an artificial-atom-like spectrum. In gate-defined quantum dots, confinement is achieved electrostatically using metallic surface gates. By applying appropriate voltages, these gates change the potential landscape of the underlying quantum well. Applying negative voltages locally, for example, depletes the electron gas beneath the gates, allowing the creation of isolated charge carrier islands through careful gate design and tuning[3].

Typically, quantum dot architectures employ several types of gates. **Plunger gates** tune the chemical potential inside the dot, effectively controlling its charge occupancy. **Barrier gates** define tunnel barriers, regulating coupling between quantum dots and source/drain reservoirs or between multiple dots. **Lead gates** provide connections to external charge reservoirs. Additionally, **screening gates** can help stabilize and shape the overall potential landscape. This confinement potential can, near its minimum, be approximated by an anisotropic two-dimensional harmonic potential:

$$V(x,y) = \frac{1}{2}m^*\omega^2(\delta x^2 + \frac{y^2}{\delta}), \tag{2.70}$$

where m^* is the effective mass, and $\delta = \omega_x/\omega_y$ is the ratio of the confinement strength (frequency) in each direction. This is a good approximation for finite quantum systems of fermions with no unresolved degeneracies at the Fermi surface. In other words, this is valid for a certain number of fermions in the quantum dot for which a large energy is required for the addition of an extra fermion. Under this assumption the fermions are considered to move independently. The energy spectrum of this system is given by

$$\varepsilon_{n_x,n_y}(\delta) = \hbar\omega\left[\left(n_x + \frac{1}{2}\right)\sqrt{\delta} + \left(n_y + \frac{1}{2}\right)/\sqrt{\delta}\right]. \tag{2.71}$$

Alternatively, in the case of a perfectly symmetric dot, we can take advantage of the quantum dot's circular symmetry and use polar coordinates to write the energy spectrum as

$$\varepsilon_{n,m} = \hbar\omega(2n + |l| + 1), \tag{2.72}$$

with $n = 0, 1, 2, ...$ (radial quantum number) and $l = 0, \pm1, \pm2, ...$ (angular momentum quantum number).

When a charge is added to the quantum dot it occupies the lowest possible energy state available. Electrostatic repulsion prevents a second charge from entering the dot unless it is supplied with sufficient energy. This phenomenon is called *Coulomb blockade* and results in the characteristic Coulomb diamond features in transport

[3]This section's discussion on the fundamentals of quantum dots is based on references [56, 109–111]

measurements. In the *Constant-interaction model*, which assumes the Coulomb interaction between charges does not depend on the number N of charges, the charging energy, that is, electrostatic energy cost to add an additional charge to the dot is given by

$$E_C = \frac{e^2}{2C}, \tag{2.73}$$

where C is the total capacitance of the dot. By manipulating the gate voltage above the dot, its energy can be controlled and occupancy changed. For N charges, the quantum dot total energy is

$$E(N) = \frac{\left[e(N - N_0) - C_g V_g\right]^2}{2C} + \sum_N \varepsilon_{n,l}, \tag{2.74}$$

where N_0 represents the background (neutralizing) charge, or the effective offset charge in the quantum dot, C_g is the capacitance between the quantum dot and the gate and V_g is the gate voltage. The last term is a sum over all the occupied states given by equation (2.72). The dependency of quantum dots on the gate voltage V_g makes their sensitiveness to electric field fluctuations (due, for example, to nearby charge traps) clear.

A single quantum dot is directly connected to the source and drain leads. Charging or depleting the dot involves tunneling charges from source to dot and from dot to drain, respectively. This is modelled by the tunneling Hamiltonian $\mathcal{H}_t$:

$$\mathcal{H}_t = \sum_{r=S,D} \sum_{k,n,\sigma} T^r_{kn}\, a^\dagger_{n,\sigma r}\, a_{l,\sigma\text{dot}} + \text{h.c.}, \tag{2.75}$$

where r is the lead index (S for source and D from drain), k is the lead single-particle energy, n is the dot energy label, and σ is the spin label. T^r_{kn} are tunneling amplitudes, $a^\dagger_{n,\sigma r}$ is the creation operator at the leads and $a_{l,\sigma\text{dot}}$ the annihilation operator in the dot. The creation operator in the dot and annihilation operator in the leads are taken into account by the Hermitian conjugate term. The tunneling matrix elements are given by Fermi's golden rule:

$$\Gamma_r(E) = \frac{\hbar}{2\pi} \sum_k |T^r_{kn}|^2 \delta(E - \epsilon_{kr}) = \frac{\hbar}{2\pi} |T^r|^2 \rho_r(E), \tag{2.76}$$

where

$$\rho_r(E) = \sum_k \delta(E - \epsilon_{kr}), \tag{2.77}$$

is the lead density of states (DOS). Explicitly, the tunneling amplitudes are give by

$$T^r_{kn} = \int d\mathbf{r}\, \psi^*_{k,r}(\mathbf{r})\, V_T(\mathbf{r})\, \psi_{n,\text{dot}}(\mathbf{r}), \tag{2.78}$$

where V_T describes the barrier potential connecting the states $\psi^*_{k,r}(\mathbf{r})$ in the leads and $\psi_{n,\text{dot}}(\mathbf{r})$ in the dot. When charges tunnel through the quantum dot, from one

lead to another, a conductance can be calculated for the quantum dot:

$$G_{rr'}(\mu) = -2e^2 \frac{\Gamma \Gamma_r \Gamma_{r'}}{\Gamma} \frac{1}{1 + f(\Delta - \mu)} f'(\Delta - \mu), \tag{2.79}$$

where

$$\Gamma = \Gamma_S + \Gamma_D, \tag{2.80}$$

$f(\Delta - \mu)$ is the Fermi-Dirac distribution, Δ is the energy change in the dot when another particle is added to it, and μ is the dot's chemical potential.

In 2018, the first gate-defined Ge quantum dot was realised by Nico Hendrickx and his team [112]. Their device employed a shallow Ge well between SiGe layers, with superconducting Aluminium leads. The team demonstrated Coulomb blockade and gate-tunability of the quantum dot, establishing it as a promising qubit platform. In 2020, Hendrickx's team realised a single-hole spin qubit in a quadruple quantum dot, with single-shot readout and coherent Rabi control of the confined hole [113]. A long spin relaxation time of over 1 ms was measured and universal single-qubit operations demonstrated. In the same year, fast two-qubit logic was established in this system [114]. Via strong spin-orbit coupling, a Rabi frequency $>$ 100MHz was achieved, with single-qubit gates achieving 99.3% fidelity. These results showed that Ge qubits can satisfy the *DiVincenzo criteria*[4] with ultrafast, high-fidelity operations.

In 2021, Zhanning Wang and collaborators developed a theory of optimal operation points for Ge hole spin qubits [115]. By analysing electric field tunability and spin-orbit effects, they identified "sweet spots" where fast electric dipole spin resonance coincides with vanishing dephasing from charge noise. This work predicts that Ge hole qubits can simultaneously achieve high driving speeds and long coherence time, overturning the speed–decoherence trade-off.

In the same year, Daniel Jirovec and collaborators demonstrated a low field (10 mT) hole singlet–triplet qubit in a planar Ge double dot by exploiting large out-of-plane g-factors in the system [116]. A two-axis control was achieved: rotation by exchange energy manipulation (the energy difference between singlet and triplet states) and by the g-factor difference. Gate-driven rotations with frequencies $>$100 MHz were achieved with dephasing times of ~ 1 μs. This showed Ge qubits with coherence times comparable to GaAs/Si qubits, but operated at much lower magnetic fields.

Also in 2021, Hendrickx's team built a 2$\times$2 array of Ge hole spin qubits, fully coupled and controllable [117]. Four gate-controlled quantum dots were defined in a planar device, coupled to neighbours via gate voltages, and implemented in one-,

[4]The DiVincenzo criteria are experimental conditions required for quantum computation and communication establishement, according to David P. DiVincenzo. They are: **1** The physical system must be scalable, with well defined qubits. **2** The system must allow the initialisation of qubits to a fiducial state. **3** Quantum coherence times must be sufficiently long. **4** It must employ a universal set of quantum gates. **5** It must be able to realise qubit-specific measurements. **6** It must be able to convert between stationary and flying qubits. **7** It must transmit flying qubits between specific locations faithfully.

two-, three-, and four-qubit gate sequences. Dynamical decoupling was employed to preserve coherence. This is the first demonstration of a small Ge quantum processor, showing all-electrical multi-qubit operations.

In 2021, Stefano Bosco and collaborators proposed a new quantum dot design based on asymmetric potentials that strongly squeeze the quantum dot in one direction, improving electric control via spin-orbit coupling [118]. Their design allows for low-power ultra-fast operations in the GHz range by dramatically enhancing Rashba spin-orbit coupling in heavy-hole qubits. The design relies on device geometry rather than strain, suggesting a path to ultrafast hole qubit gates in standard Ge heterostructures.

In 2022, Ke Wang's team achieved ultra-fast coherent control of a hole spin in a Ge nanowire double dot (hut wire) [119]. The strong spin-orbit coupling in Ge enabled record Rabi oscillation frequencies ($>$540 MHz at $B = 100$ mT) with heavy-hole spins, corresponding to a spin-orbit length of only ~ 1.5 nm. This work solidified the potential of Ge hole spins for very high-speed control, satisfying the fast gate criterion.

In the same year, He Liu and his team achieved gate-tunable spin–orbit coupling in a Ge hut-wire double dot [120]. By electrically adjusting interdot tunneling, the effective spin-orbit was controlled. Spin-blockade leakage measurements showed that the spin-orbit length could be tuned from ~ 2 nm up to ~ 49 nm. This tunability implies that Ge qubits' electric dipole spin resonance strength can be electrically controlled.

In 2023, Abhikbrata Sarkar and collaborators presented a theory of planar Ge hole spin qubits with an in-plane magnetic field [121]. Analysing realistic quantum dot confinements, they found highly anisotropic Rabi frequencies: Electron Dipole Spin Resonance (EDSR) is maximal when the driving electric field is parallel to the magnetic field B, and weaker for a perpendicular field. In-plane g-factors are also shown to be strongly anisotropic for *squeezed* dots. Crucially, they show there is no field orientation that completely nullifies dephasing, due to orbital spin-orbit effects. The paper provides design rules (field orientation, quantum dot size) for optimized Ge qubit operation.

In the same year Hanifa Tidjani and collaborators departed from planar Ge quantum dots and proposed vertical stacks of strained Ge quantum wells double quantum dot realisation [122]. Their system consists of vertically stacked quantum dots separated by barriers; each barrier containing one quantum dot, with both coupled to reservoirs. Transport was measured through each dot in parallel, confirming its well-controlled behaviour. This device architecture enables vertically coupled qubits or multi-layer qubit designs.

Also in 2023, Patrick Del Vecchio and Oussama Moutanabbir proposed a "light-hole" gate-defined spin qubit in highly tensile-strained Ge quantum wells [123]. The theory shows that squeezing the dot (low-dimensional confinement) can produce light-hole states with spin-orbit dipole moments 100–1000$\times$ larger than heavy holes, yielding ultrafast electrical control. They calculate that such light-hole qubits could enable GHz gates (via strong combined Rashba effects) at low power, offering a

new all-Ge hybrid qubit platform.

In the same year, Chien-An Wang's team developed quantum simulations with a Ge hole-qubit array [124]. The team used a linear array of four gate-defined Ge QDs (four holes) to simulate resonating-valence-bond physics. They coherently initialized singlet-product states and observed coherent oscillations between different multi-spin states. By pulsing exchange couplings, they produced four-spin "s-wave" and "d-wave" singlet states. The hole spins remained coherent over many oscillation periods, demonstrating control of multi-qubit entangled states in Ge

In 2024, Arianna Nigro and collaborators achieved the integration of coplanar-waveguide resonators with Ge/SiGe heterostructures [125]. They were able to fabricate high-quality superconducting resonators and gate-defined double quantum dots on the same reverse-graded Ge/SiGe wafer. The charge stability of the quantum dots coupled to the resonator was measured and determined to be well-controlled. This work shows the compatibility of planar Ge qubit devices with Quantum Electro-Dynamics (QED) circuit, opening paths to long-range coupling and readout of Ge spin qubits.

In the same year, Floor van Riggelen-Doelman and her team demonstrated spin-qubit shuttling in a linear array of Ge quantum dots [126]. The team moved a hole spin-qubit through multiple tunnel-coupled Ge quantum dots while preserving coherence. Spin basis states were shuttled over effective lengths >300 μm, and superposition states over 9 μm (extendable to 49 μm via dynamical coupling). This demonstrates the feasibility of moving hole qubits with strong Spin-Orbit Interaction in Ge, enabling routing of qubits between registers.

In 2024, Hendrickx's team demonstrated the "sweet-spot" operation of a Ge hole spin-qubit [127]. They studied a single-qubit's in-plane g-tensor, revealing extreme anisotropy and how electrical control affects it. Operating at the symmetry point (zero first-order Zeeman dependence), they achieved coherence times $\approx 17.6, \mu$s, which is limited by $1/f$ noise, and demonstrated single-qubit gate fidelity $>99\%$ even at relatively high temperatures of $T = 1$ K. This work uncovers anisotropic noise sensitivity in Ge and identifies qubit working points for long coherence.

In 2024 Yuan Kang and collaborators coupled a QED-circuit to a Ge hole double quantum dot. The qubit pair was coupled to a superconducting microwave cavity and and the hole-photon interaction measured. Using a calibrated virtual-gate method, they fitted the charge stability and extracted a hole-cavity coupling rate of $g/2\pi = 21.7$ MHz. This is the first demonstrated integration of a Ge double quantum dot with QED-circuit, paving the way for long-range qubit coupling and readout of Ge spin qubits.

In 2024, Lazar Lakic and collaborators presented a superconducting lead-quantum dot-superconducting lead junction in Ge/SiGe [128]. The superconducting leads were made of a PtSiGe alloy. The Sc-QD-Sc Josephson junction strongly coupled the dot to the two superconductors. By electrostratic gating, they were able to tune the ratio of the charging energy E_C to the induced gap, observing parity switches (even-odd ground-state transitions) and Yu-Shiba-Rusinov bound states. A relevant study for hybrid qubits systems.

Finally, in 2025, John Rooney's team demonstrated the gate-voltage tuning of a hole singlet-triplet qubit frequency in Ge [129]. They observed that small changes in the interdot barrier voltage can change the qubit resonance by an order of magnitude. The effect is attributed to the position-dependent variation of the quantum well strain, which can alter the hole's g-factor. The variation in strain is believed to yield a heavy-hole-light-hole bands mixing. The result highlights the highly tunnable nature of g-tensors and frequency by electrostatic gates in Ge double quantum dots.

Such remarkable contributions collectively establish Ge quantum dots as a versatile and promising solid-state qubit platform. They have strong and electrically tunable spin-orbit coupling, large and anisotropic g-factors, and can display high-fidelity control; important features for coherent spin manipulation. These properties are also promising for Ge hole quantum dots as a platform for photo-spin conversion: the large spin-orbit interaction facilitates spin generation via optical transitions, enabling direct interfacing with photons for spin initialisation, manipulation, and readout. These capabilities open a path for hybrid quantum architectures, where stationary Ge spin-qubits can be coherently linked via photonic channels, satisfying the demanding DiVincenzo criteria for quantum communication and distributed quantum computing. Ge quantum dots are an important tool to bridge solid-state quantum processors with photonic networks.

Despite these promising features, several significant challenges remain before Ge quantum dots can realise their full potential in scalable quantum technologies. There are, for example, fabrication complexities, such low fabrication yielding and achieving uniform and precisely controlled quantum dot geometries, strain profiles, and barrier heights. High-quality heterostructures with precise interface smoothness and minimal disorder are important to ensure reproducible devices, but understanding how surface roughness, traps, and non-uniform strain affect performance is also important. Another challenge is engineering robust coupling to photonic structures for efficient photo-spin conversion. Thermal management and operation at higher temperatures, though recently improved, still require careful optimisation. Addressing these issues is crucial in bridging laboratory demonstrations into reliable building blocks of real networks.

2.7 Outline of this thesis

We have so far introduced fundamental concepts of classical and quantum information processing and transmission. We have also, briefly outlined various qubit candidates and discussed the challenges quantum networks must overcome. In particular, we introduced the concept of quantum repeaters and the Vrijen–Yablonovitch protocol for photo-spin conversion. We have also discussed the advantages and disadvantages of different material choices for photon-spin conversion platforms, presenting Ge as a strong candidate. We discussed valence band degeneracies and described how confinement effects, achieved through quantum well engineering, can lift these degeneracies. We also derived the optical transition selection rules.

Finally, we described recent achievements in Ge/SiGe heterostructure quantum well devices, notably quantum dots.

While these discussions present Ge as an interesting platform for photo-spin conversion, still, a few issues must be addressed, which is the goal of the present work. For one, while a few groups have successfully developed Ge-based devices, still many groups struggle with reproducibility and device yield due to gate leakages caused by interfacial trap states and defects and to high ohmic contact resistances due to poor diffusion conditions. So, optimising fabrication recipes is a crucial step in developing reliable and reproducible devices. With this goal in mind, in Chapter 3, we discuss fabrication methods and the specific challenges associated with Ge-based systems. We present different surface cleaning protocols and evaluate their performance via X-ray photo-electron spectroscopy (XPS) and Atomic Force Microscopy (AFM) analysis.

Besides recipe optimisation, a second issue is relevant for employing Ge devices as photo-spin platforms. The original proposal for the Vrijen-Yablonovitch protocol considered GaAs as a platform. GaAs presents, however, a phenomenon which makes its employment in photon-spin conversion devices less stable: persistent photo-conductivity, [130, 131]. Persistent photo-conductivity in GaAs quantum wells is verified when photons with energy above the bandgap energy generates electron-hole pairs, which are preserved, to some extent, after illumination is stopped. Verifying the stability of transport properties of Ge quantum wells with light irradiation is then an important task, as the presence of such phenomenon must be ruled-out if Ge-devices are to proceed as photo-spin interfaces. Chapter 4 focuses then on transport characterisation with light irradiation, discussing charge carrier concentration increment factors, in-dark relaxation and possible mechanisms for the measured photo-conductivity. Finally, in Chapter 5, we summarise our conclusions on the viability of Ge/SiGe quantum well heterostructures as a platform for photo-spin conversion technologies.

3

Germanium devices fabrication

Ge was at the inception of solid-state electronics. It was, however, quickly replaced in the industry by Si, due to its natural abundance and the higher quality of its native oxide. On the other hand, on the purely scientific end of research, GaAs became a go-to platform for proof of concepts and basic solid-state physics' phenomena investigation due to the high quality of GaAs/AlGaAs heterostructures, which can be made flat with atomic precision via advanced techniques in Molecular Beam Epitaxy, allowing for minimal impurity scattering. This creates ultra-clean 2D electron gases (2DEG), which are essential for quantum transport measurements, for example. Many canonical devices and phenomena have been demonstrated first in GaAs-based samples, such as the quantum Hall effect, measured in 1980 by Klaus von Klitzing [132], the fractional quantum Hall effect, measured in 1982 by D. C. Tsui's team [133], the first measurement of Coulomb blockade phenomenon by T. A. Fulton and G. J. Dolan in 1987 [134], and the first quantum point contact in 1988, devised by David A. Wharam's team in the Netherlands [135] and, independently, by Bart J. van Wees' team in Germany [136].

In the last decades, however, Ge has re-emerged as a topic of interest, in particular due to its potential in computation and telecommunication industries. Ge's band-gap lies inside the *telecomm* waveband, and its compatibility with Si makes its integration with the existing infrastructure natural. This renewed interest has also motivated investigations on micro-fabrication techniques, as the similarities with Si are not enough to warrant a simple transfer of methods from one material to the other. In this chapter we will discuss the fabrication recipes tested and the corresponding challenges faced, with particular focus to etching and cleaning effects on surface composition and roughness, as clean, smooth surfaces are essential for ohmic metals diffusion.

The samples discussed in this work were provided by Professor Kentarou Sawano, from Tokyo City University, and by Delft. Tokyo City University's samples are grown by Molecular Beam Epitaxy and are labelled **Sample A** and **Sample B**. **Sample A** is nominally undoped, but has some unintentional p-type contamination which makes it conductive even with no gate voltage applied. **Sample B**, on the other hand, has a B-doped layer bellow the quantum well. These heterostructures' profiles can be seen in Figure 3.1.

Delft's sample was grown by Chemical Vapour Deposition and is nominally undoped. It is labelled **Sample C** and its profile can be seen in Figure 3.2.

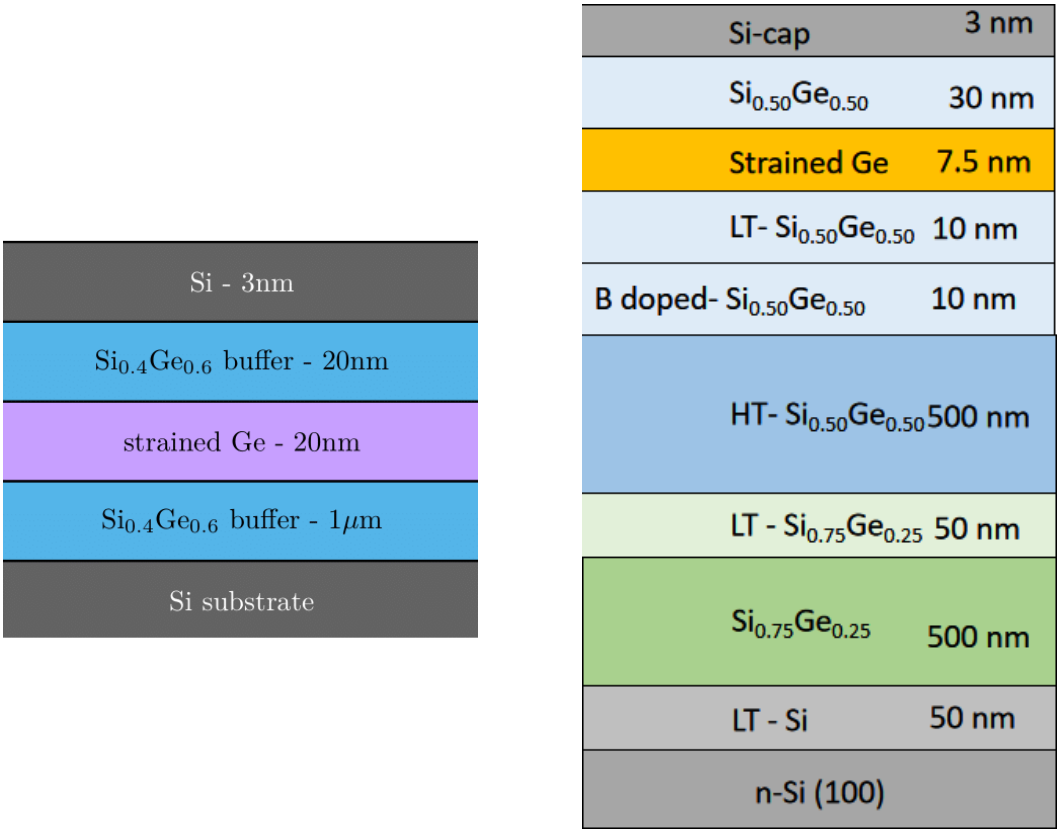

(a) **Sample A**: Undoped sample. (b) **sample B**: Doped sample.

FIGURE 3.1: **Molecular Beam Epitaxy grown Ge/SiGe heterostructures**: The samples were provided by professor Kentarou Sawano from Tokyo City University. **Sample A** is nominally undoped, but unintentional p-type contamination makes it conductive even at 0V top gate voltages.

3.1 Device design

The devices fabricated for this study were conventional 6-terminals Hall bars (with the addition of the contacts connected to top gates). The overall design consists of a mesa structure on top of which the conduction channel is defined by top gates. These gates are separated from the sample by an Aluminium oxide (Al_2O_3) insulating layer. The electrical contact with the channel is established via Al ohmic contacts, which were connected to contact pads linking them to the wiring pads. Such pads were made of a thin layer of Ti (10nm) followed by a thick layer of Au (200nm). The Hall bar design can be seen in Figure 3.3.

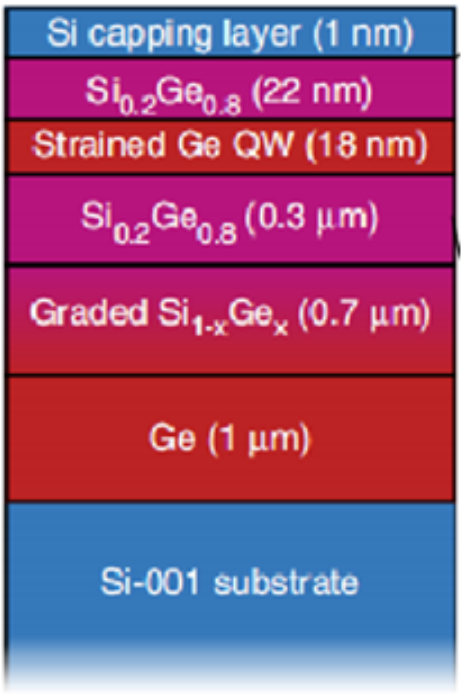

FIGURE 3.2: **Chemical Vapour Deposition grown Ge/SiGe heterostructures**: **Sample C** - undoped sample provided by Delft [112].

3.2 Standard fabrication

In this section we will detail the standard steps for Hall bars fabrication, many of which are shared with different types of devices fabrication such as quantum dots.

Standard cleaning:
The standard cleaning of the sample is done by Acetone (CH_3COCH_3) dip and sonication, with the process being repeated once with a clean beaker and fresh Acetone, followed by Isopropyl alcohol (C_3H_8O) dip and sonication. This process is carried out in-between fabrication steps and before storing the sample.

Acetone is a powerful solvent for organic materials, but it has a relatively low boiling point, $\sim$56°C. Its vapour pressure at room temperature is, however, relatively high, $\sim$30.6 kPa, which accounts for its fast evaporation in normal laboratory conditions. Isopropyl alcohol (IPA), on the other hand, is less aggressive than Acetone, but has a higher boiling point, $\sim$82.6°C, and a lower vapour pressure, $\sim$4.4 kPa. It cleans light organic residues and displaces water and Acetone molecules, allowing the sample to dry cleanly. IPA is used as a final cleaner because the quick evaporation of Acetone may leave patches of contaminant solutes behind, which can be observed in samples as blackish spots. After this last dipping step, the sample is blown dry by

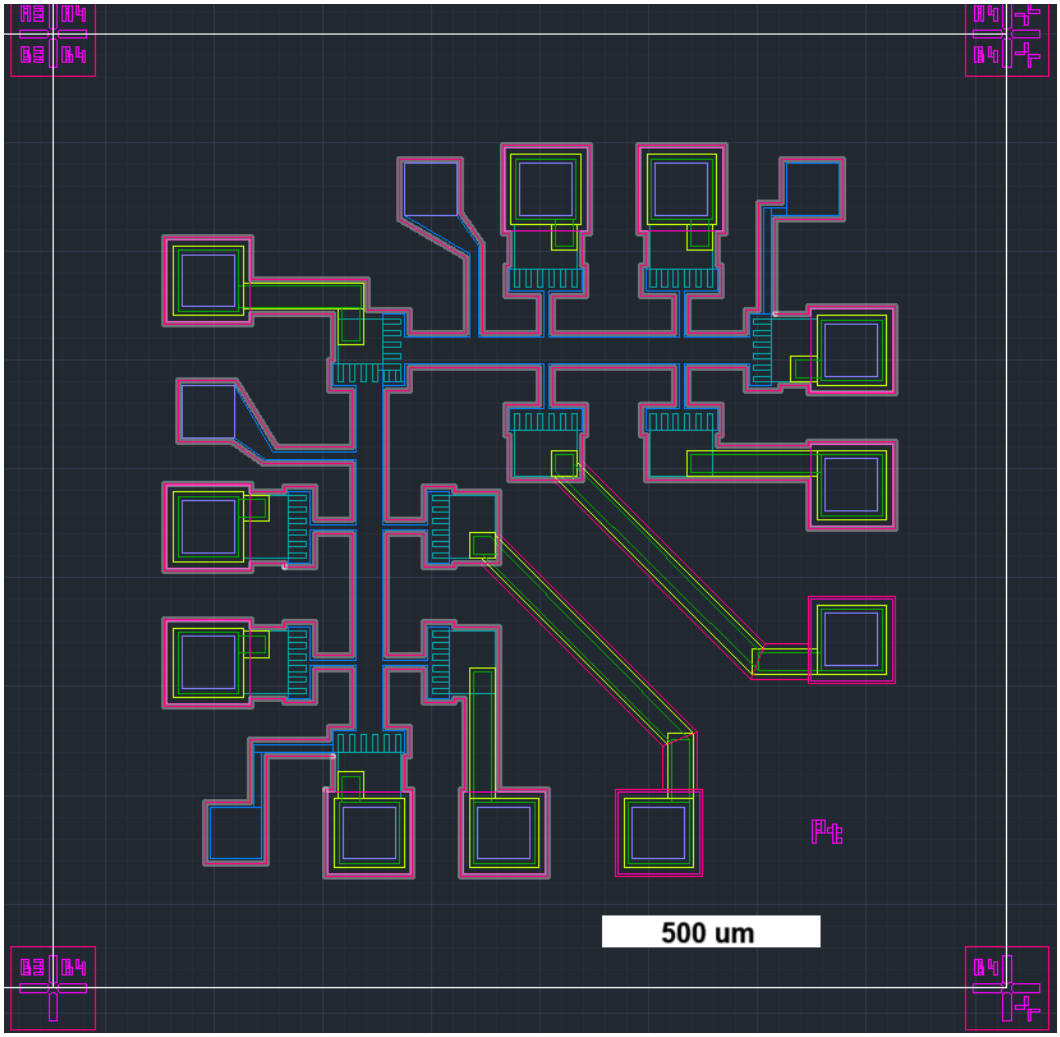

FIGURE 3.3: **Hall bar design:** This design consists of two 6-terminals hall bars fabricated on perpendicular directions, sharing one source/drain terminal. The effective channel length is 300 nm, and the effective width is 60 nm.

a N_2 gun and finally baked in a hot plate at 110°C for 3 minutes.

1. Position markers:
Accurate alignment of lithographic layers requires position markers, which are metallic reference points deposited near the active regions of the sample. The process begins by coating the sample in a positive photoresist; a photosensitive polymer that has its chemical structure altered when irradiated by light of appropriate wavelengths. The resist used was an LOR/S1813 bilayer resist. LOR is solidified by baking the sample at 180°C for 5 minutes. The S1813 layer is baked at 110°C for 3 minutes. A digital mask is used to expose pre-selected areas in an LED-lithography machine. Such areas become then soluble in TMAH-based aqueous developers. They are removed by dipping the sample for 2 minutes in MF CD-26 followed by a 2 minutes

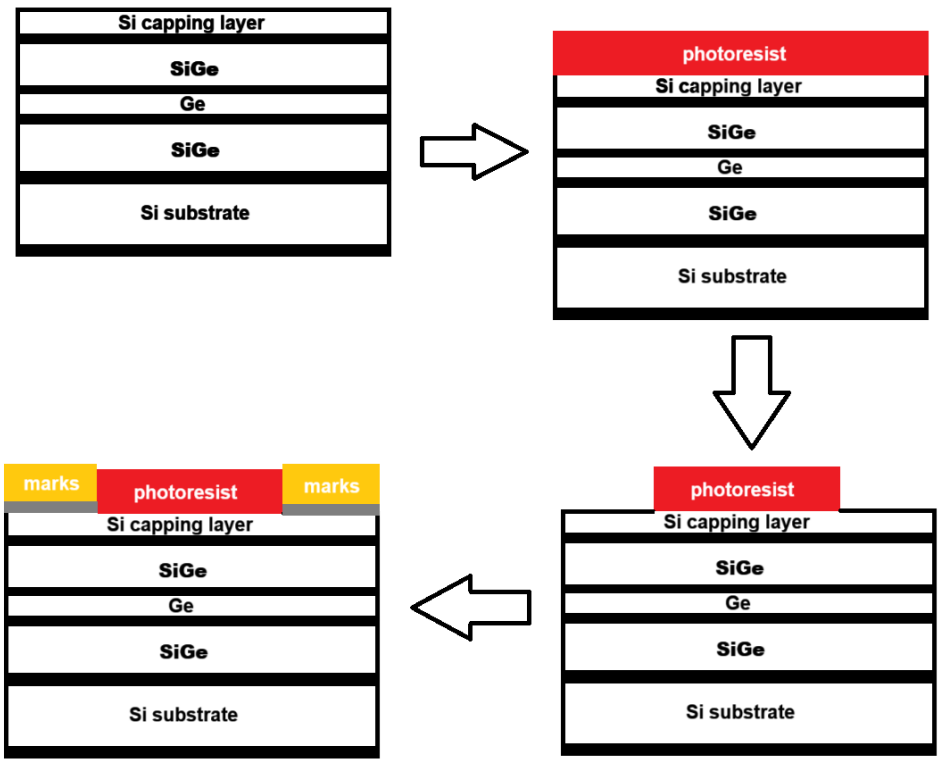

FIGURE 3.4: **Position markers deposition process:** A photoresist coating polymer is applied on top of the sample. The polymer becomes soluble in TMAH-based developer when exposed to light of appropriate wavelengths. The exposed areas are removed and metal markers are deposited by electron-beam evaporation of Ti (10nm) followed by Au (200nm).

dip in de-ionised water (DIW), see Figure 3.4. This procedure is repeated for every subsequent lithographic layer.

The sample is then placed in an electron-beam evaporator, where a thin adhesion layer of Ti (10 nm) is deposited, followed by a thicker Au layer (200 nm). Ti ensures a stronger adhesion between the Au and the underlying semiconductor surface, as Au alone has poor adherence to oxides. After the evaporation is complete, a lift-off process is performed in Acetone (at 110°C for 60 minutes), removing the remaining resist and excess metal, leaving only the aligned position marks, see Figure 3.5. All metal deposition steps follow this procedure.

2. Mesa etching:

Since several devices are fabricated on the same chip, it is important to cut communication channels between devices. This means isolating the quantum well regions belonging to each device by etching mesas: small elevated regions where the gates

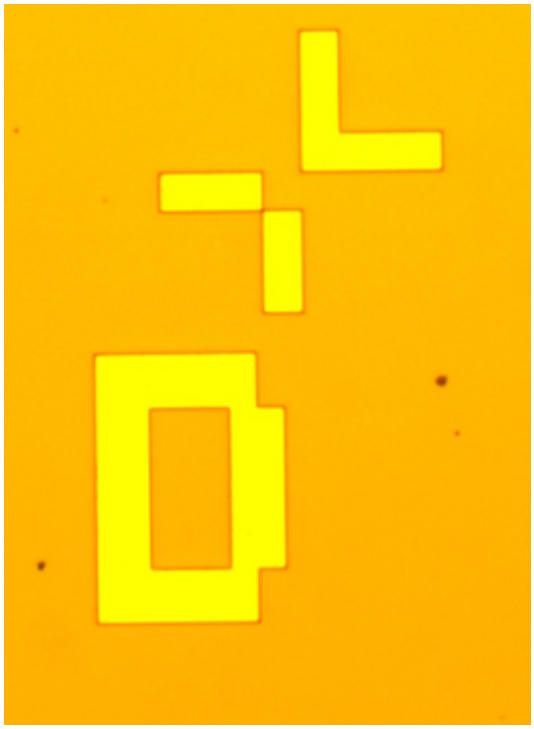

FIGURE 3.5: **Finished position marker:** A Ti (10nm) - Au (200nm) bilayer position marker for lithographic layers alignment.

are placed. Mesas can be etched either by *Reactive Ion Etching* (RIE) or by chemical etching. RIE is done in a plasma chamber with the following conditions:

$SF_6/CHF_3/O_2$ 35/10/19 cc/min atmosphere
Power = 60W
Frequency = 13.6MHz
Pressure = 1.5 Pa

In this process, the active etching component is the SF_6 gas. An oscillatory radio frequency electric field is applied between the electrodes of the chamber, ionising the gas into a plasma. When the plasma is formed the following reaction happens:

$$SF_6 \longrightarrow SF_x + (6 - x)\,F + e^{-}. \tag{3.1}$$

Cations are then accelerated towards the sample surface causing two kinds of effects: some atoms are physically sputtered from the surface by ionic bombardment, while others have their reactivity enhanced. While the SF_x fragments remain mostly inert, fluorine radicals react with the SiO_2 capping layer molecules according to

$$SiO_2\,(s) + 4\,F \rightarrow SiF_4\,(g) + O_2\,(g), \tag{3.2}$$

exposing the SiGe alloy layer underneath it. Once exposed, the Si and Ge atoms are combined with the fluorine radicals via the following reactions

$$\mathrm{Si} + 4\mathrm{F} \rightarrow \mathrm{SiF_4\ (g)} \tag{3.3}$$
$$\mathrm{Ge} + 4\mathrm{F} \rightarrow \mathrm{GeF_4\ (g)}. \tag{3.4}$$

The gaseous phases are then pumped out of the system.

The chemical etching is performed with a *buffered oxidising* etchant solution of Acetic acid (CH_3COOH), Hydrogen peroxide (H_2O_2), and Hydrofluoric acid (HF):

$$\mathrm{CH_3COOH : H_2O_2 : HF} = 3 : 2 : 1. \tag{3.5}$$

The chemical reaction happens according to the following steps:

Step 1: Etching of native SiO_2 by hydrofluoric acid (HF):

$$\mathrm{SiO_2\,(s)} + 6\,\mathrm{HF\,(aq)} \rightarrow \mathrm{H_2SiF_6\,(aq)} + 2\,\mathrm{H_2O\,(l)} \tag{3.6}$$

Step 2: Oxidation of elemental Si and Ge by hydrogen peroxide:

$$\mathrm{Si\ (s)} + \mathrm{H_2O_2}\,(aq) \rightarrow \mathrm{SiO_2}\,(s) + \mathrm{H_2O}\,(l) \tag{3.7a}$$
$$\mathrm{Ge\ (s)} + \mathrm{H_2O_2}\,(aq) \rightarrow \mathrm{GeO_2}\,(s) + \mathrm{H_2O}\,(l) \tag{3.7b}$$

Step 3: Dissolution of the oxides by HF:

$$\mathrm{GeO_2}\,(s) + 4\,\mathrm{HF} \rightarrow \mathrm{GeF_4}\,(aq) + 2\,\mathrm{H_2O} \tag{3.8a}$$
$$\mathrm{GeF_4}\,(aq) + x\,\mathrm{H_2O} \rightarrow [\mathrm{GeF_4(H_2O)}_x]\,(aq) \tag{3.8b}$$

$$\mathrm{SiO_2}\,(s) + 6\,\mathrm{HF} \rightarrow \mathrm{H_2SiF_6}\,(aq) + 2\,\mathrm{H_2O} \tag{3.9a}$$
$$\mathrm{H_2SiF_6}\,(aq) \rightarrow \mathrm{SiF_6^{2-}}\,(aq) + 2\,\mathrm{H^+} \tag{3.9b}$$

GeO_2 is a water-soluble oxide that forms readily at laboratory conditions. It is also more soluble in HF, increasing its etching rate. By comparison, the Si-based reactions have higher activation energies and more stable native oxides, further slowing the Si etching rate and making the solution highly Ge-selective. In both of these processes the Acetic acid serves as a diluent, buffering and moderating the total etching rate and stabilising the Hydrogen peroxide, improving reaction uniformity.

Figure 3.7 shows the comparison of etched depth as a function of time for both methods. From Figure 3.7.a we can see the RIE process is faster and attacks Si and Ge at a similar rate. From Figure 3.7.b, however, we notice the chemical etching is selective towards Ge. The angle of the mesa walls is also a function of time and varies with the method, see Figure 3.8. Chemical etching, in particular, was shown

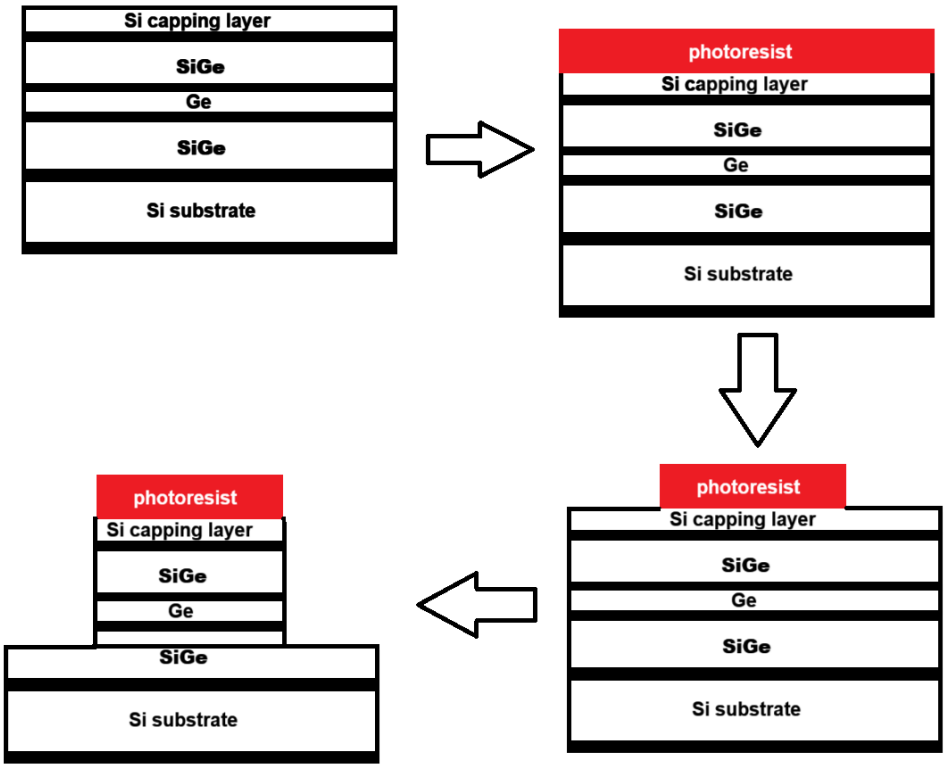

FIGURE 3.6: **Etching process:** The sample is covered by a photoresist polymer, selected areas are exposed to light in an LED-lithography machine and dissolved by an aqueous developer solution. After that, chemical or RIE etching is performed until the mesa is etched below the quantum well.

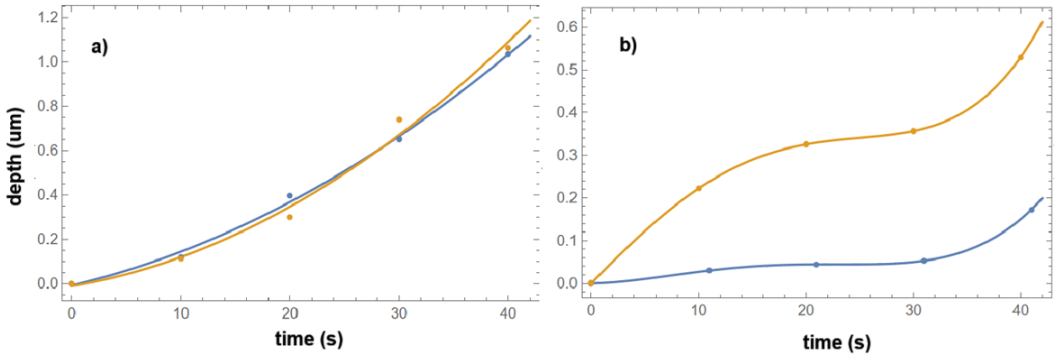

FIGURE 3.7: **Rate comparison between RIE and chemical etching:** Etched depth as a function of time for **a)** Reactive Ion Etching and **b)** chemical etching. The blue curves correspond to bulk Si while the yellow curves correspond to the undoped Ge/SiGe heterostructure.

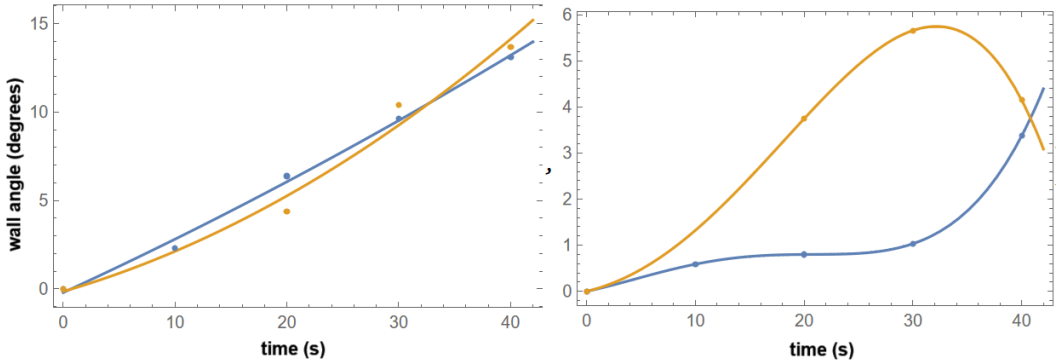

FIGURE 3.8: **Etched wall angle comparison between RIE and chemical etching:** Etched mesa walls angle as a function of time for **a)** Reactive Ion Etching and **b)** chemical etching. The blue curves correspond to bulk Si. The yellow curves correspond to the undoped Ge/SiGe heterostructure.

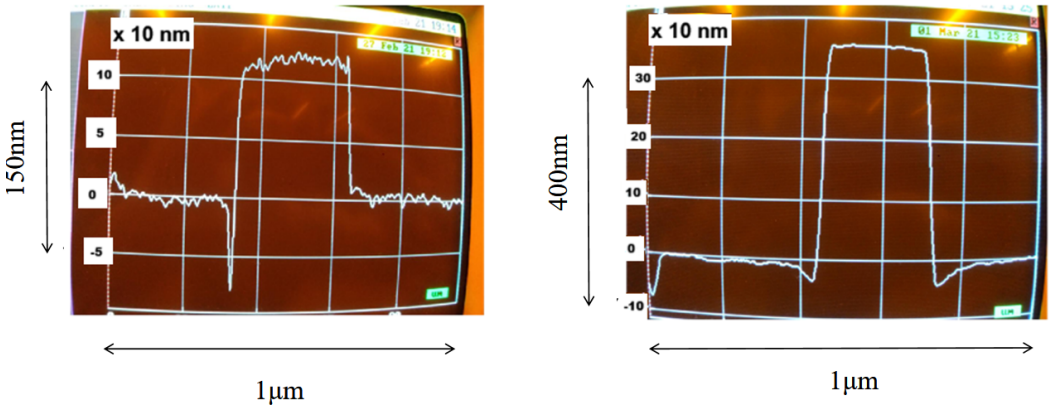

FIGURE 3.9: **Chemical etching trenching:** Profilometer images of chemically etched samples showing trenching effect: an over-etching of random areas, typically surrounding the mesa walls.

to be prone to *trenching*, that is, the over-etching of random regions, typically around the walls, see Figure 3.9.

3. Ohmic contacts

Ohmic contacts were fabricated by depositing Al via electron-beam evaporation. The ohmic contacts connect to the quantum well from the top via annealing-induced diffusion. Diffusion does not happen, however, through oxides unless temperatures much higher than the allowed thermal budget are reached. Such oxides, as well as organic contaminants, must then be removed. The SiO_2 is chemically removed with a 1:10 HF:H_2O acid solution. The sample is dipped in this solution for 2 minutes and then rinsed in de-ionised water. After that, the sample must be quickly moved into the electron-beam evaporator chamber, which has to be promptly evacuated. This is due to the fact the native oxides on the SiGe layer start to regrow immediately.

The samples are then annealed at 300°C for 90 minutes. The process is carried out in forming gas atmosphere (H_2 + N_2).

4. Dielectric layer deposition

For top-gated devices, after the ohmic contacts, an insulating Al_2O_3 layer (30nm) is deposited via Atomic Layer Deposition (ALD). The ALD is done at 300°C and so, this step can be used as the annealing step for Al as well.

5. Top gate deposition

Finally, for top-gated devices, a thin gate is deposited, consisting of a 5 nm Ti layer, followed by a 15 nm Pd layer.

3.2.1 Recipe summary

Lithographic layers:
resist:LOR/S1813
Developer: MF CD-26 for 2 minutes, de-ionised water 2 minutes

1. **Position markers**
Material: Ti/Au 20/200 nm

2. **Mesa etching**
a.1. RIE: SF_6, 60W, 13.6MHz
a.2. chemical etching: $CH_3COOH : H_2O_2 : HF = 3 : 2 : 1$

3. **Ohmic contacts**
a. SiO_2 removal: HF:H_2O 1:10 2 minutes
b. Materials: Al 30 nm
c. Anneal: 300°C for 90 minutes in forming gas

4. **ALD insulation layer**
a. Dielectric: Al_2O_3, 30 nm

6. **Window etching for bonding pads**
a. Transene D 50°C, 5 minutes and 30 seconds

7. **Bonding pads**
a. Material: Ti/Au 20/200 nm

3.3 Compositional and surface morphology analysis for different etching and cleaning recipes

The fabrication steps described in the previous section configure the standard recipe used to fabricate Hall bars, based on the literature. The device yield following such steps was, however, notably low, mostly due to excessive gate leakage currents and high-resistance ohmic contacts. A few potential causes were considered. For gate leakage, the first possible issue is wafer contamination by environmental particulates, which can create leakage paths. Alternatively, mechanical stress from wire bonding may damage delicate structures such as thin insulators, as we have observed samples from the same batch displaying leakage currents after wire bonding, but not after dye bonding. In more recent recipes, thick Si_2N_4 pads were added under the bonding pads to minimise the wire bonding damage to the wafer.

Regarding the high resistance and dead contacts, poor ohmic metal diffusion is likely the cause, which is due to poor interfacial conditions. As previously explained, metal diffusion in semiconductors such as SiGe happens at lower temperatures than in their oxides. If a semiconductor surface has patches of unclean native oxides, the annealing process produces uneven diffusion. If such patches are widespread enough, the diffusion may be notably compromised. A similar effect is observed for organic contamination. Besides the effects of surface composition, surface roughness also plays a role in diffusion. Smooth surfaces allow even metallic diffusion, while rough surfaces create preferred diffusion paths or barriers which hinder uniform metallisation.

Surface roughness has also another effect, which may be related to the observed gate leakage currents. The ohmic metal must be deposited in a thin layer to avoid non-uniformities on its surface which may pierce the insulating layer that is deposited on top of it. This non-uniformity can, however, propagate from the semiconductor surface as atomic layers are deposited on top of atomic layers during the electron beam evaporation process.

For these reasons it is important to guarantee the surface on which the ohmic metal will be deposited is both clean (free of native oxides and organic contaminants) and smooth. To better understand the surface conditions in Ge/SiGe, we prepared specially etched samples and tested different cleaning recipes. We then performed XPS analysis of the surfaces to investigate how each recipe influences native oxide cleaning and regrowth, as well as organic contaminants. The samples were etched to expose the SiGe layer; a process which in the standard recipe was done solely by a 10% HF solution. In what follows, however, two different etching methods were tested, which are similar to the etching methods employed for mesa etching in the standard recipe: Reactive Ion Etching and chemical etching. The reason for this is two-fold. Firstly, we wanted to test how different etching methods affect surface roughness. Secondly, for particularly deep quantum wells, thin ohmic metal layers may not be enough to reach the Ge layer, in which case the SiGe layer must be pre-etched before metal deposition in order to shorten the distance to the well. In

either case the motivation is to compare and look for methods that can expose the SiGe layer that are gentler and more efficient than the standard HF concentration.

3.3.1 Etching and cleaning

The Reactive Ion Etching process was carried out at the following conditions:

$SF_6/CHF_3/O_2$ 35/10/19 cc/min
Power = 60W
Frequency = 13.6MHz
Pressure = 1.5 Pa
Time = 33s

As for the chemical etch, the recipe used was:

2.3% HF solution for 1 min 30 s (SiO_2 removal)
30% H_2O_2 for 2 min (SiGe etching)
(de-ionised water rinse after each step)

The cleaning recipes employed were:

- **Recipe 1:** 10% HF (2 minutes)
- **Recipe 2:** 2% HF (2 minutes)
- **Recipe 3:** 2% HF (15s) $\rightarrow$ DIW rinse (The cycle is repeated 5 times)
- **Recipe 4:** 2% HF (2 minutes) + H_2O_2 (1 minute)

3.3.2 Results

Figures 3.10 and 3.11 show the Ge and Si tracings by XPS analysis of surface composition after each cleaning method. Figures 3.12 and 3.13 show the ratio of contaminant peaks to elemental peaks for each recipe. We can see that, as expected, the etched but unclean samples have high peaks for Si, Ge, and their native oxides. We can also see that GeO_2 is dominant over the atomic Ge species, while the Si, on the other hand, has not been fully oxidised, indicating the irregular formation of native oxides. All the cleaning solutions perform similarly to each other, with Recipe 3 and Recipe 4 being slightly more efficient. No recipe completely removes the Ge oxide, which can be attributed to its fast re-growth rate. The exposure to air in between processing steps is enough for the regrowth to occur, explaining the persistent presence of oxides.

From Figure 3.14 we can see the strong presence of O_2 molecules on unclean surfaces and some presence in cleaned surfaces as well. This is attributed to adsorbed oxygen molecules. As for organic contaminants, these can be traced by looking at

C peaks, as shown in Figure 3.15. This Figure has an added curve for fully coated samples, so the interference of the photoresist can be accounted for. Small peaks can be observed for C, and, specially in the case of unclean samples, these can be understood as organic contamination. The large peaks to the right, however, are most likely indicating readings from the coated borders of the measurement areas, but persistent resist contamination, as well as other kinds of organic contaminations, cannot be ruled out.

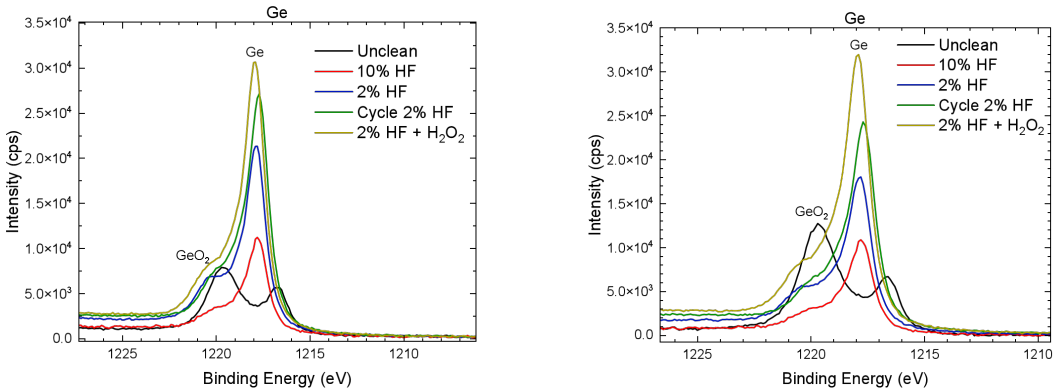

(a) Plasma etching. (b) Chemical etching.

FIGURE 3.10: **Ge XPS tracing:** Curves showing Ge and GeO_2 surface components for **a)** plasma etched and **b)** chemically etched samples. We can see that while native oxide peaks are dominant for unclean samples, Ge peaks are the main contribution for every cleaning recipe. Nevertheless, small oxide contributions are present for every case.

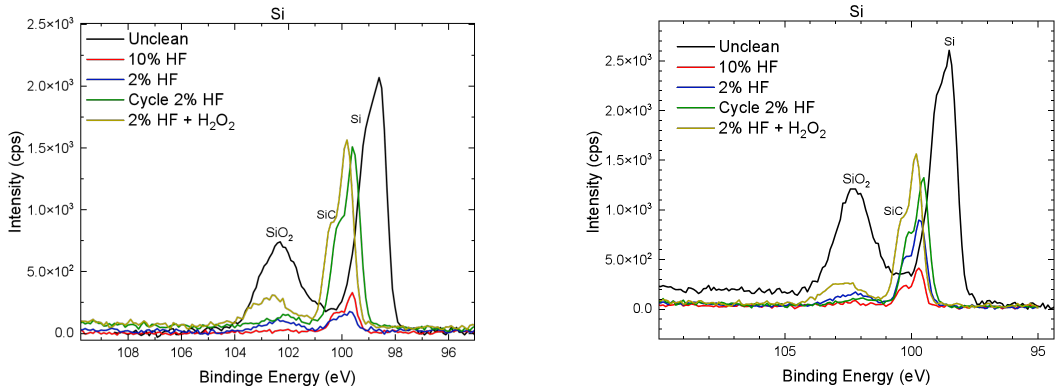

(a) Plasma etching. (b) Chemical etching.

FIGURE 3.11: **Si XPS tracing:** Curves showing Si and SiO_2 surface components for **a)** plasma etched and **b)** chemically etched samples. Contrary to the Ge case, the Si peaks are dominant for unclean and clean samples. Small oxide contributions are, however, also present for every case.

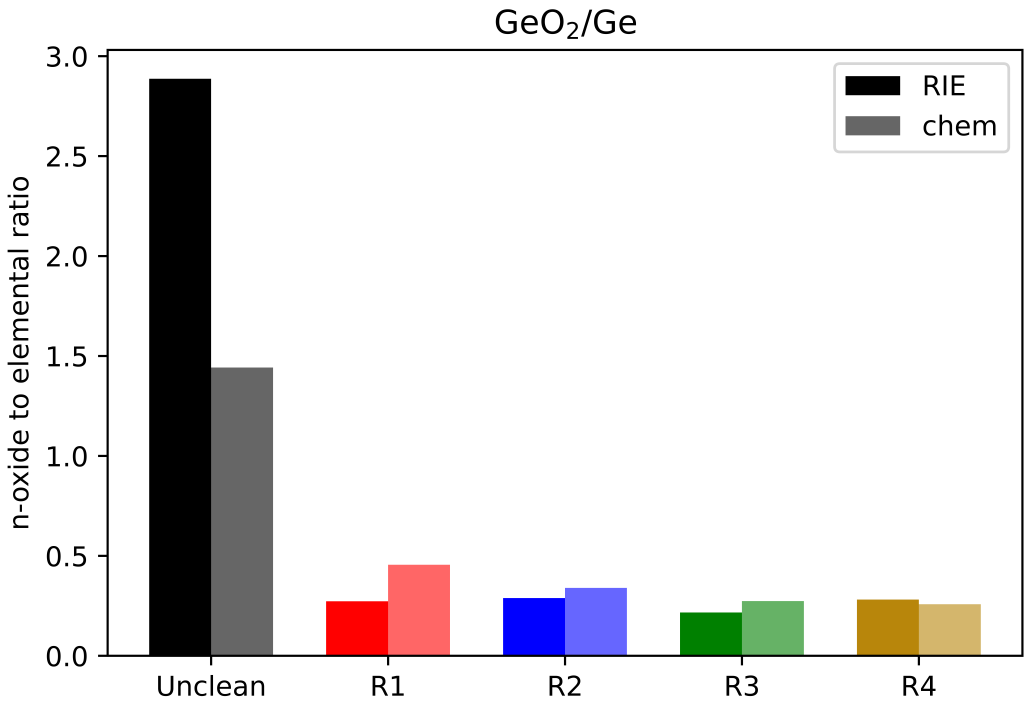

FIGURE 3.12: **Contaminants-to-Ge ratio Rn:** n varies from 1 to 4, corresponding to Recipe n. We can see that, while all cleaning recipes perform similarly, Recipes 3 and 4 are slightly more efficient.

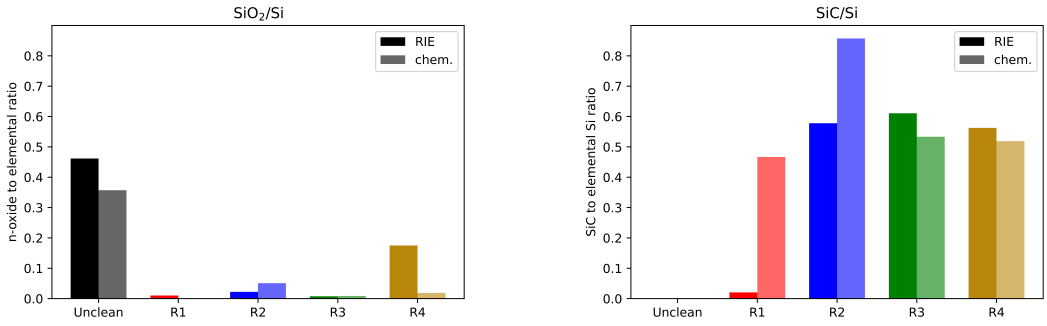

(a) Si oxide to Si XPS peaks ratio.

(b) SiC to Si XPS peaks ratio.

FIGURE 3.13: **Contaminants-to-Si ratio Rn:** n varies from 1 to 4, corresponding to Recipe n. **a)** Recipes 2 and 3 are the most efficient. b) All recipes perform similarly, except for Recipe 2 on RIE etched surfaces which is notably more efficient.

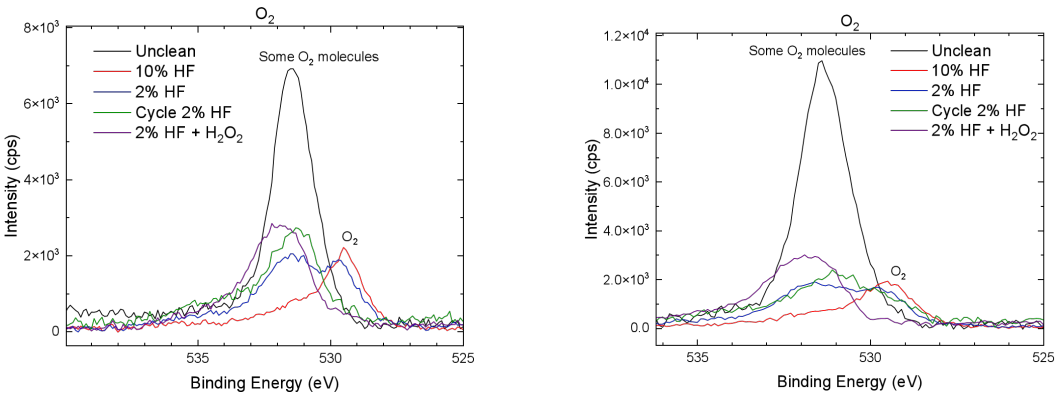

(a) Plasma etching. (b) Chemical etching.

FIGURE 3.14: **O_2 XPS tracing:** Adsorbed O_2 molecules are present in every case.

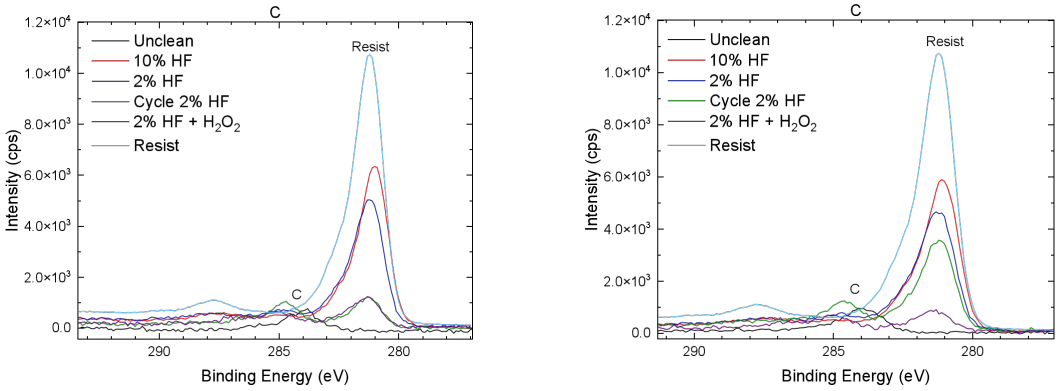

(a) Plasma etching. (b) Chemical etching.

FIGURE 3.15: **C XPS tracing:** The persistent presence of C peaks is most likely due to the XPS reading the resist on the borders of the measurement area. This explains why the unclean samples have less pronounced C peaks, as those were measured without any resist coating the sample at all. This interference in the reading makes it difficult to separate contributions from actual organic contaminants from unintended resist reading.

Besides the cleaning efficiency of the recipes, how they chemically attack the SiGe surface is also an important aspect to monitor, as increased roughness may create leakage paths and promote uneven diffusion of ohmic metals. The roughness is estimated from the Root Mean Square (RMS) of height measurements:

$$y_{\text{RMS}} = \sqrt{\frac{1}{n}}\sqrt{(y_1^2 + y_2^2 + ... + y_n^2)}, \tag{3.10}$$

where y_i is the difference between the height of a given site and the average height of all sites. A smooth surface has similar heights at different points and so the RMS is small when compared to a rough surface where each individual points have larger variations amongst themselves.

Figure 3.16 shows the AFM analysis of an unetched surface (a), a Reactive Ion etched surface (b), and a chemically etched surface (c). We can see the unetched surface is the smoothest, with an Root Mean Square (RMS) of 0.385 nm. RIE is the most damaging technique, with RMS = 1.04 nm, while chemical etching has RMS = 0.606 nm.

Figures 3.17 and 3.17 show the effect of each cleaning recipe on the wet etched and plasma ethced samples' surfaces, respectively. The RMS results are averaged from measurements in different areas treated by the same recipes. The initial etching method of choice seems not to have a dominant relevance in the process, as chemical processes of cleaning, which are similar to the chemical etching process, smooth out initial differences. Due to technical reasons, the area corresponding to Recipe 2 was unable to be measured. We can see, however, that the standard cleaning method (Recipe 1), with 10% HF solution, creates a relatively rough surface, with average RMS = 2.124 nm. Recipe 4, combining low concentration HF solution (2%) and Hydrogen peroxide, provided the smoothest surface with average RMS = 0.553 nm. Recipe 3 showed a very rough surface, with average RMS = 2.396 nm. This could be attributed to the short time of the 2% HF dip (15s) and to the frequent transfer between beakers in-between cycle steps, which could re-start the Ge oxide growth process every turn.

In summary, cyclic 2% HF and 2% HF + Hydrogen peroxide recipes seem to be the most efficient in removing oxides, but the Hydrogen peroxide approach helps smoothing the final surface. Nearly all of the failed devices can be traced back to interfacial defects; be them at the semiconductor-insulator interface, causing gate leakage, or at the semiconductor-ohmic metal interface, compromising proper diffusion. Rigorous surface treatment optimisation must be carried out to improve yield and overall quality of the devices.

For Ge, in particular, the native GeO_2 layer is inherently problematic. Unlike SiO_2, GeO_2 is hygroscopic and thermally unstable. On the other hand, it easily forms in laboratory conditions, with the possibility of creating irregular native oxide patches on the exposed SiGe layer, potentially compromising ohmic metal diffusion. Regarding the surface treatment pre-insulating layer deposition, a non-uniform Si capping layer may leave exposed areas of the underlying SiGe layer, causing the oxidation of Ge atoms. Experimental studies have shown interfacial GeO_2 layers

to severely degrade devices' C-V characteristics, facilitating high gate leakage via the abundant presence of interface traps [137]. The use of dilute HF solutions in association with pulsed cycles of Alumina precursor and water in the ALD chamber in order to completely remove the native oxide layer for GaAs has been reported [138], which could be an option for SiGe heterostructures as well. HF solutions, however, are etchant to SiO_2, which could further compromise the interfacial states.

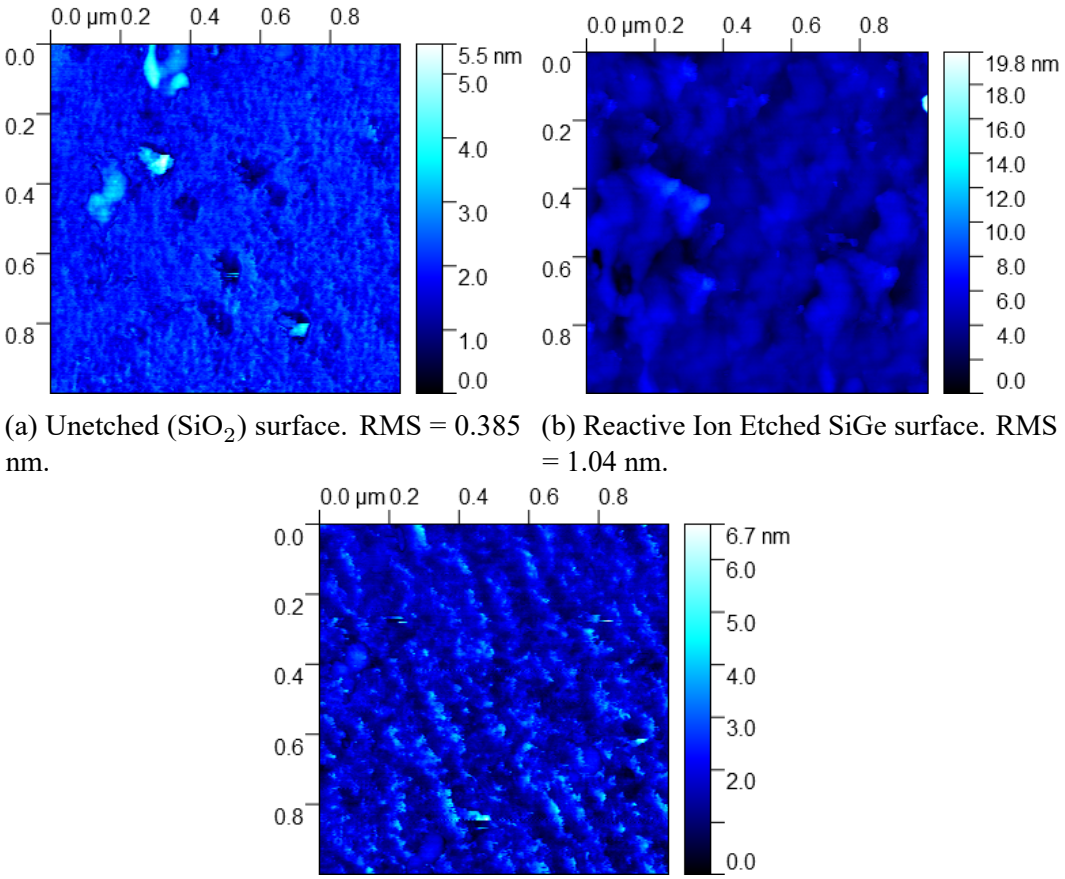

(a) Unetched (SiO_2) surface. RMS = 0.385 nm.

(b) Reactive Ion Etched SiGe surface. RMS = 1.04 nm.

(c) Chemically etched SiGe surface. RMS = 0.606 nm.

FIGURE 3.16: **Pre-treatment AFM imaging:** a) Unetched surface. b) Reactive Ion etched surface. c) Chemically etched surface.

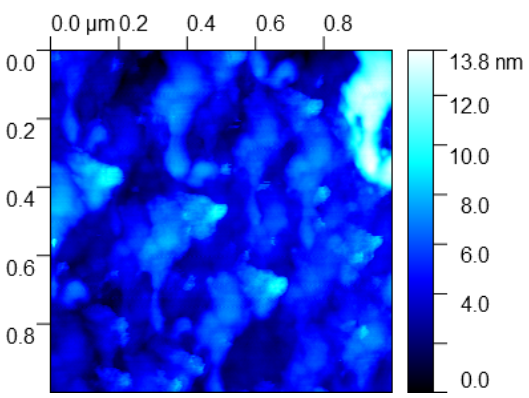

(a) Recipe 1. RMS = 2.040 nm.

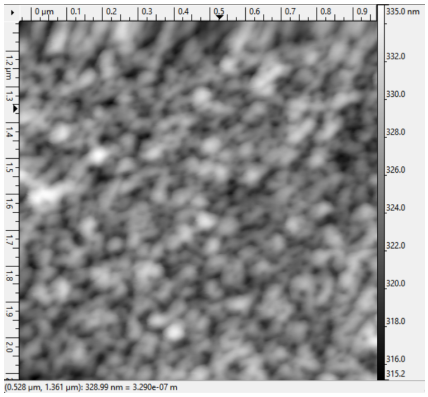

(b) Recipe 3. RMS = 2.205 nm.

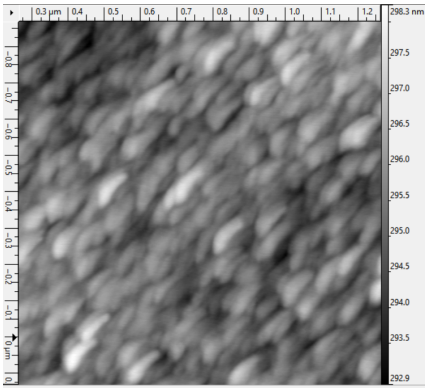

(c) Recipe 4. RMS = 0.575 nm.

FIGURE 3.17: **Post-treatment AFM imaging for wet etched samples:** a) Recipe 1. b) Recipe 3. c) Recipe 4. Due to technical issues, the measurement area corresponding to Recipe 2 could not be measured.

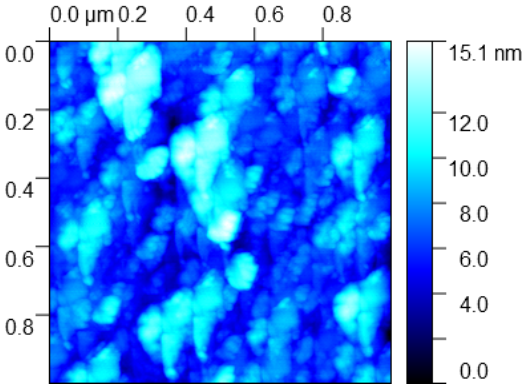

(a) Recipe 1. RMS = 2.208 nm.

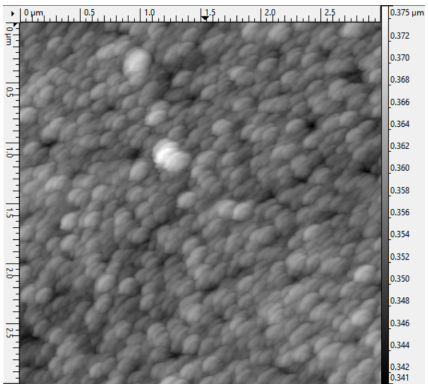

(b) Recipe 3. RMS = 2.587 nm.

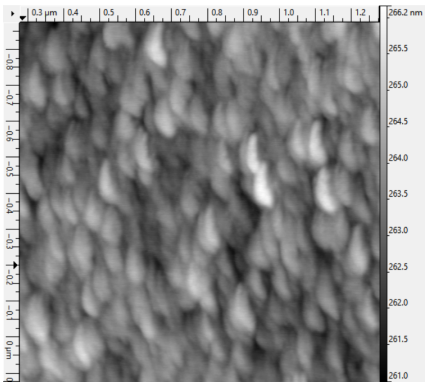

(c) Recipe 4. RMS = 0.531 nm.

FIGURE 3.18: **Post-treatment AFM imaging for plasma samples:** a) Recipe 1. b) Recipe 3. c) Recipe 4. Due to technical issues, the measurement area corresponding to Recipe 2 could not be measured.

4

Transport characterisation

4.1 Classical transport

Charge transport in a solid refers to how charge carriers move through a material when an electric field or other driving forces are applied. Classical transport is described by the Drude model, which considers charges move freely in between scattering events. The average time between these collisions is called the relaxation time τ. When collisions do occur, the particles' velocities are randomised. This scattering process is caused either by phonons or by impurities in the material. In a uniform electric field, the charges' motion is described by

$$m^* \frac{d\langle \mathbf{v} \rangle}{dt} = -e\mathbf{E} - m^* \frac{\langle \mathbf{v} \rangle}{\tau}, \tag{4.1}$$

where m^* is the effective mass and e is the electronic charge. When the system reaches a steady state, that is, $\frac{d\langle \mathbf{v} \rangle}{dt} = 0$,

$$\langle \mathbf{v} \rangle = -\frac{e\tau}{m^*}\mathbf{E}. \tag{4.2}$$

The current density is defined as the product of the carrier density and their average velocity:

$$\begin{aligned} \mathbf{j} &= ne\mathbf{v} \\ &= ne\left(\frac{e\tau}{m^*}\right)\mathbf{E} \\ &= \frac{ne^2\tau}{m^*}\mathbf{E}, \end{aligned} \tag{4.3}$$

where n is carrier density. In a two-dimensional system, n represents the 2D areal density of carriers and σ has units of conductance (Ω^{-1}), since the thickness is effectively single-layered. From Ohm's law, which establishes the relation between current density and the applied electric field via the conductivity σ, $\mathbf{j} = \sigma\mathbf{E}$, we have that

$$\sigma = \frac{ne^2\tau}{m^*}. \tag{4.4}$$

The resistivity of this system is given by

$$\rho = \frac{1}{\sigma} = \frac{m^*}{ne^2\tau}. \tag{4.5}$$

In the presence of a magnetic field, equation (4.1) must take into account a term of the form $\langle \mathbf{v} \rangle \times \mathbf{B}$. This term mixes contributions from different directions in the plane of motion, turning the conductivity into a tensor. Assuming the plane of motion is the $x-y$-plane, and the magnetic field is applied along the z-direction we have

$$\sigma = \frac{ne^2\tau}{m^*} \frac{1}{1+(\omega_c\tau)^2} \begin{bmatrix} 1 & -\omega_c\tau \\ \omega_c\tau & 1 \end{bmatrix}, \tag{4.6}$$

where

$$\omega_c = \frac{eB}{m^*} \tag{4.7}$$

is the cyclotron frequency. By inverting equation (4.6) we obtain the corresponding resistivity tensor:

$$\rho = \frac{m^*}{ne^2\tau} \begin{bmatrix} 1 & \omega_c\tau \\ -\omega_c\tau & 1 \end{bmatrix}. \tag{4.8}$$

The off-diagonal terms describe the classical Hall effect. When a magnetic field is applied perpendicularly to the current plane, the Lorentz force deflects moving charges, leading to a transverse *Hall voltage* V_H. These terms are

$$\rho_{xy} = -\rho_{yx} = \frac{B}{ne}. \tag{4.9}$$

In an experimental setting, we apply a current I along, for example, the x-direction and measure the voltage drop V_H on the transversal direction. In a two-dimensional system the current density is given by

$$j_x = \frac{I}{w}, \tag{4.10}$$

where w is the width of the current channel. The electric field built by charge accumulation on the edges of the channel, along the y-direction, is given by:

$$E_y = \rho_{yx}\, j_x = \rho_{yx}\, \frac{I}{w}. \tag{4.11}$$

The Hall voltage V_H is then

$$V_H = E_y\, w = \rho_{yx}\, \frac{I}{w} \cdot w = \rho_{yx}\, I. \tag{4.12}$$

We can see that the Hall resistance (equivalent in a 2D system to the resistivity) is then

$$R_{xy} = \frac{V_H}{I} = \rho_{yx} = R_H B, \tag{4.13}$$

where

$$R_H = \frac{1}{ne} \tag{4.14}$$

is the Hall coefficient. The Hall resistivity increases linearly with B and can be used to measure n. The measurement of the Hall voltage thus reveals the carrier density and type: the carrier density depends on the slope of the Hall resistance and its sign depends on the carrier type (electrons or holes). The Hall mobility

$$\mu = \sigma R_H = \frac{e\tau}{m^*} \tag{4.15}$$

can also be obtained, characterizing how freely carriers move in the material.

4.2 Quantum transport

When magnetic fields becomes sufficiently strong, the classical description breaks down and quantum effects become relevant. In 1930, Soviet Physicist Lev Landau showed that electrons in a uniform magnetic field B have quantized cyclotron orbits with discrete energies levels; now known as Landau levels [139]. That same year, Dutch physicists Wander Johannes de Haas and Pieter van Alphen, and Soviet physicist Lev Shubnikov and de Haas discovered oscillatory magnetic effects in Bismuth, which was explained by Landau's theory. The *de Haas-van Alphen* (dHvA) effect describes quantum oscillations in magnetisation, a thermodynamic property [140, 141], while the *Shubnikov-de Haas* (SdH) effect accounts for quantum oscillations in electrical resistance, a transport property [142]. Both these phenomena are macroscopic quantum effects arising from Landau quantisation and are periodic in $1/B$. They result from the oscillation of the density of states as Landau levels sweep through the Fermi level E_F and are successively depopulated.

4.2.1 Shubnikov-de Haas oscillations

The Hamiltonian for a two-dimensional system under a uniform magnetic field is given by

$$H = \frac{1}{2m^*}\left[\mathbf{p} + e\mathbf{A}(\mathbf{r}, t)\right]^2, \tag{4.16}$$

where m^* is the effective mass, e is the particle's charge and $\mathbf{A}(\mathbf{r}, t)$ is the vector potential. Under the Landau gauge, $\mathbf{A} = (0, Bx, 0)$, and the Hamiltonian becomes

$$H = \frac{1}{2m^*}\left[p_x^2 + (p_y + eBx)^2\right]. \tag{4.17}$$

We can see that in this gauge, $[p_y, H] = 0$, so p_y is a conserved quantity, making it a good quantum number ($p_y \to k_y$).

$$H = \frac{p_x^2}{2m^*} + \frac{1}{2}m^*\omega_c^2\left(x + \frac{\hbar k_y}{eB}\right)^2. \tag{4.18}$$

where $\omega_c = eB/m^*$ is the cyclotron frequency. This equation has the same form of the harmonic oscillator Hamiltonian with a guiding center

$$x_0 = -\frac{\hbar k_y}{eB} = -k_y \ell_B^2, \tag{4.19}$$

where

$$\ell_B = \sqrt{\frac{\hbar}{eB}} \tag{4.20}$$

is the magnetic length. The quantised energies of this system, the Landau levels, are given by

$$E_n = \hbar\omega_c \left(n + \frac{1}{2}\right). \tag{4.21}$$

To account for finite sample dimensions, we now consider the spatial confinement of the system. In the x-direction, the sample extends from $x = 0$ to $x = L_x$. Recalling the the guiding centre given by equation (4.19), we impose that the centre of the cyclotron orbit lies within the physical sample:

$$0 < -k_y \ell_B^2 < L_x \quad \Rightarrow \quad -\frac{L_x}{\ell_B^2} < k_y < 0. \tag{4.22}$$

In a finite geometry, the momentum k_y is quantised due to periodic boundary conditions in the y-direction:

$$k_y = \frac{2\pi}{L_y} j, \quad j \in \mathbb{Z}. \tag{4.23}$$

The number of allowed k_y values, that is, the degeneracy of each Landau level—is given by the number of distinct guiding centres that fit within the sample:

$$D = \frac{L_x L_y}{2\pi \ell_B^2} = \frac{eB}{h} A, \tag{4.24}$$

where $A = L_x L_y$ is the area of the sample. This shows how the Landau levels are highly degenerate. Physically, the guiding centre of the cyclotron orbit can be anywhere in the plane. For each E_n, one can choose any k_y, leading to a continuum of states along y with the same energy. In a system of area A, one finds approximately $\frac{A\,eB}{h}$ states per Landau level (spin degeneracy neglected), meaning each level can accommodate $\frac{eB}{h}$ electrons per unit area. This large degeneracy reflects the fact that the applied field "assembles" the otherwise continuous 2D free-electron states into discrete Landau levels, without changing the total density of states.

Semi-classically, electrons in a magnetic field trace closed circular orbits in momentum space (**k**-space). The area enclosed by such an orbit is

$$A_k = \pi k_F^2. \tag{4.25}$$

According to the Onsager quantisation condition, allowed orbits in **k**-space are quantised via

$$A_k = \frac{2\pi eB}{\hbar}(n+\gamma), \tag{4.26}$$

where $n \in \mathbb{N}_0$, and $\gamma \approx \frac{1}{2}$ for parabolic bands. At the Fermi level, electrons occupy all states up to the largest k-space orbit:

$$A_F = A_k(E_F) = \pi k_F^2. \tag{4.27}$$

Solving for the Fermi wavevector:

$$k_F = \sqrt{\frac{A_F}{\pi}}. \tag{4.28}$$

In a two-dimensional system, each quantum state in **k**-space occupies an area

$$\Delta k_x \Delta k_y = \frac{(2\pi)^2}{A}, \tag{4.29}$$

where A is the real-space area of the sample. The number of available states within a circular Fermi surface of radius k_F is

$$\begin{aligned} N &= g_s \cdot \frac{\text{area in } \mathbf{k}\text{-space}}{\text{area per state}} \\ &= g_s \cdot \frac{\pi k_F^2}{(2\pi)^2/A} \\ &= g_s \cdot \frac{A \cdot k_F^2}{4\pi}, \end{aligned} \tag{4.30}$$

where $g_s = 2$ accounts for spin degeneracy. Dividing by the area A, we obtain the electron density:

$$n = \frac{N}{A} = \frac{g_s}{4\pi}k_F^2 = \frac{1}{2\pi}k_F^2. \tag{4.31}$$

Solving for $A_F = \pi k_F^2$, we find:

$$A_F = 2\pi n, \tag{4.32}$$

which gives

$$k_F = \sqrt{2\pi n}. \tag{4.33}$$

For a magnetic field value B_n at which the n-th Landau level aligns exactly with the Fermi energy, we have that

$$E_F = \hbar\omega_c \left(n + \frac{1}{2}\right). \tag{4.34}$$

Solving for B, we find:

$$\frac{1}{B_n} = \frac{e}{\hbar} \cdot \frac{1}{m^* E_F}\left(n + \frac{1}{2}\right), \tag{4.35}$$

which reveals that Landau level crossings are periodic in $1/B$. The spacing between successive Landau level crossings in $1/B$ defines the period:

$$\Delta\left(\frac{1}{B}\right) = \frac{1}{B_{n+1}} - \frac{1}{B_n}. \tag{4.36}$$

Using the Onsager relation, we obtain that

$$A_k = \frac{2\pi e B_n}{\hbar} \quad \Rightarrow \quad \Delta\left(\frac{1}{B}\right) = \frac{2\pi e}{\hbar A_k}. \tag{4.37}$$

Since at the energy crossing

$$A_k = A_F = 2\pi n, \tag{4.38}$$

we have that

$$\Delta\left(\frac{1}{B}\right) = \frac{e}{\hbar n}. \tag{4.39}$$

As B varies, the Landau levels move through E_F, causing oscillations in occupancy. At low B (weak field), many Landau levels are occupied and overlap (smearing out quantization). At high B, however, the Landau levels are well-separated if $\hbar\omega_c \gg k_B T$ and $\hbar\omega_c$ exceeds the level broadening Γ, which characterises the disorder-induced linewidth or scattering-induced energy uncertainty of the Landau levels.

4.2.2 The Lifshitz-Kosevich formula

In 1956, Soviet physicists Isaak Markovich Lifshitz and Alexei Kosevich performed a rigorous analysis of the amplitude of quantum oscillations, taking temperature and scattering into consideration [143]. The derivation of their formula, now known as the Lifshitz-Kosevich formula, is based on calculations of the oscillatory part of the grand potential of electrons in a magnetic field. From this oscillatory part quantities like magnetisation and conductivity can be derived.

The grand canonical potential $\Omega(\mu, B)$ of electrons can be written as a sum over Landau level energies. At $T = 0$,

$$\Omega = -\sum_{n,\sigma} f(E_n - \mu), \tag{4.40}$$

(plus integrals for continuum parts), where f is the energy occupancy (Heaviside step at μ) and σ accounts for spin degeneracy. This sum can be evaluated using the Poisson summation (Euler-MacLaurin) method by separating the smooth and oscillatory contributions. The oscillatory contribution arises from the discrete Landau level index and is roughly proportional to

$$\cos\left(2\pi\frac{E_F}{\hbar\omega_c} + \varphi\right). \tag{4.41}$$

The pre-factor decays with T and with the Landau level broadening. The oscillation amplitude ΔX of a given observable X can then be generally written as the product of three factors: a temperature damping factor R_T, a disorder (Dingle) damping factor R_D, and an overall pre-factor related to the average magnitude of oscillation. For the Shubnikov-de Haas oscillation amplitude in resistivity, we can write

$$\Delta X(B) \;\propto\; R_T R_D \cos\Big(\frac{2\pi F}{B} + \varphi\Big)\,, \tag{4.42}$$

where F is the oscillation frequency in $1/B$, and φ is a phase offset. The thermal smearing factor R_T, and the impurity scattering factor R_D are given by

$$R_T \;=\; \frac{X}{\sinh X}\,, \qquad \text{with} \quad X \;\equiv\; \frac{2\pi^2 k_B T}{\hbar\omega_c}\,, \tag{4.43}$$

and

$$R_D \;=\; \exp\Big(-\frac{2\pi^2 k_B T_D}{\hbar\omega_c}\Big)\,, \tag{4.44}$$

where T_D is the Dingle temperature, which is related to the Landau level broadening via the quantum lifetime τ:

$$k_B T_D = \hbar/(2\pi\tau). \tag{4.45}$$

The Lifshitz–Kosevich formula for the oscillatory part of the longitudinal resistivity $\Delta\rho_{xx}$ is given by

$$\Delta\rho_{xx}(B) \;\propto\; \rho_0 \frac{X}{\sinh X} e^{-X_D} \cos\Big(\frac{2\pi F}{B} + \varphi\Big)\,, \tag{4.46}$$

where ρ_0 is the zero-field conductivity. The regime where the Landau levels separation becomes significant requires that $\omega_c\tau > 1$. This means that electrons can complete at least one cyclotron orbit before scattering. This is the condition for observing pronounced quantum oscillations in transport.

At very high fields or in materials with large g, the Zeeman splitting of Landau levels can be comparable to $\hbar\omega_c$, leading to what is called Shubnikov-de Haas beating: a change in the Shubnikov-de Haas oscillation frequency depending on the difference between the Fermi surfaces for spin-up and spin-down. Analysing such spin-split oscillations yields information on the g-factor and spin-orbit effects.

4.2.3 Quantum Hall effect

As for the transversal resistivity, at sufficiently high magnetic fields, the system enters the *quantum Hall regime*, where the cyclotron frequency dominates the scattering rate: $\omega_c\tau \gg 1$. In this regime, the Landau levels are well separated, and the longitudinal resistivity ρ_{xx} drops to zero between oscillation minima. Simultaneously, the Hall resistivity ρ_{xy} exhibits *plateaus* at quantised values. Each plateau corresponds to

an integer number of completely filled Landau levels. In these regions, the Hall resistivity is given by

$$\rho_{xy} = \frac{h}{\nu e^2}, \tag{4.47}$$

where $\nu \in \mathbb{Z}$ is the *filling factor*. The *width* of the Hall plateaus as a function of magnetic field reflects the role of disorder. A certain degree of disorder is necessary to localise electronic states between Landau levels, which stabilises the quantisation and broadens the plateaus. In cleaner systems, plateaus may be narrower, as fewer states are localised.

When the filling factor ν is an integer, the Fermi level lies in an *energy gap* between Landau levels. All states at the Fermi energy are then localised and do not contribute to longitudinal conduction, leading to

$$\rho_{xx} \to 0, \tag{4.48}$$

and a quantised Hall conductivity

$$\sigma_{xy} = \nu \frac{e^2}{h}, \tag{4.49}$$

which remains constant even as the magnetic field varies, resulting in flat plateaus in $\rho_{xy}(B)$. As the magnetic field is swept, the next Landau level begins to populate and delocalised states contribute to transport. This causes an increase in ρ_{xy} between plateaus and a peak in ρ_{xx} due to enhanced longitudinal conduction. This alternating pattern of plateaus and peaks gives rise to the characteristic *quantum Hall staircase*.

4.3 Measurements

In this section we present the measurement protocols and results obtained from doped and undoped samples fabricated as described in ***Chapter 3***, using the standard fabrication recipe. In particular, we present results for transport measurements under light-irradiation. The measurements were conducted in an *Oxford Instruments Heliox* cryogenic unit. The electric current applied between source and drain terminals of the Hall bars was

$$I = 100\text{nA}, \tag{4.50}$$

and a varying magnetic field was applied perpendicularly to it. Longitudinal and transverse voltages were measured for positive and negative values of the magnetic field, and the corresponding resistivities were computed. To suppress antisymmetric contributions, the measured voltages were averaged as follows:

$$\Delta V_{x\alpha} = \frac{\Delta V_{x\alpha}(B > 0, I) + \Delta V_{x\alpha}(B < 0, -I)}{2}, \tag{4.51}$$

where $\alpha \in x, y$ corresponds to longitudinal ($\alpha = x$) and transverse ($\alpha = y$) voltages, respectively. For the longitudinal resistivity, which reveals the Shubnikov–de Haas

oscillations, a third-order polynomial fit is applied to the data in order to subtract the smooth background from the purely oscillatory component. The resulting signal can then be analysed using the Lifshitz–Kosevich theory:

$$\Delta\rho_{xx} = \rho_{xx} - P^{(3)}_{\text{fit}}(\rho_{xx}), \tag{4.52}$$

where $P^{(3)}_{\text{fit}}(\rho_{xx})$ denotes the third-order polynomial fit to the dataset ρ_{xx}. After this, the independent variable is transformed from magnetic field B to its reciprocal,

$$\Delta\rho_{xx}(B) \to \Delta\rho_{xx}(1/B), \tag{4.53}$$

in order to make the frequency dependence of the oscillations explicit. By repeating the measurements at different temperatures, the damping effect on the oscillations can be verified and fit to equation (4.46) to obtain the effective mass and quantum time.

Sample A and **sample C** were measured under irradiation of LED light sources with wavelengths 1.55μm and 1.3μm, respectively. Both configurations provide photons with enough energy to bridge the band gap. In these experiments, the LED was mounted on the same PCB as the samples. **Sample B** was used as a test for the measurement protocol and was not irradiated. For this reason we begin the measurements discussion with this sample. The experimental set-up has the LED light source mounted on the same PCB as the sample, positioned over it, with an approximate distance of 1.5 cm between them.

4.3.1 Sample B: Doped sample

The doped samples were the best-behaved ones, which further confirms the delicate nature of processes involving insulating layers and top gates. Ordinarily, undoped samples are preferred for quantum devices such as quantum dots, due to the possibility of tuning transport properties via gate voltages. However, for the specific purpose of using quantum dots as a platform for light-spin interaction in quantum repeaters, there is a compelling reason to consider doped heterostructures. Metal gates are highly absorbent to light and significantly reduce the transmittance of the device. While the choice of metal and the thickness of the gate both affect optical transmittance, in all cases the conversion efficiency is compromised.

From Figure 4.1 we can see the Shubnikov-de Haas oscillations and the quantum Hall effect curves. The magnetic field was swept from 0 to 14T (absolute values). From Figure 4.1a we can see the longitudinal resistivity starts to go to zero around 12 T, indicating a considerable degree of disorder in the system. Figure 4.1b shows the filling factors of the Hall plateaus. At 14 T the lowest filling factor achieved is $\nu = 5$.

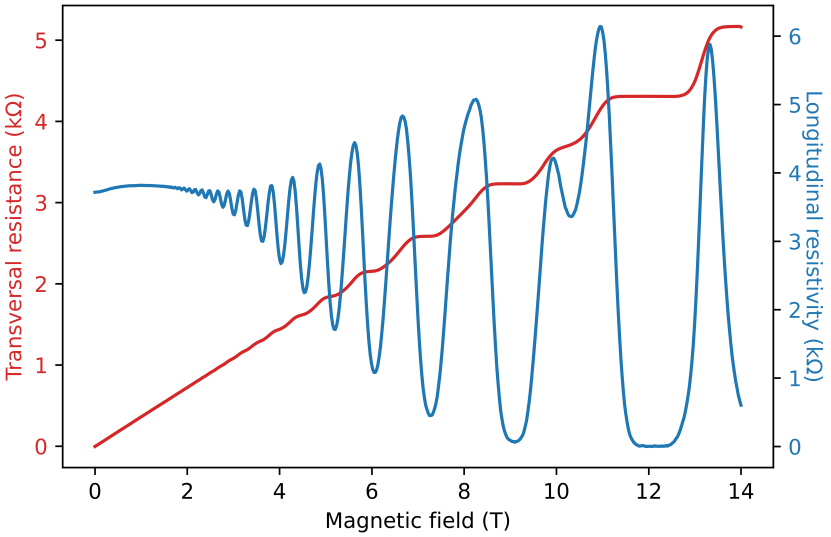

(a) Shubnikov-de Haas oscillations and quantum Hall effect.

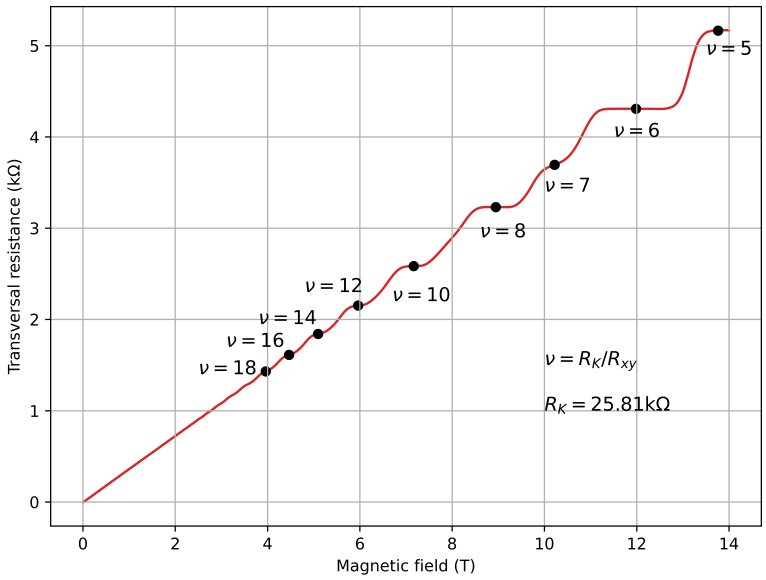

(b) Quantum Hall plateaus with filling factors.

FIGURE 4.1: **Shubnikov-de Haas oscillations and quantum Hall effect curves.**

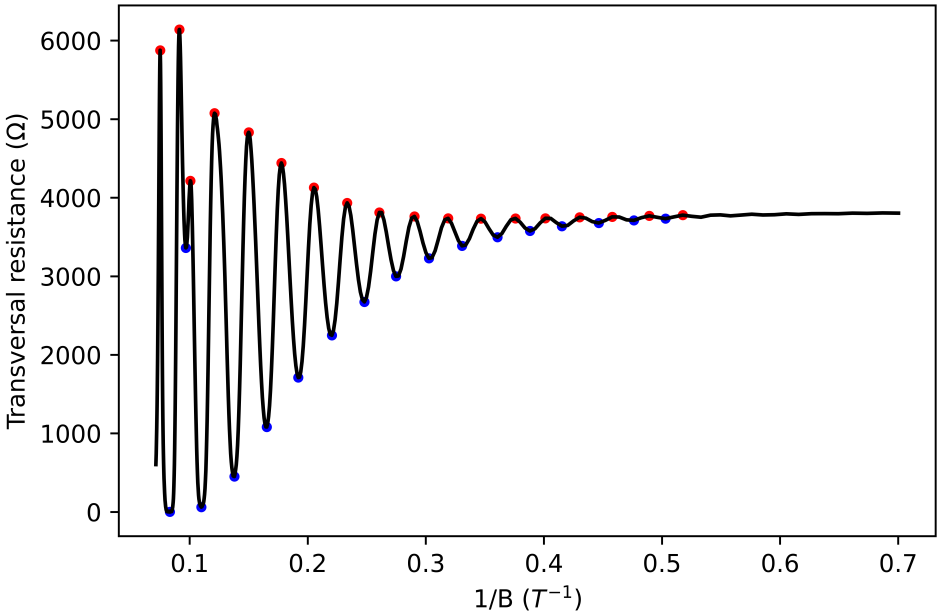

(a) Shubnikov-de Haas oscillations as a function of the magnetic field reciprocal.

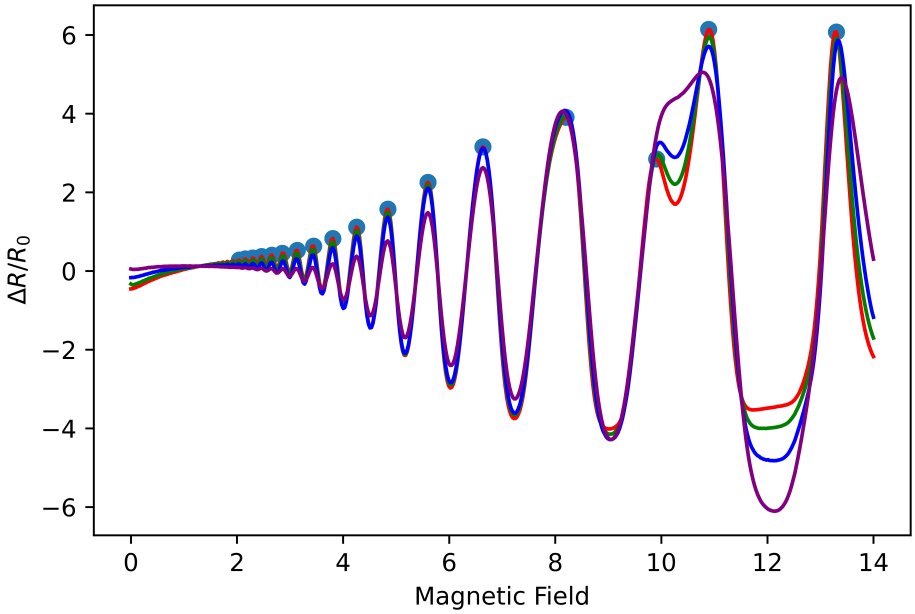

(b) Temperature damping of Shubnikov-de Haas oscillations. The temperatures range from 0.3 to 4.2K.

FIGURE 4.2: **Shubnikov-de Haas oscillations analysis.**

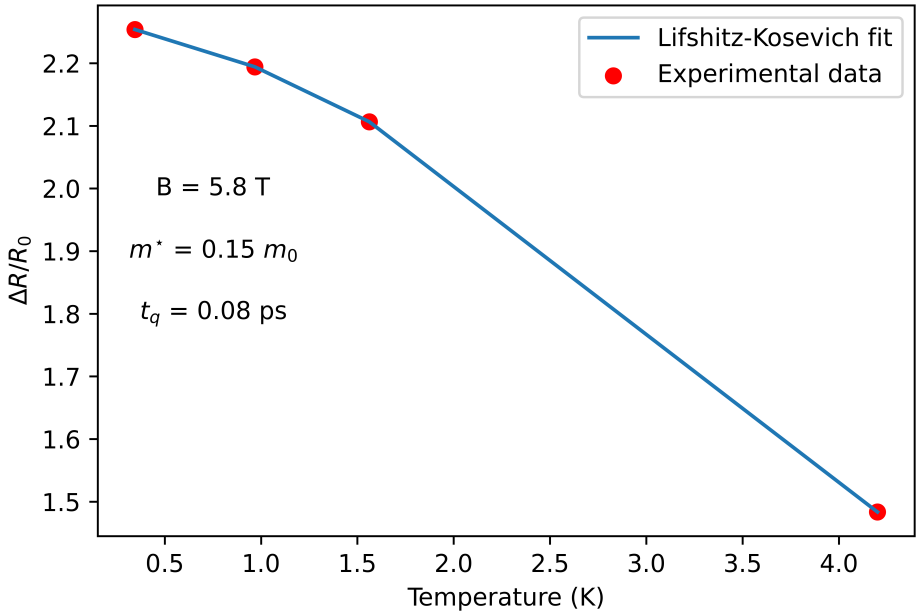

FIGURE 4.3: **Lifshitz-Kosevich fit:**. It shows an effective mass of 0.15 $_0$ and a quantum lifetime of 0.08 ps, indicating a high number of scattering events.

Figure 4.2a shows the Shubnikov-de Haas oscillations as a function of the magnetic field's reciprocal $1/B$. Figure 4.2b shows the oscillations for different temperatures, ranging from 0.3K to 4.2K. We can see that, as the temperature increases the amplitude of the oscillations is damped. Using this data we can perform a Lifshitz-Kosevich fit to extract the effective mass m^* and the quantum lifetime τ_q. The effective mass was measured to be 0.15 m_0, in agreement with previous reports [144]. The quantum lifetime τ_q is 0.08ps, indicating a high number of scattering events.

4.3.2 Sample A: light irradiation (1.55 um)

Sample A was measured under light irradiation of an 1.55μm LED light source. Such LEDs are not designed for cryogenic operation and need higher voltages than described on their data-sheet to achieve nominal currents and corresponding emissions. This raises the temperature in the fridge, making it hard to keep stable temperatures below 4.2K for long times. To avoid quenching from the electromagnet, its electric current rate must be set at low values, increasing the total time of the experiment. In our case, sweeping from 0 to 8T took approximately 90 minutes, making the light irradiation at lower temperatures unfeasible.

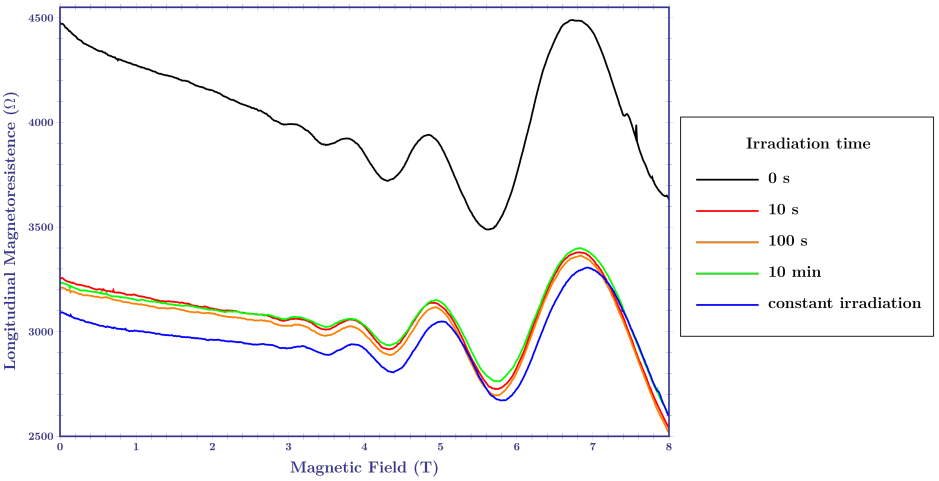

(a) Shubnikov-de Haas oscillations for different irradiation times.

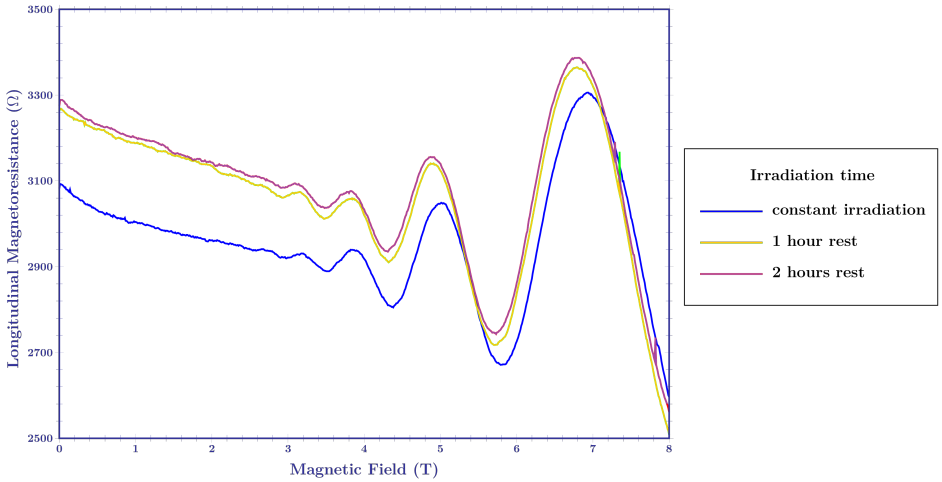

(b) Shubnikov-de Haas oscillations in the dark after 1 and 2 hours rest. We can see the curves are shifting back upwards.

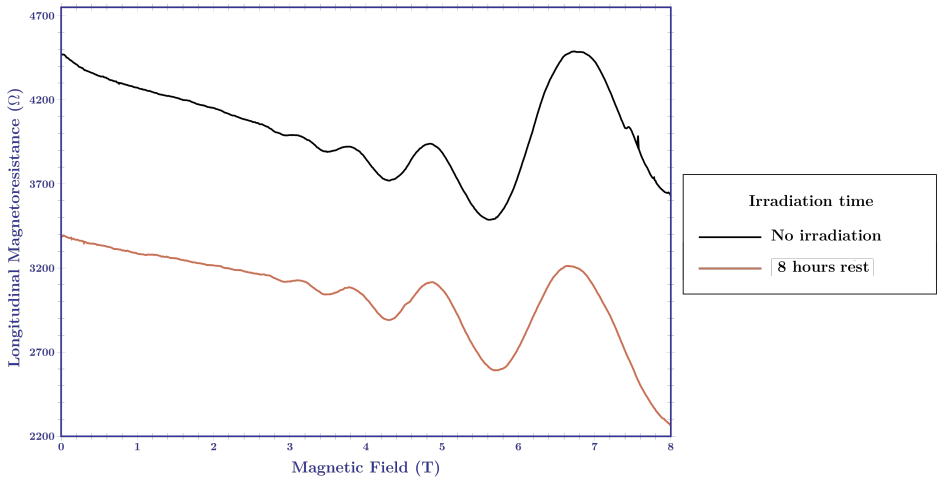

(c) Shubnikov-de Haas oscillations in the dark after 8 hours rest. The curve is beginning to approach the dark measurement values.

FIGURE 4.4: **Doped sample Shubnikov-de Haas oscillations under light irradiation:** Different illumination regimes using a 1.55μm LED.

This sample was not gated, despite being nominally undoped, but it nevertheless displayed Shubnikov-de Haas oscillation patterns, indicating an unintentional doping in the growth process. Five irradiation regimes were used: dark, 10s, 100s, 10min, and constant irradiation. The LED was operated for different amount of times, turned off, and then the magnetic sweep would be initiated. For the constant irradiation regime the LED was kept on during the full duration of the experiment. We can see from Figure 4.4a that the effect of illumination was to shift the longitudinal resistivity downwards, without dramatically changing the oscillation pattern. Figure 4.4b shows the persistence of the resistivity shift in dark measurements after 1, and 2 hours and Figure 4.4c after 8 hours rest, following the constant irradiation regime.

Figure 4.5 shows the charge carrier concentration and mobility as a function of the irradiation time. We can see that after initial illumination both quantities remain virtually constant. The initial improvement in mobility and charge carrier concentration is most likely due to photo-ionisation of shallow donors or excitation of carriers from traps. After a certain illumination dose, all optically active donors or traps are ionised, saturating the system. Further illumination cannot then increase carrier density, as there are no more trap states available. Contrary to what is observed for GaAs, after rest in the dark the resistivity starts to approach dark measurements values again.

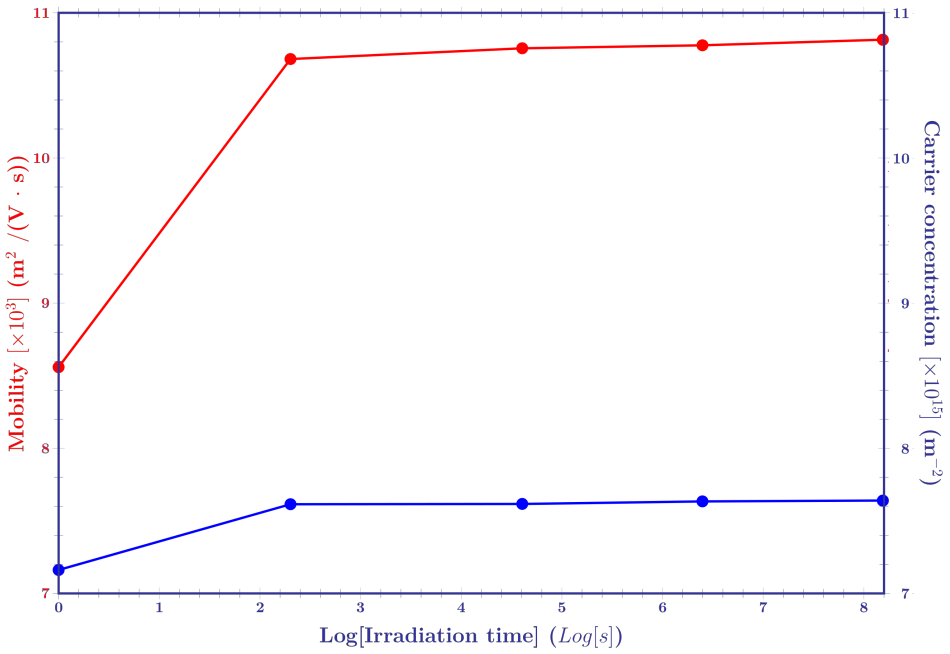

FIGURE 4.5: **Charge carrier concentration and carrier mobility as a function of irradiation time:** After initial irradiation the transport characteristics are kept virtually constant.

4.3.3 Sample C: light irradiation (1.3 um)

The second transport characterisation under light irradiation experiment was done with a gated, undoped sample. Gated samples showed relatively low tunabilities, most likely due to gate leakage. The illumination was done with a 1.3μm wavelength LED light source. Figure 4.6 shows the Shubnikov-de Haas oscillations for dark, 100ms, 500ms, and 1000ms illumination regimes. We can see a small downward shift of the resistance for non-zero illumination times, specially at low fields. Besides, even at relatively high magnetic fields (14T), the oscillations still display small amplitudes, not approaching zero resistance. This illustrates the poor conditions for charge transport in the sample. Figure 4.7 shows the charge carrier concentration and mobility as a function of top-gate voltage for different irradiation times. We can see the limited tunability of the device from the small range of the vertical axes. Figure 4.4a shows the carrier concentration curve corresponding to dark measurement as the lower bound of the curves, indicating a small amount of charge carriers were photo-excited. The slight increase in the carrier concentration and slight decrease in mobility upon illumination suggests the presence of photo-activated traps or defects, which contribute free carriers, but also introduce additional scattering. The system isn't entirely free of residual impurities or interface traps, and the illumination exposes hidden disorders that are not active in the dark.

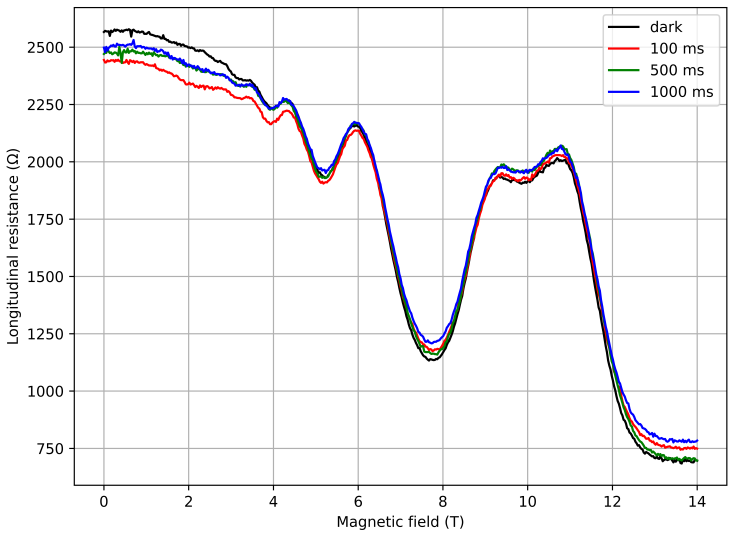

FIGURE 4.6: **Undoped sample Shubnikov-de Haas oscillations under light irradiation:** Gated samples showed low tunability due to gate leakage issues. The irradiation was done with a 1.3μm wavelength LED light source. The top-gate voltage is -1.5V.

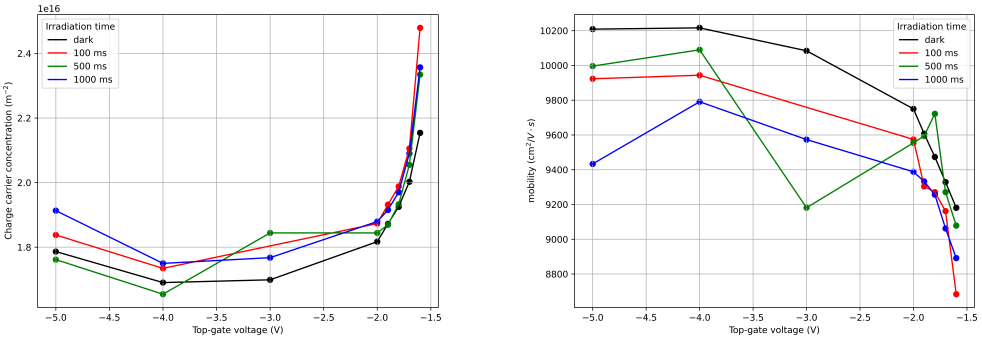

(a) Carrier concentration as a function of top-gate voltage for different irradiation times.

(b) Mobility as a function of top-gate voltage for different irradiation times.

FIGURE 4.7: **Undoped sample's transport characteristics under illumination**

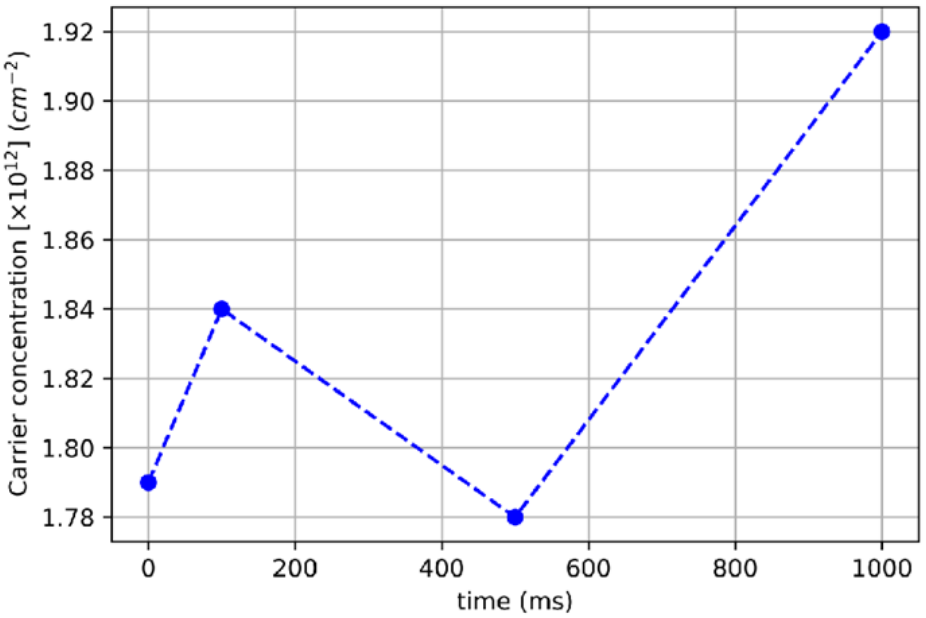

FIGURE 4.8: **Charge carrier concentration as a function of irradiation time:** No saturation is observed, which can be attributed to the short irradiation time. The total variation in the carrier density is, however, only $\approx 6.7\%$.

The overall behaviour of the samples with illumination suggests a low induced photoconductivity in comparison to GaAs persistent photoconductivity, for example. The contribution from traps, defects and other such mechanisms to the photo-induced carriers must still be taken into account, but the small percentual change (around 6.7%) suggests Ge may not suffer from persistent photoconductivity.

5

Conclusions

Germanium is a promising platform for photo-spin conversion in quantum dots. It has long coherence times, high hole mobility and is compatible with current industry Si-based infrastructure. As infrastructure goes, its band gap lies inside the bandwidth employed by telecommunication infrastructure, making it a natural candidate for a conversion platform between solid-state and photonic qubits. In particular, its strong spin-orbit coupling in the valence band, its low hyperfine interaction, and the possibility of nuclear spin-free isotopic engineering makes it an ideal medium for manipularing spin information in hole states. In confined nanostructures such as quantum dots, Ge quantum wells have the potential for precise photo-induced spin state preparation via circularly polarised light, following protocols akin to the Vrijen-Yablonovitch scheme, adapted for the holes. The quantum confinement also lifts the heavy and light holes degeneracy, enabling selective transitions that enhance spin-state purity. Ge is then positioned as a cornerstone in the development of scalable quantum networks and optically addressable quantum information processing.

To achieve this potential, however, the preparation of pristine SiGe interfaces is of utmost importance to realise high-quality devices with minimal defect densities, and well-controlled carrier transport. Contamination, from organic residues, and native oxides (notably GeO_x), can severely impact the electrical and structural integrity of gate dielectrics and ohmic contacts. Ohmic metals are diffused via annealing through the heterostructure and should, ideally, establish contact with the quantum well. Diffusion cannot happen, however, across native oxide layers. The required temperatures for such process to occur are usually much higher than the allowed thermal budget (above 700°C). A clean interface between semiconductor and metal is then a crucial step in device fabrication. Usually, heterostructures are covered with a thin SiO_2 capping layer, which must be removed in order to deposit ohmic metals. This removal exposes, however, the SiGe layer underneath it, which promptly starts to oxidise at normal laboratory conditions. A successful annealing relies then on the proper cleaning of this interface. Ideally, this cleaning process should yield atomic-level smoothness and chemical passivation of the surface. Of particular concern are GeO_x species, which rapidly regrow in air, making it necessary to minimise the exposure time of samples to atmosphere.

In the present work we evaluated four acid cleaning recipes based on different concentrations of aqueous HF acid solution, as well as different dipping times:

- **Recipe 1:** 10% HF (2 minutes)
- **Recipe 2:** 2% HF (2 minutes)
- **Recipe 3:** 2% HF (15s) $\rightarrow$ DIW rinse (The cycle is repeated 5 times)
- **Recipe 4:** 2% HF (2 minutes) + H_2O_2 (1 minute)

HF is corrosive to native oxides and a solvent to organic contaminants. It also, however, affects the heterostructure atomic species, and so, effective cleaning must be considered under the light of a trade-off with surface roughness. We observed the standard 10% HF solution (recipe 1) to be, generally, very damaging to surface smoothness, with a roughness given by an RMS value of 2.124 nm. On the other hand, solutions with lower HF concentration (2%) combined with Hydrogen peroxide provided a more gentle alternative, with RMS = 0.553 nm; closer to the unprocessed sample's roughness of RMS = 0.385 nm . Due to technical issues, Recipe 2, consisting of a 2% HF solution, could not have its roughness measured. Surprisingly, the cyclic cleaning (recipe 3), which employs low concentration HF (2%) and short dipping times (15s repeated 5 times and alternating with DIW rinse) presented very rough surfaces with RMS = 2.396 nm. This can be attributed to the short time of the acid cleaning step and to the frequent exchange of beakers in-between cycle steps. Albeit short, the exposure to air may kick-start the GeO_2 regrowth and the successive, fast steps in the cycle may contribute to roughing of the surface.

As a secondary effect of chemical cleaning, it must be also kept in mind that the induced surface roughness strongly influences metal diffusion mechanisms. Rough semiconductor surfaces have larger effective area and a richer topography for metal particles to interact with. This can enhance interdiffusion and affect the nature of interactions between phases: different inter-metallic compounds or silicides/germanides may form preferentially at protrusions or pits, altering the electrical properties of the contact. In essence, a rough interface fosters non-uniform phase formation. Roughness is also connected to diffusion pathways. Smoother interfaces force a more uniform, controlled intermixing, whereas rougher interfaces often indicate uncontrolled, path-dependent diffusion.

As for the recipes cleaning power, XPS analysis revealed broad Ge peaks, often extending towards the GeO_2 binding energy, indicating a persistent presence of oxides. The ratio between the contaminants peaks and the elemental Ge peak showed all recipes to have an approximately equal performance. The persistent presence of Ge oxides can be attributed to the exposure to air while loading the samples in the XPS machine's chamber, something that can only be fully addressed by in-loci cleaning. As for Si, Recipe 1 was successful in flattening the Si_2 peaks, while other recipes still kept visible, albeit small, peaks. When analysing the O binding energy region we can verify that no recipe was able to fully eliminate the peaks, indicating a lingering presence of adsorbed Oxygen molecules. As for organic contaminants, the XPS reading was compromised by the photoresist coated border with the measurement area, making it difficult to separate residual contributions in

the actual measurement area from false-positives from the border. Recipe 4, showed the best balance between cleaning and surface smoothing.

Devices fabricated with the standard recipe had a low yield. Their performance was, in general, affected by high resistance contacts, and, more importantly gate leakages and interfacial trap states. In quantum devices, especially spin-based systems, uncontrolled interface states can act as charge fluctuators and magnetic noise sources, degrading coherence. Surface traps and interfacial states at the semiconductor-dielectric boundary are important in defining the electronic landscape of devices, affecting performance. Such traps can originate from unsatisfied bonds, local strain fluctuations, dislocations, or chemical inhomogeneities, acting as centres for charge capture and emission. This increases noise and scattering.

From our devices, the doped samples showed the best overall behaviour. with clearly defined Hall plateaus and Shubnikov-de Hass oscillations reaching zero longitudinal resistivity for high magnetic fields. Such samples were analysed under different temperatures, revealing, through Lifshitz-Kosevich fitting, an effective hole mass of $0.15\mathrm{m}_0$, in accordance with the expectation of hole effective mass change in strained quantum wells [144]. For the undoped samples, one of them was not top-gated, and Shubnikov-de Haas oscillations were still observed, most likely due to unintentional p-doping during its growth. This sample's transport characteristics were observed under different illumination times from a 1.55μm wavelength LED light source. Since the LED is not designed to operate at cryogenic temperatures, the applied voltage needed to obtain the nominal output was greatly increased, making it difficult to maintain stable temperatures below 4.2K. After initial illumination, both the carrier concentration and mobility were observed to increase, remaining approximately constant for subsequent illumination. This indicates the photo-excitation of trap states which were quickly saturated.

A third sample, undoped and gated, was illuminated with a 1.3μm wavelength LED light source. This particular sample had low gate tunability due to gate leakage. Changes in carrier concentration were observed to be less than 10% and to return to dark measurement values after rest in the dark. This behaviour is contrary to what is observed in GaAs, for example, were carrier concentration can increase by over 100% and persist after light sources have been turned off. Accounting for the possible excitation of interfacial states, this suggests stable transport characteristics under light irradiation and no persistent photo-conductivity.

In summary, this work reinforces the position of Ge as a compelling platform for photo-spin conversion in quantum systems. However, fully realising this potential depends on particular attention to the cleanliness and topology of interfaces. We have shown that even aggressive HF-based cleaning protocols face challenges in order to fully eliminate interfacial oxides, with residual GeO_x species persisting as confirmed by XPS. While the standard 10% HF cleaning solution is effective, it introduces trade-offs with surface roughness, an often-overlooked parameter that has a profound impact on metal diffusion dynamics during ohmic contact formation.

Device characterisation revealed that contact resistance and gate leakage remain major limitations. These defects originate from structural and chemical imperfections.

Illumination experiments on undoped Hall bars with poor gating demonstrated that exposure to sub-band gap photons can still induce marked changes in carrier density and mobility, suggesting trap photo-excitation mechanisms. In particular, the observed saturation behaviour of transport properties following short exposure to 1.55 μm photons is indicative of mid-gap or band-tail states that are photo-ionised and rapidly filled. These findings demonstrate the sensitivity of quantum well transport to interfacial disorder and underscore the importance of understanding photo-excitation pathways, especially in optically addressable spin qubit architectures.

Ultimately, the interplay between interface cleanliness, surface topology, and illumination-induced trap dynamics represents a delicate triad that governs the performance of Ge/SiGe quantum devices. Advancing this platform toward scalable, low-noise, and high-fidelity quantum operations will require continued refinement of surface preparation techniques, development of low-leakage gate stacks, and in-depth exploration of light-matter interactions at the defect level. This work offers a step in that direction, providing experimental insight into the conditions necessary for coherent and stable operation in future Ge-based spin-photonic quantum systems.

5.1 Future prospects

In what regards the future steps in this investigation, the metal diffusion under different surface topography and compositional conditions must be evaluated, as well as stoichiometric tests of ohmic metal layer thickness versus quantum well depth.

The surface analysis employed in this work can be extended to other fabrication steps, such as ALD insulating layer deposition, to evaluate interfacial conditions and possible leakage paths and mechanisms.

Regarding the transport under light irradiation measurements the contributions from traps/impurities versus quantum well charges to photo-induced transport must be analysed and distinguished via a spectral dependence of transport characteristics.

Bibliography

1. Freeth, T. *et al.* Decoding the ancient Greek astronomical calculator known as the Antikythera Mechanism. *Nature Letters* **444,** 587–591 (2006).
2. Bruderer, H. The Antikythera Mechanism. *Communications of the ACM* **63,** 108–115 (2020).
3. Rojas-Sola, J. I. *et al.* Blaise Pascal's Mechanical Calculator: Geometric Modelling and Virtual Reconstruction. *Machines* **9** (2021).
4. Morar, F.-S. Reinventing machines: the transmission history of the Leibniz calculator. *The British Journal for the History of Science* **48,** 123–146 (2015).
5. Al-Razzaz al-Jazari, I. *The Book of Knowledge of Ingenious Mechanical Devices* ISBN: 978-94-010-2575-1 (D. Reidel Publishing Company, Dordrecht, Holland, 1974).
6. Bromley, A. G. The Evolution of Babbage's Calculating Engines. *Annals of the History of Computing* **9,** 113–136 (1987).
7. Hartree, D. R. The Bush Differential Analyser and its applications. *Nature* **146,** 319–323 (1940).
8. Electronics Associates, I. *EAI 680 Scientific Computing System, an economical high-performance hybrid computer* Brochure. `http://s3data.computerhistory.org/brochures/eai.680.1965.102646244.pdf` (2025).
9. Burks, A. R. & Burks, A. W. *The First Electronic Computer, the Atanasoff Story* ISBN: 0-472-10090-4 (University of Michigan Press, Michigan, United States, 1989).
10. Bissel, C. Historical perspectives - The Moniac A Hydromechanical Analog Computer. *IEEE Control Systems Magazine* **27,** 69–74 (1940).
11. Benjamin, B. V. *et al.* Neurogrid: A Mixed-Analog-Digital Multichip System for Large-Scale Neural Simulations. *Proceedings of the IEEE* **102,** 699–716 (2014).
12. Schemmel, J. *et al. A wafer-scale neuromorphic hardware system for large-scale neural modeling* in *2010 IEEE International Symposium on Circuits and Systems (ISCAS)* (2010), 1947–1950.

13. Bardeen, J. & Brattain, W. H. The Transistor, A Semi-Conductor Triode. *Physical Review* **74,** 230–231 (2 1948).

14. Brattain, W. H. & Bardeen, J. Nature of the Forward Current in Germanium Point Contacts. *Physical Review* **74,** 231–232 (2 1948).

15. Shockley, W. The theory of p-n junctions in semiconductors and p-n junction transistors. *The Bell System Technical Journal* **28,** 435–489 (3 1949).

16. Shockley, W. *et al.* p-n Junction Transistors. *Physical Review* **83,** 151–162 (1 1951).

17. Lilienfeld, J. E. US265372A (United States) (1928).

18. Heil, O. 439,457 (United Kingdom) (1935).

19. Kahng, D. & Atalla, M. *Silicon-Silicon dioxide field induced surface devices* in *IRE Solid-State Device Research Conference* (Carnegie Institute of Technology, Pittsburgh, 1960).

20. Greenlaw, R. *et al. Limits to Parallel Computation: P-Completeness Theory* ISBN: 9780195085914 (Oxford University Press, Oxford, UK, 1995).

21. Jacob, B. *et al.* in *Memory Systems* (eds Jacob, B. *et al.*) 353–376 (Morgan Kaufmann, San Francisco, 2008). ISBN: 978-0-12-379751-3.

22. Torrens, G. *et al.* A 65-nm Reliable 6T CMOS SRAM Cell with Minimum Size Transistors. *IEEE Transactions on Emerging Topics in Computing* **7,** 447–455 (2019).

23. Moore, G. E. Cramming more components onto integrated circuits. *Electronics* **38** (8 1965).

24. Wenzlhuemer, R. The Development of Telegraphy, 1870–1900: A European Perspective on a World History Challenge. *History Compass* **5,** 1720–1742 (2007).

25. Raboy, M. *Marconi: The Man Who Networked the World* Reprint edition. ISBN: 019090593X (Oxford University Press, Oxford, England, 2018).

26. Flosi, F. S. Father Landell de Moura - Radio Broadcasting Pioneer. *PHILATELIA CHIMICA ET PHYSICA* **34,** 18–26 (2012).

27. Beauchamp, K. *A History of Telegraphy* ISBN: 0852967926 (Institute of Engineering and Technology, 2001).

28. Pohlmann, K. *Principles of Digital Audio* 5th. ISBN: 0071441565 (McGraw-Hill/TAB Electronics, New York, U.S., 2005).

29. Bellamy, J. *Digital Telephony* 3rd. ISBN: 0-471-34571-7 (John Wiley & Sons, Inc, New York, U.S., 2000).

30. Hersent, O. *et al. Ip Telephony: Packet-Based Multimedia Communications Systems* ISBN: 0201619105 (Addison-Wesley Publising Company, New York, U.S., 1999).

31. Agrawal, G. P. *Fiber-Optic Communication Systems* 3rd. ISBN: 0-471-21571-6 (John Wiley & Sons, Inc, New York, U.S., 2001).
32. Keiser, G. *Fiber Optics Communication* ISBN: 978-981-33-4664-2 (Springer Nature Singapore, Singapore, 2021).
33. Manin, Y. I. *Computable and Non-computable* Russian. Originally published in Russian as *Vychislimoe i Nevychislimoe* (Sovetskoye Radio, Moscow, 1980).
34. Feynman, R. P. Simulating Physics with Computers. *International Journal of Theorethical Physics* **21,** 467–488 (1982).
35. Deutsch, D. & Jozsa, R. Rapid solution of problems by quantum computation. *Proceedings of the Royal Society A* **439,** 553–558 (1992).
36. Shor, P. W. Algorithms for quantum computation: discrete logarithms and factoring. *Proceedings 35th Annual Symposium on Foundations of Computer Science,* 124–134 (1994).
37. Boole, G. *An Investigation of the Laws of Thought* (PROJECT GUTENBERG, 2017).
38. Harris, D. M. & Harris, S. L. *Digital Design and Computer Architecture* 1st edition. ISBN: 978-0-12-370497-9 (Morgan Kaufmann Publishers, San Fransisco, U.S.A., 2007).
39. Sakurai, J. J. *Modern Quantum Mechanics* Revised Edition. ISBN: 0-201-53929-2 (Addison-Wesley Publishing Company, Massachusetts, U.S., 1994).
40. Nielsen, M. A. & Chuang, I. L. *Quantum Computation and Quantum Information* 10th Anniversary Edition. ISBN: 9781107002173 (Cambridge University Press, Cambridge, UK, 2010).
41. Von Neumann, J. *Mathematical Foundations of Quantum Mechanics* New Edition. Translated by Robert T. Beyer. ISBN: 9780691178561 (Princeton University Press, New Jersey, U.S., 2018).
42. Grover, L. K. A fast quantum mechanical algorithm for database search. *STOC '96: Proceedings of the twenty-eighth annual ACM symposium on Theory of Computing,* 212–219 (1996).
43. Zurek, W. H. Decoherence and the Transition from Quantum to Classical. *Physics Today* **44,** 36–44 (1991).
44. Unruh, W. G. Maintaining coherence in quantum computers. *Physical Review A* **51,** 992–997 (1995).
45. Shor, P. W. Scheme for reducing decoherence in quantum computer memory. *Physical Review A* **52,** R2493–R2496 (1995).
46. Preskill, J. in *Introduction to Quantum Computation and Information* (World Scientific, Singapore, 1998). ISBN: 978-981-238-525-3.

47. Nielsen, M. A. A simple formula for the average gate fidelity of a quantum dynamical operation. *Physics Letters A* **303,** 249–252 (2002).

48. Ballance, C. J. *et al.* High-Fidelity Quantum Logic Gates Using Trapped-Ion Hyperfine Qubits. *Physical Review Letters* **117,** 060504-1–-6 (2016).

49. Gambetta, J. M. *et al.* Building logical qubits in a superconducting quantum computing system. *npj Quantum Information* **3** (2017).

50. Preskill, J. Quantum Computing in the NISQ era and beyond. *Quantum* **2,** 79–99 (2018).

51. Cirac, J. I. & Zoller, P. Quantum Computations with Cold Trapped Ions. *Physical Review Letters* **74,** 4091–4094 (1995).

52. Gershenfeld, N. A. & Chuang, I. L. Bulk Spin-Resonance Quantum Computation. *Science* **275,** 350–356 (1997).

53. Chuang, I. L. *et al.* Experimental Implementation of Fast Quantum Searching. *Physical Review Letters* **80,** 3408–3411 (1998).

54. Loss, D. & DiVicenzo, D. P. Quantum computation with quantum dots. *Physical Review A* **57,** 120–126 (1998).

55. Kane, B. E. A silicon-based nuclear spin quantum computer. *Nature* **393,** 133–137 (1998).

56. Hanson, R. *et al.* Spins in few-electron quantum dots. *Reviews Of Modern Physics* **79,** 1217–1265 (2007).

57. Itoh, K. M. & Watanabe, H. Isotope engineering of silicon and diamond for quantum computing and sensing applications. *MRS Communications* **4,** 143–157 (2014).

58. Veldhorst, M. *et al.* A two-qubit logic gate in silicon. *Nature* **526,** 410–414 (2014).

59. Sammak, A. *et al.* Shallow and Undoped Germanium Quantum Wells: A Playground for Spin and Hybrid Quantum Technology. *Advanced Functional Materials* **29,** 1807613–8 (2019).

60. Hendrickx, N. W. *et al.* A single-hole spin qubit. *Nature Communications* **11** (2020).

61. Nakamura, Y. *et al.* Coherent control of macroscopic quantum states in a single-Cooper-pair box. *Nature* **398,** 786–788 (1999).

62. Jaksch, D. *et al.* Fast Quantum Gates for Neutral Atoms. *Physical Review Letters* **85,** 2208–2211 (2000).

63. Knill, E. *et al.* A scheme for efficient quantum computation with linear optics. *Nature* **409,** 46–52 (2001).

64. Wrachtrup, J. *et al.* Quantum Computation Using the 13C Nuclear Spins Near the Single NV Defect Center in Diamond. *Quantum Computations and Optical Processes* **91,** 429–437 (2001).

65. Jelezko, F. *et al.* Observation of Coherent Oscillations in a Single Electron Spin. *Physical Review Letters* **92,** 076401–4 (2004).

66. Gruber, A. *et al.* Scanning Confocal Optical Microscopy and Magnetic Resonance on Single Defect Centers. *Science* **276,** 2012–2014 (1997).

67. Wiesner, S. Conjugate Coding. *ACM SIGACT News* **15,** 78–88 (1983).

68. Bennett, C. H. & Brassard, G. Quantum cryptography: Public key distribution and coin tossing. *Conference on Computer Systems & Signal Processing* **1,** 175–179 (1984).

69. Bennett, C. H. & Brassard, G. Quantum cryptography: Public key distribution and coin tossing - reissue. *Theoretical Computer Science* **560,** 7–11 (2014).

70. Wootters, W. K. & Zurek, W. H. A single quantum cannot be cloned. *Nature* **299,** 802–803 (1982).

71. Dieks, D. Communication by EPR devices. *Physics Letters* **92A,** 271–272 (1982).

72. Ekert, A. Quantum Cryptography based on Bell's Theorem. *Physical Review Letters* **67,** 661–663 (1991).

73. Einstein, A. & nd N. Rosen, B. P. Can Quantum-Mechanical Description of Physical Reality Be Considered Complete? *Physical Review* **47,** 777–780 (1935).

74. Schroedinger, E. Discussion of Probability Relations Between Separated Systems. *Mathematical Proceedings of the Cambridge Philosophical Society* **31,** 555–563 (1935).

75. Horodecki, R. *et al.* Quantum Entanglement. *Review of Modern Physics* **81,** 865–942 (2009).

76. Bohm, D. *Quantum Theory* ISBN: 978-0-486-65969-5 (Dover Publications, New York, U.S., 1989).

77. Masanes, L. *et al.* All Bipartite Entangled States Display Some Hidden Nonlocality. *Physical Review Letters* **100,** 090403–4 (2008).

78. Bell, J. S. On the Einstein Podolski Rosen Paradox. *Physics Physique Fizika* **1,** 195–200 (1964).

79. Clauser, J. F. *et al.* Proposed Experiment to Test Local Hidden-Variable Theories. *Physical Review Letters* **23,** 880–884 (1969).

80. Tsirelson, B. Quantum generalizations of Bell's inequality. *Letters in Mathematical Physics* **4,** 93–100 (1980).

81. Freedman, S. J. & Clauser, J. F. Experimental Test of Local Hidden-Variable Theories. *Physical Review Letters* **28,** 938–941 (1972).

82. Aspect, A. *et al.* Experimental Tests of Realistic Local Theories via Bell's Theorem. *Physical Review Letters* **47,** 460–463 (1981).

83. Aspect, A. *et al.* Experimental Test of Bell's Inequalities Using Time-Varying Analyzers. *Physical Review Letters* **49,** 1804–1807 (1982).

84. Briegel, H.-J. *et al.* Quantum Repeaters: The Role of Imperfect Local Operations in Quantum Communication. *Physical Review Letters* **81,** 5932–5935 (1998).

85. Duan, L.-M. *et al.* Long-distance quantum communication with atomic ensembles and linear optics. *Nature* **401,** 413–418 (2001).

86. Sangouard, N. *et al.* Quantum repeaters based on atomic ensembles and linear optics. *Review of Modern Physics* **83,** 33–80 (2011).

87. Muralidharan, S. *et al.* Optimal architectures for long distance quantum communication. *Scientific Reports* **6** (2016).

88. Azuma, K. *et al.* All-photonic quantum repeaters. *Nature Communications* **6** (2015).

89. Patil, A. & Guha, S. An Improved Design for All-Photonic Quantum Repeaters. *arXiv:2405.11768v1 [quant-ph]* (2024).

90. Pant, M. *et al.* Rate-distance tradeoff and resource costs for all-optical quantum repeaters. *Physical Review A* **95,** 012304–14 (2017).

91. Hilaire, P. *et al.* Resource requirements for efficient quantum communication using all-photonic graph states generated from a few matter qubits. *Quantum* **5** (2021).

92. Burnham, D. C. & Weinberg, D. L. Observation of Simultaneity in Parametric Production of Optical Photon Pairs. *Physical Review Letters* **25,** 84–87 (1970).

93. Kwiat, P. G. *et al.* New High-Intensity Source of Polarization-Entangled Photon Pairs. *Physical Review Letters* **75,** 4337–4342 (1995).

94. Śliwa, C. & Banaszek, K. Conditional preparation of maximal polarization entanglement. *Physical Review A* **67,** 030101–4 (2003).

95. Christ, A. & Silberhorn, C. Limits on the deterministic creation of pure single-photon states using parametric down-conversion. *Physical Review A* **85,** 023829–6 (2012).

96. Branning, A. L. M. D. & Castelletto, S. Tailoring single-photon and multiphoton probabilities of a single-photon on-demand source. *Physical Review A* **66,** 053805–4 (2002).

97. Kaneda, F. & Kwiat, P. G. High-efficiency single-photon generation via large-scale active time multiplexing. *Science Advances* **5** (2019).

98. Eisaman, M. D. *et al.* Invited Review Article: Single-photon sources and detectors. *Review of Scientific Instruments* **82,** 071101–25 (2011).

99. Childress, L. *et al.* Fault-Tolerant Quantum Communication Based on Solid-State Photon Emitters. *Physical Review Letters* **96,** 070504–4 (2006).

100. Vrijen, R. & Yablonovitch, E. A spin-coherent semiconductor photo-detector for quantum communication. *Physica E* **10,** 569–575 (2001).

101. Awschalom, D. D. *et al.* Quantum technologies with optically interfaced solid-state spins. *Nature Photonics* **12,** 516–527 (2018).

102. Lodahl, P. *et al.* Interfacing single photons and single quantum dots with photonic nanostructures. *Reviews of Modern Physics* **87,** 347–400 (2015).

103. Greve, K. D. *et al.* Quantum-dot spin–photon entanglement via frequency downconversion to telecom wavelength. *Nature* **491,** 421–425 (2012).

104. Gao, W. B. *et al.* Observation of entanglement between a quantum dot spin and a single photon. *Nature* **491,** 426–430 (2012).

105. Delteil, A. *et al.* Generation of heralded entanglement between distant hole spins. *Nature Physics Letters* **12,** 218–223 (2016).

106. Stockill, R. *et al.* Phase-Tuned Entangled State Generation between Distant Spin Qubits. *Physical Review Letters* **119,** 010503–1 (2017).

107. Mustafa, S. *Chapter 4 Size–dependent structure parameter for silicon nanowires and nanoparticles 4.1. Introduction* PhD thesis (Oct. 2010).

108. Banthí-Barcenas, J. C. *et al.* Design of a quantum well based on a ZnCdSe/ZnTe type II heterostructure confined type I within ZnSe barriers. *AIP Conf. Proc.* **1934** (2018).

109. Kouwenhoven, L. P. *et al.* in *Mesoscopic Electron Transport* 1–44 (Springer Netherlands, Dordrecht, 1997).

110. Kouwenhoven, L. P. *et al.* Few-electron quantum dots. *Reports on Progress in Physics* **64,** 701–736 (2001).

111. Reimann, S. M. & Manninen, M. Electronic structure of quantum dots. *Review of Modern Physics* **74,** 1283–1342 (2002).

112. Hendrickx, N. W. *et al.* Gate-controlled quantum dots and superconductivity in planar germanium. *Nature Communications* **9** (2018).

113. Hendrickx, N. W. *et al.* A single-hole spin qubit. *Nature Communications* **11** (2020).

114. Hendrickx, N. W. *et al.* Fast two-qubit logic with holes in germanium. *Nature* **577,** 487–491 (2020).

115. Wang, Z. *et al.* Optimal operation points for ultrafast, highly coherent Ge hole spin-orbit qubits. *npj Quantum information* **7,** 487–491 (2020).

116. Jirovec, D. *et al.* A singlet-triplet hole spin qubit in planar Ge. *Nature Materials* **20,** 1106–1112 (2021).

117. Hendrickx, N. W. *et al.* A four-qubit germanium quantum processor. *Nature* **591,** 580–585 (2021).

118. Bosco, S. *et al.* Squeezed hole spin qubits in Ge quantum dots with ultrafast gates at low power. *Physical Review B* **104** (2021).

119. Wang, K. *et al.* Ultrafast coherent control of a hole spin qubit in a germanium quantum dot. *Nature Communications* **13** (2022).

120. Liu, H. *et al.* Gate-Tunable Spin-Orbit Coupling in a Germanium Hole Double Quantum Dot. *Physical Review Applied* **17** (2022).

121. Sarkar, A. *et al.* Electrical operation of planar Ge hole spin qubits in an in-plane magnetic field. *Physical Review B* **108** (2023).

122. Tidjani, H. *et al.* Vertical gate-defined double quantum dot in a strained germanium double quantum well. *Physical Review Applied* **20** (2023).

123. Vecchio, P. D. & Moutanabbir, O. Light-hole gate-defined spin-orbit qubit. *Physical Review B* **107** (2023).

124. Wang, C.-A. *et al.* Probing resonating valence bonds on a programmable germanium quantum simulator. *npj Quantum Information* **9** (2023).

125. Nigro, A. *et al.* Demonstration of Microwave Resonators and Double Quantum Dots on Optimized Reverse-Graded Ge/SiGe Heterostructures. *ACS Applied Electronic Materials* **6,** 5094–5100 (2024).

126. Van Riggelen-Doelman, F. *et al.* Coherent spin qubit shuttling through germanium quantum dots. *Nature Communications* **15** (2024).

127. Hendrickx, N. W. *et al.* Sweet-spot operation of a germanium hole spin qubit with highly anisotropic noise sensitivity. *Nature Materials* **23,** 920–927 (2024).

128. Lakic, L. *et al.* A quantum dot in germanium proximitized by a superconductor. *Nature Materials* **24,** 552–558 (2024).

129. Rooney, J. *et al.* Gate modulation of the hole singlet-triplet qubit frequency in germanium. *npj Quantum Information* **11** (2025).

130. He, L. X. *et al.* Infrared quenching of persistent photoconductivity in GaAs/AlxGa(1-x)As heterostructures. *Physical Review B* **39,** 1808–1818 (1989).

131. Fujita, T. *et al.* Angular momentum transfer from photon polarization to an electron spin in a gate-defined quantum dot. *Nature Communications* **10** (2019).

132. V. Klitzing, K. *et al.* New Method for High-Accuracy Determination of the Fine-Structure Constant Based on Quantized Hall Resistance. *Physical Review Letters* **45,** 494–497 (1980).

133. Tsui, D. C. *et al.* Two-Dimensional Magnetotransport in the Extreme Quantum Limit. *Physical Review Letters* **48,** 1559–1562 (1982).

134. Fulton, T. A. & Dolan, G. J. Observation of single-electron charging effects in small tunnel junctions. *Physical Review Letters* **59,** 109–113 (1987).

135. Wharam, D. A. *et al.* One-dimensional transport and the quantisation of the ballistic resistance. *Journal of Physics C* **21,** 209–214 (1988).

136. Van Wees, B. J. *et al.* Quantized conductance of point contacts in a two-dimensional electron gas. *Physical Review Letters* **80,** 848–850 (1988).

137. Grassman, T. J. *et al.* An atomic view of Fermi level pinning of Ge(100) by O2. *Surface Science* **602,** 2373–2381 (2008).

138. Lin, H. *et al.* Leakage current and breakdown electric-field studies on ultrathin atomic layer-deposited Al2O3 on GaAs. *Applied Physics Letters* **87,** 182904 (2005).

139. Landau, L. D. Diamagnetismus der Metalle. German. *Zeitschrift für Physik* **64,** 629–637 (1930).

140. De Haas, W. J. & van Alphen, P. M. The dependence of the susceptibility of diamagnetic metals upon the field. *Leiden Commun.* **208d.** Also published in *Proc. Netherlands Roy. Acad. Sci.* **33**, 1106 (1930) (1930).

141. De Haas, W. J. & van Alphen, P. M. The dependence of the susceptibility of diamagnetic metals upon the field. *Proc. Netherlands Roy. Acad. Sci.* **33,** 1106–1118 (1930).

142. Shubnikow, L. W. & de Haas, W. J. A new phenomenon in the change of resistance in a magnetic field in single crystals of bismuth. *Leiden Commun.* **207a.** Also reported in *Communications from the Physical Laboratory at Leiden* (1930).

143. Lifshitz, I. M. & Kosevich, A. M. Theory of magnetic susceptibility in metals at low temperatures. *Soviet Physics JETP* **2.** Translated from Zh. Eksp. Teor. Fiz. **29**, 730–742 (1955), 636–645 (1956).

144. Sawano, K. *et al.* Strain dependence of hole effective mass and scattering mechanism in strained Ge channel structures. *Applied Physics Letters* **95,** 122109 (2009).